Magnus Kyrre Windfeldt

Removal of Ti from pig iron by slag refining

Master's thesis in Materials Science and Engineering

Supervisor: Jafar Safarian

July 2020

Master's thesis

NTNU
Norwegian University of Science and Technology
Faculty of Natural Sciences
Department of Materials Science and Engineering

NTNU
Norwegian University of
Science and Technology

Magnus Kyrre Windfeldt

Removal of Ti from pig iron by slag refining

Master's thesis in Materials Science and Engineering
Supervisor: Jafar Safarian
July 2020

Norwegian University of Science and Technology
Faculty of Natural Sciences
Department of Materials Science and Engineering

NTNU
Norwegian University of
Science and Technology

Preface

This master's thesis is written as the finalisation of a 5-year degree in Material Science and Engineering at the Norwegian University of Science and Technology. It is part of the ENSUREAL project, which received funding from the European Community's Horizon 2020 Programme.

I would like to thank my supervisor Jafar Safarian for guiding me through this process. His knowledge and enthusiasm has been greatly appreciated. I would also like to thank my co-supervisor Kai Tang for his advice on thermodynamic modelling, and for providing data and diagrams using the FactSage software.

The work for this project was done during the spring and summer of 2020, and was thus affected by the COVID-19 pandemic. The uncertainty surrounding this situation was strenuous, and the resulting laboratory lockdown forced a shift in focus from experimental work to attempts at modelling. I am very grateful to everyone at the Department of Materials Science and Engineering who helped ensure a safe return to campus.

Out of these, department engineers Dmitry Slizovskiy and Ivar Andre Ødegård deserve a special mention. Their help and advice were vital to both planning and execution of the experimental part of this project. I would also like to thank Morten Peder Raanes for his help with EPMA and Torill Sørløkk for being able to do XRF-analysis at short notice when my original plans fell through.

Finally, thank you to my classmates and fellow students. You were always a source of motivation, and our frequent discussions gave me both understanding and perspective.

Trondheim, July 2020
Magnus Kyrre Windfeldt

Abstract

This project studies the feasibility of using slag refining to remove titanium from carbon-containing pig iron, as part of the ENSUREAL project for sustainable alumina production. A CaO-Al_2O_3-Fe_2O_3 slag mixture is used for the refining. The equilibrium of this system is examined at 1600 °C by use of thermodynamic modelling and experimental refining tests. Calculations for the model are based on Gibbs energy minimisation, and are done using MS Excel's solver tool with data from commercial thermochemical softwares. Refining experiments are done using synthetic slag and alloys with varying amounts of Ti and Fe_2O_3, both of which are produced as part of the project. The structure of the resulting materials is examined using EPMA, and their content is determined using XRF and LECO.

The model suggests the removal of both titanium and carbon from the metal by reaction with iron oxide in the slag. At low amounts of Fe_2O_3 it predicts preferential oxidation of titanium. This is supported by the experimental results, as the titanium is found mostly in the slag phase in all samples, while carbon levels in the metal are significantly lower when more Fe_2O_3 is used in the slag. The calculations from the project model are comparable with those of commercial software. Some unwanted TiC particles are also found in the metal when Ti content is high and low amounts of Fe_2O_3 is used. It is concluded that slag refining is a promising method for removing titanium from pig iron.

Sammendrag

I dette prosjektet undersøkes muligheten for bruk av slaggraffinering for å fjerne titan fra karbonholdig råjern, som en del av ENSUREAL-prosjektet for bærekraftig produksjon av alumina. Slaggen som brukes til raffinering er CaO-Al_2O_3-Fe_2O_3. Systemets likevekt undersøkes ved 1600 °C ved bruk av termodynamisk modellering og eksperimentelle raffineringsforsøk. Beregninger for modellen baserer seg på minimering av Gibbs energi og gjøres ved bruk av MS Excels problemløser, med data fra kommersiell termokjemisk programvare. Raffineringseksperimentene gjøres på syntetisk slagg og legeringer med varierende Ti- og Fe_2O_3-innhold som begge er produsert som en del av prosjektet. De resulterende materialenes struktur analyseres ved bruk av EPMA, og den kjemiske sammensetningen undersøkes ved bruk av XRF og LECO.

Modellen indikerer at både titan og karbon kan fjernes fra metallet ved at de reagerer med jernoksid i slaggen. Ved lavt Fe_2O_3-innhold forutsier den oksidering av titan foran karbon. De eksperimentelle resultatene støtter dette ved at titan hovedsakelig finnes i slaggen for alle prøver, og ved at karbonnivået i metallprøvene er betydelig lavere når slaggen inneholder mer Fe_2O_3. Beregningene gjort med modellen er ellers sammenlignbare med de fra kommersiell programvare. Noen uønskede TiC-partikler er også å finne i metallet når de inneholder mye titan og det brukes lite Fe_2O_3. Det konkluderes med at slaggraffinering er en lovende metode for å fjerne titan fra råjern.

Contents

Preface **i**

Abstract **iii**

Sammendrag **v**

List of Figures **ix**

List of Tables **xiii**

List of Abbreviations **xvii**

Nomenclature **xix**

1 Introduction **1**

2 Theory **3**

2.1 The Pedersen process 3

2.2 Slags and slag basicity 5

2.3 Solution thermodynamics 7

2.3.1 Gibbs energy of mixing 8

2.3.2 Activity coefficients 9

2.4 The Fe-Ti-C system 10

2.5 The Al_2O_3-CaO-FeO_x-TiO_x slag system 12

2.6 Slag refining and the slag-metal equilibrium 15

2.6.1 Reaching equilibrium 15

2.6.2 Ellingham diagram 16

2.6.3 Oxidation reactions 18

2.6.4 Partition coefficients 19

3 Experimental and modelling work 21

3.1 Materials and furnace equipment 21

3.2 Production of slag and alloys 23

3.2.1 Production of master slag 23

3.2.2 Production of master alloys 23

3.3 Refining experiments 25

3.3.1 Preparation 25

3.3.2 Experiments 27

3.4 Characterisation 28

3.4.1 EPMA 28

3.4.2 Chemical analysis 28

3.5 Modelling the phase distribution 29

3.5.1 Gibbs energy minimisation 29

3.5.2 Estimation of activity coefficients 29

3.5.3 Assumptions and simplifications 30

3.5.4 Implementation of the model 30

4 Results 31

4.1 Visual inspection after refining 31

4.2 Metal analysis 37

4.3 Slag analysis 41

4.3.1 Sample 1 41

4.3.2 Sample 2 43

4.3.3 Sample 3 45

4.3.4 Sample 4 49

4.3.5 Sample 5 51

4.3.6 Sample 6 . . . 53
4.4 Model results . . . 55

5 Discussion **59**
5.1 Implications of the model results . . . 59
5.2 Metal composition . . . 60
5.3 Distribution of titanium . . . 62
5.4 Structure of refining slag . . . 64

6 Conclusion **69**

References **71**

A Software **I**
A.1 HSC Chemistry 9 . . . I
A.2 FactSage 8.0 . . . I

B BSE images of metal **III**

C BSE images of slag **XI**

List of Figures

2.1 Schematic of the Pedersen process. 3

2.2 Phase diagrams of the slag from the Pedersen process. 5

2.3 Examples of the effect of Al compounds on slag structure. 7

2.4 Binary phase diagrams of the Fe-C and Fe-Ti systems. 11

2.5 Phase diagram of the Fe-Ti-C system. 12

2.6 Ternary phase diagrams of slag systems. 13

2.7 The phases in the CaO-Al_2O_3-MgO system at 1600 °C. 14

2.8 Typical concentration of Ti in Fe during slag refining. 16

2.9 Ellingham diagram. 17

3.1 Pictures of the blue furnace. 21

3.2 Pictures of the TF3 furnace. 22

3.3 Crushed CaO-Al_2O_3 slag. 23

3.4 Setup inside blue furnace. 24

3.5 Pictures of first alloying attempts. 24

3.6 Pictures of final master alloys. 25

3.7 Pieces of the master alloys after cutting. 26

3.8 Crucible setup for refining experiments. 27

4.1 Crucible contents from experiment 1. 31

4.2 Crucible contents from experiment 2. 32

4.3 Crucible contents from experiment 3. 33

4.4 Crucible contents from experiment 4. 34

4.5 Crucible contents from experiment 5. 35

4.6 Crucible contents from experiment 6. 36
4.7 BSE images of metal samples. 38
4.8 X-ray maps showing particles in metal. 40
4.9 BSE image of slag 1 with phase labels. 42
4.10 X-ray map of slag 1. 43
4.11 BSE image of slag 2 with phase labels. 44
4.12 X-ray map of slag 2. 45
4.13 BSE images of slag 3 with phase labels. 46
4.14 X-ray maps of slag 3. 48
4.15 BSE image of slag 4 with phase labels. 49
4.16 X-ray map of slag 4. 50
4.17 BSE image of slag 5 with phase labels. 51
4.18 X-ray map of slag 5. 52
4.19 BSE image of slag 6 with phase labels. 53
4.20 X-ray map of slag 6. 54
4.21 Calculated Gibbs energy in the slag phase. 55
4.22 Calculated Gibbs energy in slag depending on oxidation state. 56
4.23 Calculated Gibbs energy in the metal phase. 57
4.24 Calculated equilibrium phase content after refining of Fe-0,5Ti-C. 58
4.25 Calculated equilibrium phase content after refining of Fe-1,0Ti-C. 58
4.26 Calculated equilibrium phase content after refining of Fe-1,5Ti-C. 58

5.1 Calculated partition coefficients 59
5.2 Comparison of metal composition results. 61
5.3 Comparison of partition coefficients. 63

B.1 BSE images of metal from experiment 1. IV
B.2 BSE images of metal from experiment 2. V

B.3 BSE images of metal from experiment 3. VI

B.4 BSE images of metal from experiment 4. VII

B.5 BSE images of metal from experiment 5. VIII

B.6 BSE images of metal from experiment 6. IX

C.1 BSE images of slag from experiment 1. XII

C.2 BSE images of slag from experiment 2. XIII

C.3 BSE images of slag from experiment 3. XIV

C.4 BSE image of slag from experiment 4. XV

C.5 BSE images of slag from experiment 5. XVI

C.6 BSE images of slag from experiment 6. XVII

List of Tables

2.1 Selected characterisation results of slag and pig iron 5

2.2 Classification of common oxides. 6

2.3 Interaction coefficients for the Fe-Ti-C system. 10

2.4 Thermodynamic data for reaction equations. 19

3.1 Materials and crucibles used in experiments. 22

3.2 Composition of the master alloys. 23

3.3 Alloy combinations for refining. 26

3.4 Initial composition of the metal and slag phases used in the refining experiments. 27

3.5 Overview of all refining attempts. 28

4.1 Results of chemical analysis on refined metal done by Sintef Norlab. 37

4.2 Results of WDS analysis on metal. 39

4.3 Results of XRF analysis on refining slag. 41

4.4 WDS analysis of slag from experiment 1. 42

4.5 WDS analysis of slag from experiment 2. 44

4.6 WDS analysis of slag from experiment 3. 47

4.7 WDS analysis of slag from experiment 4. 50

4.8 WDS analysis of slag from experiment 5. 52

4.9 WDS analysis of slag from experiment 6. 54

5.1 Normalised results of chemical analysis on metal. 60

5.2 Content of titanium and titanium distribution coefficients from experimental samples. 62

5.3 Results of XRF analysis on refining slag. 64

5.4 Characterisation of slag phases from experiment 1. 65

5.5 Characterisation of slag phases from experiment 2. 65

5.6 Characterisation of slag phases from experiment 3. 66

5.7 Characterisation of slag phases from experiment 4. 66

5.8 Characterisation of slag phases from experiment 5. 67

5.9 Characterisation of slag phases from experiment 6. 67

List of Abbreviations

Al_2O_3 Alumina, aluminium oxide.

CaO Calcia, calcium oxide.

Fe_2O_3 Iron(III) oxide.

FeO_x Unspecified iron oxide.

FeO Iron(II) oxide.

MgO Magnesia, magnesium oxide.

SiO_2 Silica, silicon oxide.

Ti_2O_3 Titanium(III) oxide.

TiC Titanium carbide.

TiO_2 Titanium(IV) oxide.

TiO_x Unspecified titanium oxide.

at% Atomic percent.

BSE Backscatter electrons.

EPMA Electron probe microanalyser.

WDS Wavelength dispersive spectroscopy.

wt% Weight percent.

XRF X-ray fluorescence.

Nomenclature

$(\%i)$	Weight percent of compound i in slag
$[\%i]$	Weight percent of element i in metal
γ_i	Activity coefficient used with molar fractions
ρ_i^j	Second order coefficient for the interaction of element i with j, for use with molar fractions
ε_i^j	First order coefficient for the interaction of element i with j, for use with molar fractions
a_i	Activity of i
e_i^j	First order coefficient for the interaction of element i with j, for use with weight percents
f_i	Activity coefficient used with weight percents
K	Equilibrium constant
L_i	Partition coefficient of element i
M_i	Molar weight of i
x_i	Molar fraction of i

Chapter 1

Introduction

In recent years, the importance of more sustainable methods for metal production has become increasingly evident. The metals industry has shown deficits in all three dimensions of sustainability: Social, economic and ecological [1]. As the societal need for metals and metal products continues to increase, these issues must be addressed through improvement of methods and policies, as well as introduction of alternate production routes. An important aspect in many industrial improvement processes is the valorisation of byproducts, researching ways to use or sell materials that would otherwise be dumped as waste.

The EU project ENSUREAL [2] is an effort to improve the sustainability of the aluminium industry in Europe by introducing an alternate method for alumina production known as the Pedersen process. Implementation of this process is thought to reduce toxic emissions to both soil and atmosphere, while simultaneously reducing the supply risk of aluminium metal in European markets.

A central step in the Pedersen process is the pyrometallurgical reduction of bauxite ore into alumina-rich slag and pig iron. This latter byproduct has a market in the industrial production of steel or cast iron. However, the bauxite used in this process is known to be rich in titanium oxides [3], which is shown to be reduced into the metal phase along with the iron [4]. In order for the pig iron to be a saleable product, this titanium must be removed from the metal. The present project will investigate on a thermodynamic level the possibility of doing so by use of slag refining.

The theoretical basis for the slag refining is simple; iron oxide added to the process slag reacts with the titanium in the metal to form titanium oxides and additional metallic iron. The titanium is then removed with the slag. In practice this is a rather complex system, one which this project aims to investigate at equilibrium. This investigation is twofold: First, running a series of experiments where metal and slag of varying compositions are allowed to react to equilibrium at high temperatures. Second, making a simple thermodynamic model of the system as an attempt to predict its behaviour. Both the effects of varied titanium content in the metal and iron oxide amount in the slag are studied. The scope of the project does not include reaction kinetics, and all experiments and calculations are done at 1600 °C.

Combining and comparing the results of modelling and experimental refining attempts will provide some insight into the feasibility of this refining method. A primary concern is the interaction between titanium and carbon in the iron: Which element will oxidise first, and is there a risk of carbide formation? While it is expected for titanium to be preferentially oxidised, even partial simultaneous oxidation of carbon will greatly increase the necessary amount of Fe_2O_3 in the slag. This may not be detrimental to the feasibility of the method, but is important to understand should the process be further developed.

Chapter 2

Theory

2.1 The Pedersen process

The Pedersen process is an old process used to produce alumina from bauxite ore, combining both pyrometallurgical and hydrometallurgical methods. It was originally invented by Harald Pedersen in Trondheim in 1927 and used by A/S Norsk Aluminium Company in Høyanger between 1928 and 1969 to produce alumina from Greek bauxite [5]. The process became outdated when the use of tube autoclaves significantly reduced the cost of the competing Bayer process in 1967 [6]. The EU project ENSUREAL [2] seeks to revive a modern version of the Pedersen process for use in Europe in order to ensure a stable and sustainable supply of aluminium.

In the Pedersen process, the bauxite ore is carbothermally reduced together with lime to produce a CaO-Al_2O_3 slag as well as pig iron. Al_2O_3 is then extracted from the slag using a hydrometallurgical process based on leaching, leaving behind the byproduct known as grey mud [7, 8]. Figure 2.1 shows a simplified overview of a modernised Pedersen process.

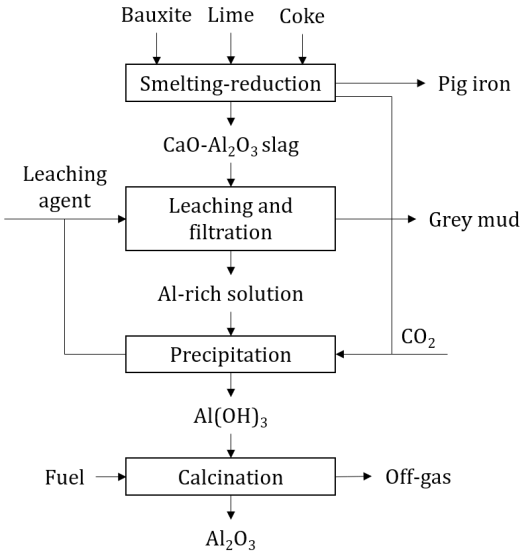

Figure 2.1: A simplified Pedersen process based on Azof et al. [7]

Development of an alternative to the Bayer process has for some time been considered a long

term solution to some of the problems in the aluminium industry [9]. Specifically, switching to the Pedersen process helps remedy two major issues: The availability of bauxite raw materials and the unwanted production of red mud.

The first problem is related to the quality requirements for bauxite ore. In order to produce alumina with the Bayer process the bauxite must be of higher purity than if the Pedersen process is used [5]. This limits the choice of raw material source to a few locations, which impacts both the supply stability and the transportation costs negatively. Developing the Pedersen process would therefore give alumina producers a wider choice of more locally sourced raw materials.

The second problem is caused by bauxite tailings, a toxic byproduct of the Bayer process often referred to as red mud. The processing and storage of this sludge is considered a major environmental issue for the alumina industry [10]. It mostly consists of a wide range of metallic oxides in the form of complex minerals, but can also contain elemental components such as sulphur and phosphorous as well as some organic compounds. The presence of soluble sodium compounds also gives rise to an elevated pH level in soil [11]. Efforts have been made to valorise this byproduct, but today it is still mostly stored in dams and landfills, some of which have been the cause of major environmental disasters [12]. As red mud is not a byproduct in the Pedersen process, switching from the Bayer process would eliminate this issue. This is also because both pig iron and grey mud, the major byproducts of the Pedersen process, have defined usage in the foundry and cement industries respectively [5].

As the Pedersen process is a rather complex process involving both pyrometallurgical and hydrometallurgical methods, it is important to understand how variations in an early step may influence the implementation of following steps. An investigation by Azof et al. [7] shows that the recovery of aluminium in the leaching step greatly depends on the structure of the slag produced by the smelting-reduction step. As shown in the phase diagram in figure 2.2a, there are a multitude of phases that may be formed based on the ratio of oxides in the slag. It is found that the $Ca_{12}Al_{14}O_{33}$ phase, also known as mayenite, is the most leachable phase in the CaO-Al_2O_3 system.

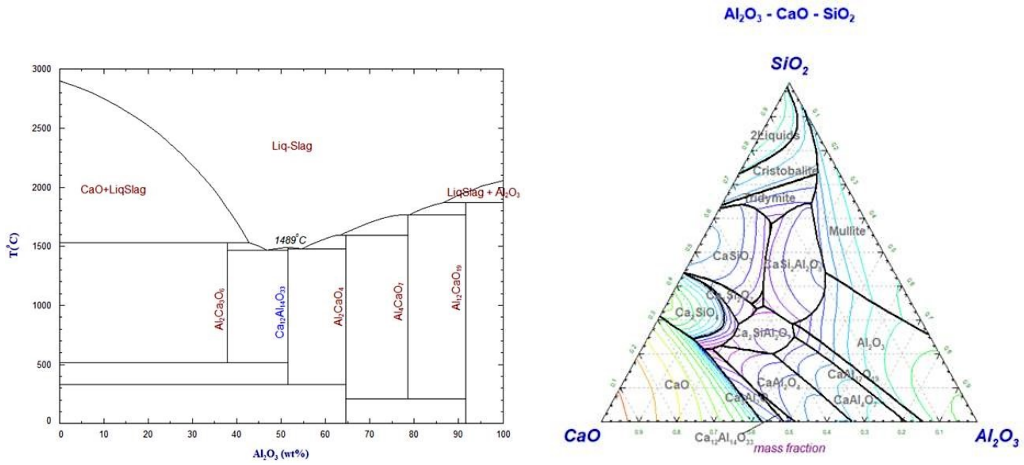

(a) Phase diagram of the CaO-Al_2O_3 system.

(b) Phase diagram of the CaO-Al_2O_3-SiO_2 system

Figure 2.2: Phase diagrams showing the slag phases present at equilibrium. Made using the FactSage 8.0 software [13].

From figure 2.2b, which shows the phase diagram of the CaO-Al_2O_3-SiO_2 system, we can see that addition of other oxides also affects the phase composition of the slag. A different study, also conducted by Azof et al. [14], has characterised the slag and pig iron produced when three different low-grade bauxite ores were heated with coke and lime. Table 2.1 shows the chemical content of the resulting slag and pig iron, obtained using XRF analysis. This supports the earlier findings of Sellæg et al. [8], where silicon, titanium and vanadium is shown to partially enter the metal phase during bauxite reduction. It can be seen that if the Pedersen process is to be usable for various low-grade bauxites, techniques for processing a wide range of slag and metal compositions must be available.

Table 2.1: Selected characterisation results of slag and pig iron from Azof et al. [14]

	Slag				**Pig iron**		
Oxide	Ore 1	Ore 2	Ore 3	**Element**	Ore 1	Ore 2	Ore 3
Al_2O_3 (wt%)	47,5	46,1	36,7	Fe (wt%)	89,9	92,0	92,7
CaO (wt%)	36,8	48,1	28,0	C_{sat} (wt%)	4,6	5,3	4,9
SiO_2 (wt%)	11,2	2,3	30,3	Si (wt%)	4,0	0,2	1,2
TiO_2 (wt%)	0,9	1,8	2,8	Ti (wt%)	0,6	0,9	0,2

2.2 Slags and slag basicity

The term slag is used to describe mixtures of oxides encountered in metallurgical processes. Refining of metal can be such a process, but slag is more commonly encountered as a by-product from the primary smelting of ores used to produce said metal. Such a slag mainly contains unreduced oxides from the ore and flux materials added to control various slag

properties, for example the addition of CaO in the form of lime, used to reduce its viscosity. The composition of a slag varies greatly from process to process, but some common oxide components include CaO, FeO, Al_2O_3 and SiO_2. Other oxides are also often present, as well as some phosphates, borates, sulfides, halides and carbides [15].

Compared to melts of metal, liquid slags display a great variety in their properties. This is mainly due to the ability of slag melts to form complex structures, which can vary greatly with both composition and temperature [16]. These structures are formed because of the predominantly ionic nature of liquid slags, an attribute first proposed by Herasymenko in 1938 [17]. It is here theorised that the main components of a slag are cations such as Fe^{2+}, anions such as O^{2-} and anion complexes such as ${AlO_3}^{3-}$. These anion complexes have later been shown to form polymeric networks in the slags, leading to the varying degree of structure observed [18].

The degree of structure in a slag has traditionally been referred to as the slags basicity. Individual oxide components are also classified as basic, acidic or amphoteric depending on how they affect the structure. The basicity of a slag is often taken as some variation on the ratio of basic oxides to acidic oxides. This is not an absolute measurement, and the basicity of different slags or oxides cannot be quantitatively compared [15]. It is common to discuss the physical properties of a slag in terms of its basicity.

Table 2.2: Common oxides classified as acidic, basic or amphoteric [16, 18].

Acidic	**Basic**		**Amphoteric**
SiO_2	CaO	FeO	Al_2O_3
P_2O_5	MnO	MgO	TiO_2
VO_2	BaO	ZnO	Fe_2O_3
B_2O_3	CoO	CdO	
	NiO	CuO	

The classification of oxides in terms of basicity is based on their ability to form structural networks. Thus, acidic oxides can also be referred to as *network forming* oxides, while basic oxides can also be called *network modifying* oxides [18]. Table 2.2 shows the classification of several common oxides. The most studied network former is SiO_2, which is widely reported to form tetraedric networks when present in liquid slags [19]. These are based on tetraedric ${SiO_4}^{4-}$ anion complexes, in which corner oxygen ions are shared between two tetraedra. Cations of basic oxides disrupt this network by providing charge balance to the oxygen ions without furthering the structure [20]. Amphoteric oxides are able to be either network forming or network modifying depending on the overall basicity of the melt.

In order to explain why oxides behave this way in a melt, the concepts of *bridging* and *non-bridging* oxygen ions are employed. Bridging oxygen ions are the ones that are shared between anion complexes and thus contribute to the polymerisation of the melt, while non-bridging ions do not [21]. In some compounds formed from amphoteric oxides, charge balance keeps the oxygen ions from being bridging unless they are also bound to a cation from a basic oxide. This is illustrated in figure 2.3, where compounds formed from Al_2O_3 contribute differently to the slag structure depending on what other components are present.

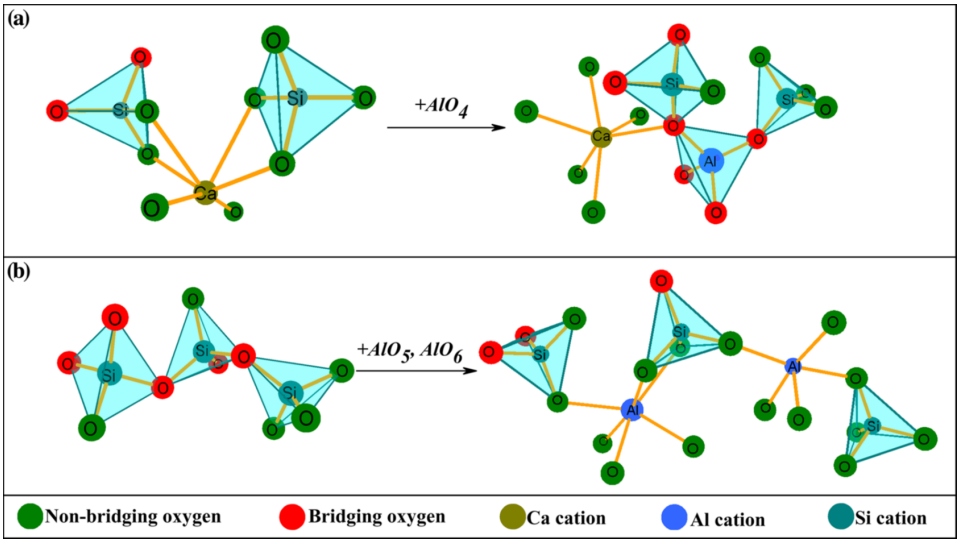

Figure 2.3: Schematic illustration from Chen et al. [20] of Al-based units acting (a) network forming and (b) network modifying.

The structures displayed in liquid slags do not necessarily translate into its solid state. Upon cooling in equilibrium, discrete and crystalline phases are formed, such as those displayed in the phase diagrams in figure 2.2. These phases do not form simultaneously however. Instead, one of the phases will often precipitate first, altering the composition of the melt until a second phase can form as well.

Predicting the formation of phases upon solidification is one of the main uses of phase diagrams. Using figure 2.2b as an example of this, we can see that at equilibrium, a melt containing 80 wt% Al_2O_3, 10 wt% CaO and 10 wt% CaO would start its solidification by precipitating grains of Al_2O_3. This would alter the composition of the melt until the $CaSi_2Al_2O_8$ is able to be formed as well. From solidification theory we can also predict that the first Al_2O_3 to solidify will form a dendrittic microstructure, while a lamellar eutectic will be formed should the two phases solidify together [22].

All this prediction of phase formation relies on the melt solidifying under equilibrium conditions. This requires the cooling rate to be low, as the diffusion necessary for crystallisation slows down at lower temperatures. The parts of the melt that have not formed a crystalline structure will then solidify as an amorphous solid. A slag that has solidified without the formation of any crystals is called a glass, and has been cooled down faster than its *critical cooling rate* [21]. This rate depends on multiple factors such as slag viscosity and system size.

2.3 Solution thermodynamics

In order to predict the behaviour of a system containing multiple components, we must describe it using the thermodynamics of solutions. The definitions provided here are based

on the texts of Stølen and Grande [23] as well as Engh [24]. They will form the foundations of a model predicting the distribution of elements between phases during refining.

2.3.1 Gibbs energy of mixing

All compounds and elements in the system have an innate Gibbs energy, denoted here by G_m, where the m indicates it being a molar property with the units $\mathrm{kJ\,mol^{-1}}$. If the compounds and elements of the system existed separately and did not interact, the total Gibbs energy of the system would be

$$G_{sys} = \sum_{i=1}^{k} n_i G_{m,i} = n_{tot} \sum_{i=1}^{k} x_i G_{m,i} \tag{2.1}$$

where n_i denotes the number of moles of substance i, n_{tot} is the total number of moles and x_i is the molar fraction of substance i in the system. However, because the components in the system mix together and form phases, the interaction of different atoms changes the Gibbs energy of the system. This change is known as the Gibbs energy of mixing, $\Delta_{mix}G$. Using the notation of partial properties, $\Delta_{mix}\overline{G}$, it is defined as

$$\Delta_{mix}G = \sum_{i=1}^{k} n_i \Delta_{mix}\overline{G}_i = \sum_{i=1}^{k} n_i RT \ln a_i \tag{2.2}$$

where R is the gas constant, T is the absolute temperature and a_i is the activity of substance i in solution. The activity is a function of the molar fraction of i by the relation

$$a_i = x_i \gamma_i \tag{2.3}$$

where γ_i is known as the activity coefficient of i. In the case where $\gamma_i = 1$ for all components in the solution, the solution is known as an ideal mixture. The Gibbs energy of mixing then becomes

$$\Delta^{id}_{mix}G = \sum_{i=1}^{k} n_i RT \ln x_i. \tag{2.4}$$

Knowing that

$$\ln a_i = \ln x_i + \ln \gamma_i \tag{2.5}$$

we can then rewrite $\Delta_{mix}G$ as

$$\Delta_{mix}G = \sum_{i=1}^{k} n_i RT \ln a_i = \Delta_{mix}^{id}G + \sum_{i=1}^{k} n_i RT \ln \gamma_i. \tag{2.6}$$

We then define a phases deviation from ideality as a separate thermodynamic property, known as the excess Gibbs energy of mixing. From equation 2.6, we see that this can be written as

$$\Delta_{mix}^{exc}G = \sum_{i=1}^{k} n_i RT \ln \gamma_i. \tag{2.7}$$

The total Gibbs energy of the system can then be described as

$$G_{sys} = \sum_{i=1}^{k} n_i G_{m,i} + \Delta_{mix}^{id}G + \Delta_{mix}^{exc}G \tag{2.8}$$

or, alternatively as

$$G_{sys} = \sum_{i=1}^{k} n_i G_{m,i} + \sum_{i=1}^{k} n_i RT \ln x_i + \sum_{i=1}^{k} n_i RT \ln \gamma_i. \tag{2.9}$$

Here it is important to note that x_i denotes the molar fraction of i in its respective phase, not in the system as a whole.

2.3.2 Activity coefficients

As seen from equation 2.7, the activity coefficient γ_i determines the degree of deviation from ideality for a component in solution. For atomic mixtures such as liquid metals, it has traditionally been calculated as

$$\ln \gamma_i = \ln \gamma_i^0 + \sum_{j=1}^{m} \varepsilon_i^j x_j. \tag{2.10}$$

Here, ε_i^j is known as the first order interaction coefficient of i with respect to j. If the molar fraction x_j is considered the probability for an i atom to interact with a j atom while in solution, the ε_i^j determines the effect of that interaction [24]. Combining equations 2.10 and 2.7 reveals that, due to the effect on $\Delta_{mix}^{exc}G$, negative interaction coefficients promote mixing while positive interaction coefficients are detrimental to mixing.

In some cases, especially if the solute concentration is high, second order interaction coefficients are used as well. These are typically denoted by ρ_i^j and $\rho_i^{j,k}$ [25] and alter equation 2.10 into

$$\ln \gamma_i = \ln \gamma_i^0 + \sum_{j=1}^{m} \left(\varepsilon_i^j x_j + \rho_i^j x_j^2 + \sum_{k=2}^{m} \rho_i^{j,k} x_j x_k \right). \tag{2.11}$$

2.4 The Fe-Ti-C system

Compared to other iron-based system, the Fe-Ti-C system has not been widely examined on a thermodynamic basis. Specifically, the interaction coefficients between titanium and carbon when dissolved in liquid iron at low concentration is not readily found in literature.

A complete set of first and second order coefficients for the Fe-Ti-C system was proposed in 1990 by Guo et al. [25] based on experimental work. While the self-interaction coefficient for titanium proposed by this paper is inconsistent with the ones published by Sigworth and Elliott [26] in 1974 and cited by Engh [24] in 1992, the data is successfully reproduced in thermodynamical calculations by Jonsson [27] in 1998. The various interaction coefficients are given in table 2.3.

Table 2.3: Interaction coefficients from literature [24, 25, 26].

Source	ε_C^C	ε_{Ti}^{Ti}	ε_{Ti}^{C}	ρ_{Ti}^{Ti}	ρ_{Ti}^{C}	$\rho_{Ti}^{Ti,C}$
Guo et al.		4,67	-11,94	0,32	-4,52	-9,96
Sigworth and Elliott	7,71	2,71				
Engh	6,92	2,71				

In the publications by Engh [24] as well as Sigworth and Elliot [26], the coefficients are presented in the form of e_i^j as opposed to the ε_i^j described earlier. This form is meant to be used with weight percentages instead of molar fractions. For comparison, all coefficients are here converted to the latter form by equation 2.12 [24], in which the M's denote the molecular weights of the interacting elements as well as the solvent liquid.

$$\varepsilon_i^j = 230 e_i^j \frac{M_j}{M_{Fe}} + \left(1 - \frac{M_i}{M_{Fe}}\right) \tag{2.12}$$

To better understand how the system behaves, we turn to the phase diagrams. These describe how the equilibrium state of the system changes when we vary parameters such as temperature or composition. In figure 2.4, the diagrams for the iron-rich sides of the Fe-C and Fe-Ti systems are shown. We see that individually both carbon and titanium is dissolved in liquid iron at low concentrations. At the temperatures shown here, carbon has an upper dissolution limit, represented by the line separating the *LIQUID* and *C + LIQUID* areas, that is not present in the Fe-Ti diagram. Upon solidification, these diagrams both indicate a separation into two phases: Ferrite (denoted as *BCC_A2*) and either graphite (*C*) or the intermediate phase Fe_2Ti. However, this equilibrium state is not necessarily reached. For the Fe-C case, it is known that carbon usually solidifies in the metastable Fe_3C phase

instead of as graphite [28]. As for the Fe-Ti case, the formation of the Fe_2Ti phase in alloys with low titanium content requires solid state diffusion. This is known to occur very slowly at low temperatures [29], to the point where the phase may not be formed in a foreseeable timeframe.

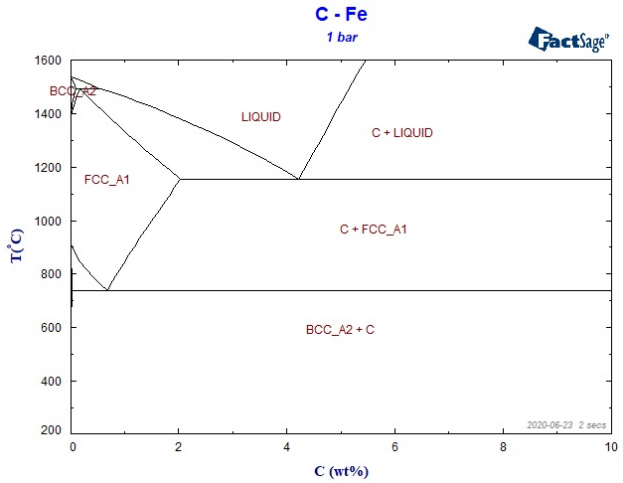

(a) Fe-rich side of the Fe-C phase diagram.

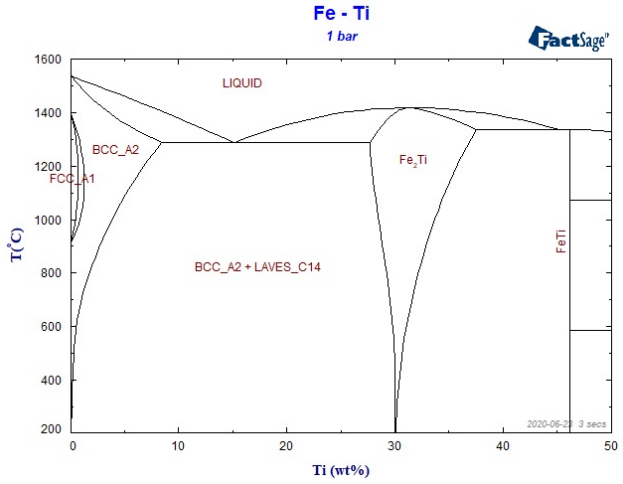

(b) Fe-rich side of the Fe-Ti phase diagram.

Figure 2.4: Binary phase diagrams describing the alloying of iron with carbon or titanium. Made using the FactSage 8.0 [13] software.

As indicated by the interaction coefficients presented in table 2.3, titanium and carbon does not act independently of each other when dissolved in iron. A phase diagram describing the ternary system is therefore shown in figure 2.5. In this diagram titanium and carbon content is varied along the axis, while isotherms are used to show the liquidus surfaces. A liquidus surface is used to describe the compositions that may be in equilibrium with a solid at a given temperature [23]. For example, the green 1700 °C isotherm in figure 2.5 indicates

the carbon- and titanium content in molten iron that is in equilibrium with TiC at that temperature.

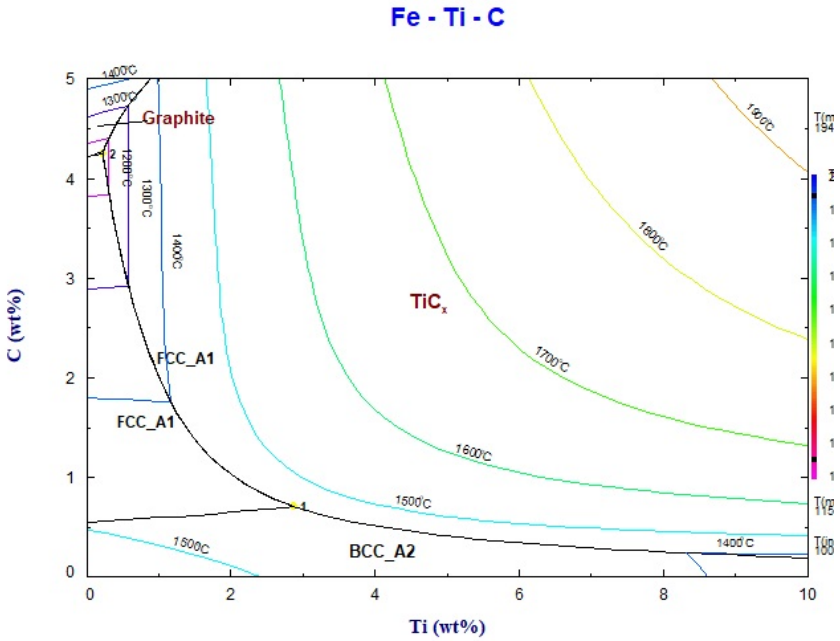

Figure 2.5: Phase diagram describing the alloying of iron with both carbon and titanium. Made using the FactSage 8.0 [13] software.

Among the phases in this diagram we can recognise several from the binary diagrams in figure 2.4, especially along the two axis. At higher concentrations of both elements, this ternary diagram indicates that the aforementioned TiC phase is formed as well. This carbide phase is known to form small particles that severely impact the properties of any steel [28]. Its presence in pig iron for steel production should therefore be controlled.

2.5 The Al_2O_3-CaO-FeO_x-TiO_x slag system

The slag system studied in this project is very complex. This is mainly due to the ability of some metallic elements to exist in various oxidation states. For example, divalent iron is present as FeO, while trivalent iron is present as Fe_2O_3. Similarly, trivalent titanium is present as Ti_2O_3, while tetravalent titanium is present as TiO_2. As discussed in section 2.2, the slag system is a mixture of ions and not clearly distinguishable oxides. Its composition is nonetheless described by using pure oxides as components. For example, the use of Fe_2O_3 and TiO_2 to denote composition in figure 2.6 describes the amount of iron, titanium and oxygen in the slag, but does not indicate the valence state of iron and titanium.

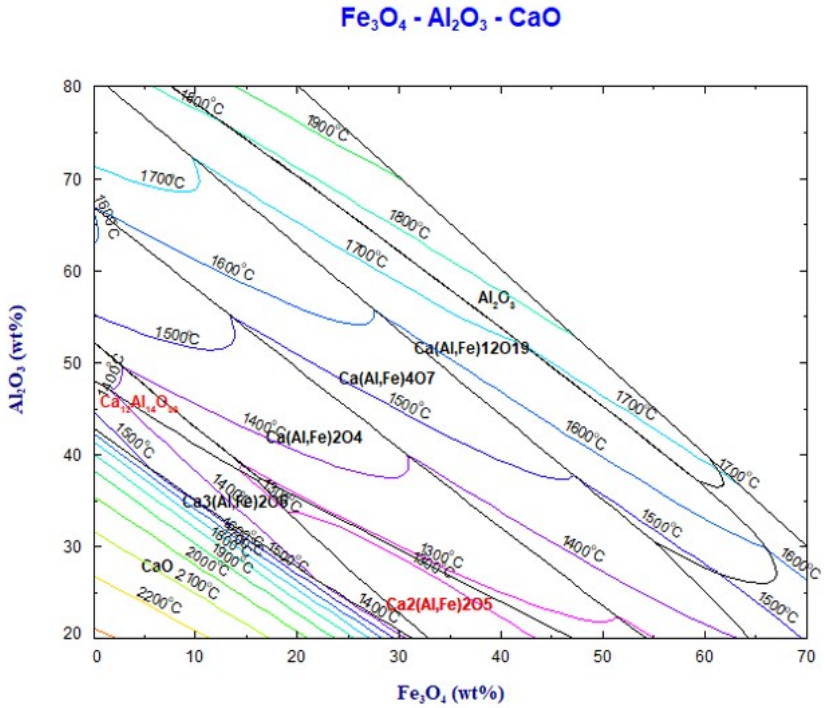

(a) Ternary phase diagram of the Al_2O_3-CaO-Fe_2O_3 system.

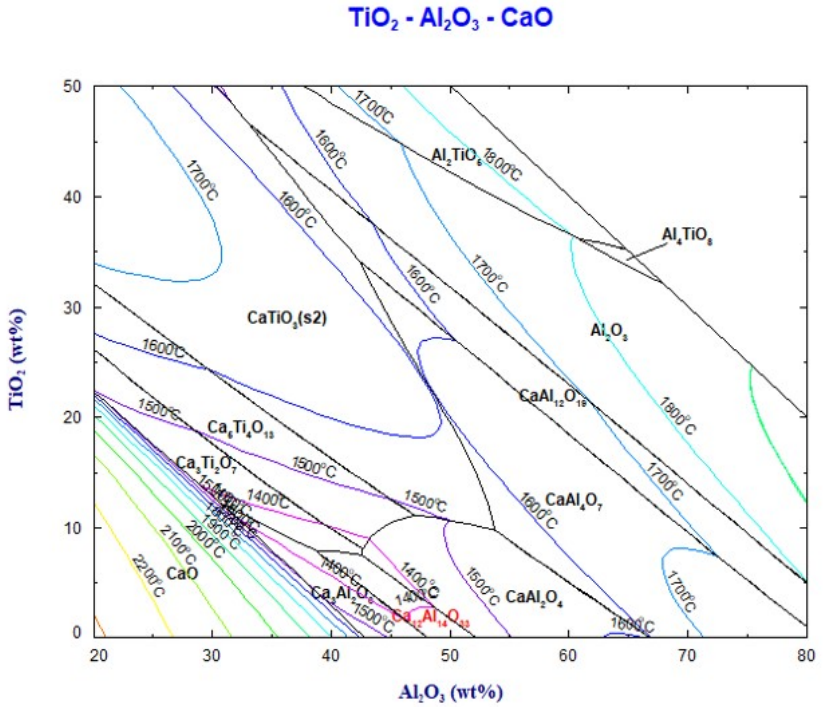

(b) Ternary phase diagram of the Al_2O_3-CaO-TiO_2 system.

Figure 2.6: Ternary phase diagrams describing the relevant slag systems. Made using the FactSage 8.0 software [13].

What we see in figure 2.6 are the ternary phase diagrams of the Al_2O_3-CaO-Fe_2O_3 and Al_2O_3-CaO-TiO_2 slag systems. They show what solid phases are formed at equilibrium during cooling, and at which temperatures. Along the Al_2O_3-axis we recognise the phases from the binary diagram in figure 2.2a.

Comparing the two diagrams, the most notable feature is the difference in solubility of Fe and Ti in the solid CaO-Al_2O_3 slag. Fe seems to be able to substitute for Al in the slag, allowing for similar phases to form in both the binary and ternary systems. The notable exception is the $Ca_{12}Al_{14}O_{33}$ phase, in which iron does not seem to dissolve. Titanium does not seem to be able to substitute for neither calcium nor aluminium however. Instead, it forms compounds with only calcium such as $Ca_3Ti_2O_7$ and $Ca_6Ti_4O_{13}$.

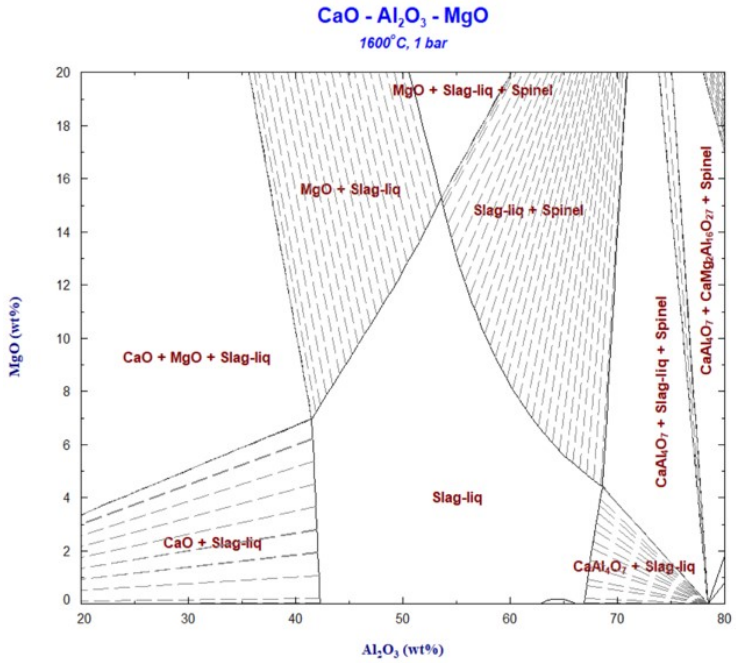

Figure 2.7: The phases in the CaO-Al_2O_3-MgO system at 1600 °C.

The refining experiments in this project are done using MgO crucibles, which may interact with the CaO-Al_2O_3 slag. Figure 2.7 shows a part of the ternary CaO-Al_2O_3-MgO phase diagram at 1600 °C. Here we can see that when CaO and Al_2O_3 are present in equal amounts by weight, as it is in the experiments done in this project, the solubility of MgO is around 10 wt%. This slag is then in equilibrium with the pure MgO in the crucible, suggesting that upon cooling MgO will precipitate as a singular phase. In comparison, if the Al_2O_3 content of the slag is higher, then the solid phase in equilibrium with the liquid slag is instead a spinel structure seemingly consisting of both MgO and Al_2O_3. Two phases containing all three oxides at around these compositions are also described in the Slag Atlas [16], the stable $Ca_3MgAl_4O_{10}$ compound and the metastable $Ca_7MgAl_{10}O_{23}$ compound. The formation of MgO-containing compounds is reported to reduce the leachability of aluminium from the slag, especially if silicon also is present in the system as an impurity [30]. As suggested by the phase diagram in figure 2.7 this effect is reduced at higher CaO concentrations.

2.6 Slag refining and the slag-metal equilibrium

Slag refining is the process of removing impurities from liquid metal by adding a slag to the system. Mass transfer of impurity and non-impurity elements then occur across the phase boundary until equilibrium is reached. This usually involves a chemical reaction in which a slag oxide is reduced and an alloy element is oxidised. Some elements will instead form gasses and thus be removed from the system. After refining, the slag and metal are physically separated. Due to the immiscibility of slag and metal, this is usually an uncomplicated process. Industrial examples of slag refining processes include the removal of phosphorous and sulphur from iron during steelmaking and the removal of phosphorous and boron from silicon for solar cell production [24, 31].

2.6.1 Reaching equilibrium

For the purpose of determining the viability of our proposed refining method, the slag-metal system is studied at equilibrium. This means that for all calculations, experiments and theoretical discussions, it is assumed that the reactions are given enough time that their rate is of no importance. A brief explanation of what this assumption entails based on Engh [24] is included here.

The driving force for the refining reaction to remove titanium from iron is the difference between the amount of titanium present in the iron and the amount of titanium present at a hypothetical equilibrium with the slag. We denote this difference as $[\%\mathrm{Ti}] - [\%\mathrm{Ti}]_e$. As the reaction happens, this difference will become smaller. The titanium will therefore be removed at a slower rate as time progresses, as described in the equation 2.13.

$$-M\frac{\mathrm{d}[\%\mathrm{Ti}]}{\mathrm{d}t} = k_t \rho A_s([\%\mathrm{Ti}] - [\%\mathrm{Ti}]_e) \tag{2.13}$$

Here, M is the mass of the metal (kg), k_t is the mass transfer rate ($\mathrm{m\,s^{-1}}$), ρ is the density of the metal ($\mathrm{kg\,m^{-3}}$) and A_s is the slag-metal contact area ($\mathrm{m^2}$). By performing a mass balance for titanium between the slag and metal and incorporate thermodynamic constants for the refining reaction, it is possible to integrate this expression over time. This results in equation 2.14.

$$\frac{[\%\mathrm{Ti}] - [\%\mathrm{Ti}]_\infty}{[\%\mathrm{Ti}]_{in} - [\%\mathrm{Ti}]_\infty} = \exp\left\{-\frac{k_t \rho A_s t}{M}\left(1 + \frac{\gamma_{\mathrm{Ti}} M}{K f_{\mathrm{Ti}} M_s}\right)\right\} \tag{2.14}$$

Here, K is the equilibrium constant for the reaction, M_s is the mass of the slag, γ_{Ti} and f_{Ti} are the activity coefficients for Ti in the metal and slag respectively. $[\%\mathrm{Ti}]_{in}$ denotes the initial amount of titanium in the iron, and $[\%\mathrm{Ti}]_\infty$ denotes the theoretical minimum amount of titanium in the metal, achieved when slag-metal equilibrium is reached. This gives an exponential drop in titanium content, as shown in figure 2.8.

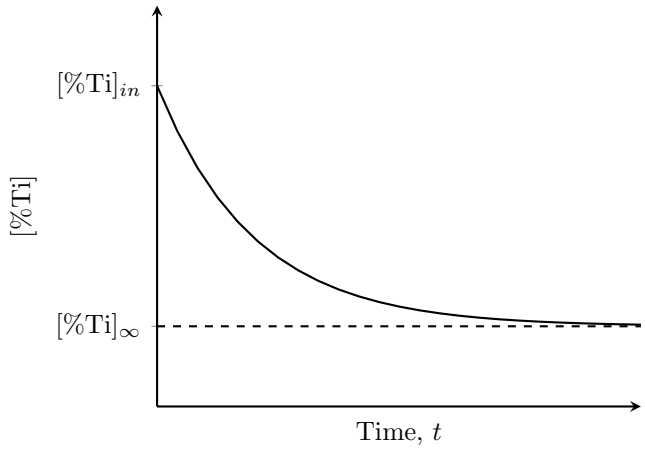

Figure 2.8: Concentration of titanium in metal melt during slag refining. Based on Engh [24].

From this it becomes clear that even if thermodynamic parameters such as γ_{Ti} and kinetic parameters such as k_t are unknown, it is possible to study a system approaching equilibrium by allowing reactions to occur over a long period of time.

2.6.2 Ellingham diagram

When working with systems where the stability of oxides are of concern, it is customary to use an Ellingham diagram. This is a diagram showing the Gibbs energy of formation for various oxides, balanced to one mole of O_2, as a function of temperature. Each oxide is then represented by a continuous line, with breaks for first-order phase transitions in either the oxide or the corresponding metal [23]. Comparing the lines of two or more oxides allows for easy assessment of which is the most stable, as those in the lower part of the diagram tend to be oxidised at the expense of those further up.

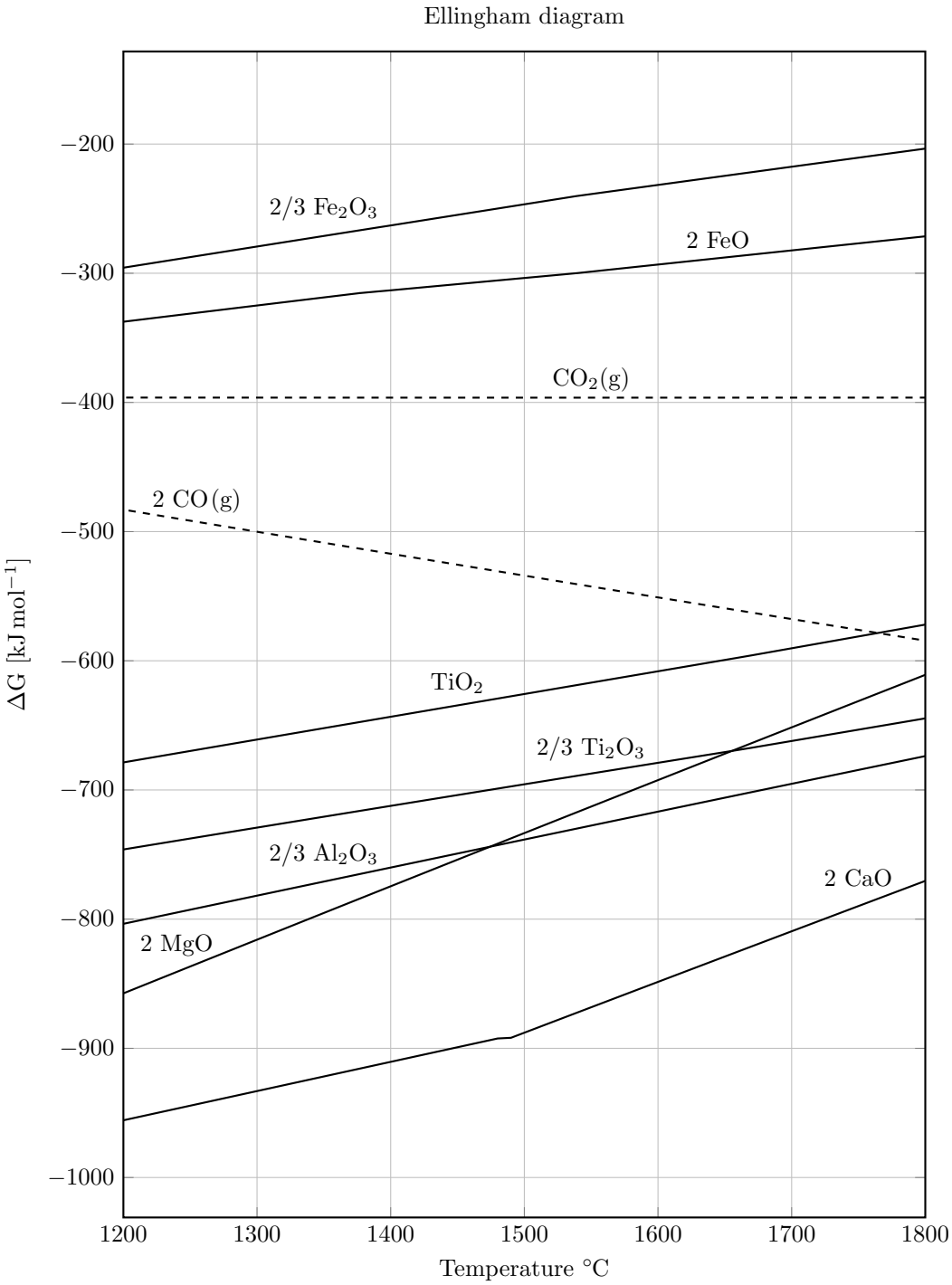

Figure 2.9: Ellingham diagram showing the formation energy for the relevant oxides, balanced for equal oxygen stochiometry. Made using data from HSC Chemistry 9 [32].

An Ellingham diagram for the oxides relevant to this project is shown in figure 2.9. It is drawn using data from HSC Chemistry 9 [32]. We see that the most stable oxides in the system are CaO and Al_2O_3, used to make the initial slag, as well as the crucible material MgO. The oxides formed from iron, titanium and carbon, the elements in the metal, are all further up in the diagram. This means that if no other oxide is added to the slag, no reaction between the slag and metal is expected at 1600 °C. As the diagram is drawn only for pure oxides, this assessment does not take into account the effect of concentration and activity on the energy of reaction. We do however see that if more oxygen is added to the system, titanium and carbon are both expected to be removed from the metal phase and enter the slag and gas phases respectively. This is the basis for the refining method studied in this project.

2.6.3 Oxidation reactions

The study of slag refining is really the study of selective oxidation reactions. Thus, the oxidation reactions expected in the system should be explored. If we assume that the oxidation state of each element is the one furthest down in the Ellingham diagram in figure 2.9, these reactions will be as shown below:

$$2\,\mathrm{FeO} + \frac{4}{3}\,\mathrm{Ti} \rightleftharpoons 2\,\mathrm{Fe} + \frac{2}{3}\,\mathrm{Ti_2O_3} \tag{2.15}$$

$$2\,\mathrm{FeO} + 2\,\mathrm{C} \rightleftharpoons 2\,\mathrm{Fe} + 2\,\mathrm{CO\,(g)} \tag{2.16}$$

The oxidation state of the various elements will however not be as uniform as described above. For each of them, an equilibrium will exist between their two states. These equilibrium reactions are balanced by the element in its elemental state, as shown in the equations below:

$$\mathrm{Fe_2O_3} + \mathrm{Fe} \rightleftharpoons 3\,\mathrm{FeO} \tag{2.17}$$

$$3\,\mathrm{TiO_2} + \mathrm{Ti} \rightleftharpoons 2\,\mathrm{Ti_2O_3} \tag{2.18}$$

$$\mathrm{CO_2(g)} + \mathrm{C} \rightleftharpoons 2\,\mathrm{CO\,(g)} \tag{2.19}$$

Any interaction between iron, titanium, carbon and oxygen in the system can be described using a combination of these reaction equations. The standard Gibbs energy of reaction at 1600 °C for each is shown in table 2.4, together with the equilibrium constant K for the same temperature. This constant is derived from the reaction energy as shown in equation 2.20, and is used to define the state of equilibrium as in equation 2.21.

$$K = \exp\left(-\frac{\Delta_r G^0}{RT}\right) \tag{2.20}$$

$$b\,\mathrm{B} + c\,\mathrm{C} \rightleftharpoons d\,\mathrm{D} + e\,\mathrm{E}, \qquad K = \frac{a_D^d \cdot a_E^e}{a_B^b \cdot a_C^c} \tag{2.21}$$

In these equations, R is the gas constant, T is the absolute temperature and a is the activity of the species B-E.

Table 2.4: Thermodynamic data for reaction equations. Values from HSC Chemistry 9 [32].

Reaction	$\Delta_r G^0$ $[\mathrm{kJ\,mol^{-1}}]$	$\log K$
2.15	-386,379	10,775
2.16	-257,666	7,186
2.17	-92,437	2,578
2.18	-212,513	5,927
2.19	-154,619	4,312

Thus, for the equilibrium in equation 2.15, the following holds:

$$K = 10^{10,775} = \frac{a_{\mathrm{Fe}}^2 \cdot a_{\mathrm{Ti_2O_3}}^{2/3}}{a_{\mathrm{FeO}}^2 \cdot a_{\mathrm{Ti}}^{4/3}} \tag{2.22}$$

A similar relation could be made for all reactions in the system. However, as any gas species formed is continuously removed from the system, the equations involving CO (g) and CO_2(g) will not reach an easily definable equilibrium.

2.6.4 Partition coefficients

A commonly used tool for studying the distribution of elements between phases in equilibrium is the partition coefficient L_i. It is defined as the relative amount of an element in one phase over the relative amount of that element in another phase [24]. This relative amount may be presented either as weight percent or atomic percent, and may be either that of the element itself or one of its compounds, such as an oxide in slag. In this project it is defined using molar content of each element as shown below:

$$L_{\mathrm{Ti}} = \frac{(\%\ \mathrm{Ti})}{[\%\ \mathrm{Ti}]}, \qquad L_{\mathrm{Fe}} = \frac{(\%\ \mathrm{Fe})}{[\%\ \mathrm{Fe}]} \tag{2.23}$$

Here, $(\%i)$ is the atomic percent of the element in the slag and $[\%i]$ is the atomic percent of the element in the metal.

The partition coefficient also relates heavily to the equilibrium constant K. Using the alternate partition coefficients

$$L'_{\mathrm{Ti}} = \frac{(\%\ \mathrm{Ti_2O_3})^{1/2}}{[\%\ \mathrm{Ti}]} \qquad \text{and} \qquad L'_{\mathrm{Fe}} = \frac{(\%\ \mathrm{FeO})}{[\%\ \mathrm{Fe}]} \tag{2.24}$$

allows rewriting equation 2.22 as

$$K = \frac{a_{\mathrm{Fe}}^2 \cdot a_{\mathrm{Ti_2O_3}}^{2/3}}{a_{\mathrm{FeO}}^2 \cdot a_{\mathrm{Ti}}^{4/3}} = \frac{\gamma_{\mathrm{Fe}}^2 \cdot \gamma_{\mathrm{Ti_2O_3}}^{2/3}}{\gamma_{\mathrm{FeO}}^2 \cdot \gamma_{\mathrm{Ti}}^{4/3}} \cdot \frac{x_{\mathrm{Fe}}^2 \cdot x_{\mathrm{Ti_2O_3}}^{2/3}}{x_{\mathrm{FeO}}^2 \cdot x_{\mathrm{Ti}}^{4/3}} = \frac{\gamma_{\mathrm{Fe}}^2 \cdot \gamma_{\mathrm{Ti_2O_3}}^{2/3}}{\gamma_{\mathrm{FeO}}^2 \cdot \gamma_{\mathrm{Ti}}^{4/3}} \cdot \frac{(L'_{\mathrm{Ti}})^{4/3}}{(L'_{\mathrm{Fe}})^2} \tag{2.25}$$

Proper use of this kind of relation requires knowledge of both activity coefficients and the distribution of elements between their oxidation states in the slag phase. It may therefore be impractical for use with complex systems.

Chapter 3

Experimental and modelling work

3.1 Materials and furnace equipment

Two furnaces at the Department of Material Science at NTNU were used for the experimental part of this work. They are an induction furnace known as the blue furnace and a graphite tube resistance furnace known as TF3. This section contains a brief outline of their functionality as well as specifications for crucibles and raw materials.

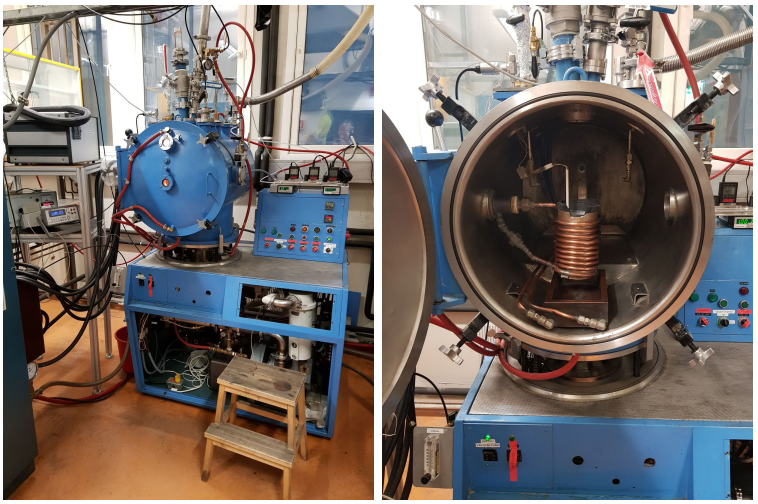

(a) Outside of the furnace while is use. (b) Inside of the furnace, with an insulated crucible inside the coils.

Figure 3.1: The blue furnace, used for production of slag and alloys.

The blue furnace, pictured in figure 3.1, is a closed induction furnace. Material is heated within crucibles which are placed inside a copper coil. It also allows for casting by tilting the coil and emptying the crucible into a water-cooled copper mould. The furnace can be used in vacuum or with a flowing gas atmosphere. Pictured in figure 3.2 is TF3, a closed resistance heat furnace in which smaller crucibles are heated within a graphite tube chamber. It is operated in a flowing gas atmosphere.

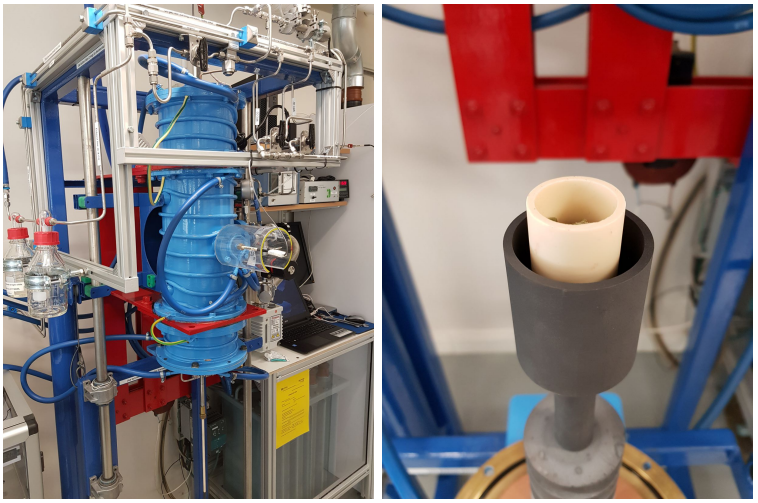

(a) Outside of the TF3 furnace.

(b) Crucible in place on an open furnace lid.

Figure 3.2: The TF3 furnace, used for production of alloys and refining experiments.

The slag was made from powdered oxides and the alloys were made from flakes of metallic sponge. The specifications of the raw materials are listed in table 3.1, together with the magnesia crucibles used for refining.

Table 3.1: Materials and crucibles used in experiments.

Material	**Purity**	**Supplier**
Al_2O_3 powder	99 %	Alfa Aesar, ThermoFisher
CaO powder	99,9 %	Sigma-Aldrich
Fe_2O_3 powder	$\geq$ 99,5 %	Sigma-Aldrich
Fe sponge	99,9 %	Alfa Aesar, ThermoFisher
Ti sponge	99,9 %	Alfa Aesar, ThermoFisher
MgO+Y_2O_3 crucibles	$\sim$ 99,2 %	Tateho Ozark Techn. Ceramics

3.2 Production of slag and alloys

3.2.1 Production of master slag

The slag used for the refining experiments is a mixture of CaO, Al_2O_3 and Fe_2O_3. While the latter is added to the refining crucible in its pure form and in varying amounts, the first two are added as a compound made beforehand using the blue furnace.

The production method for CaO-Al_2O_3 slag is based on previous work [33]. It consists of melting equal amounts of each oxide powder by weight in a graphite crucible. It is then cast into the blue furnace's cooled copper mould where it is allowed to solidify. The slag is then crushed into the pieces pictured in figure 3.3.

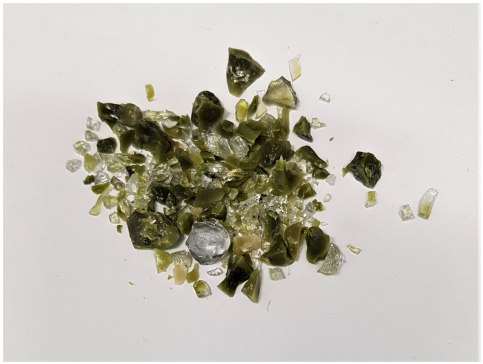

Figure 3.3: Crushed CaO-Al_2O_3 slag.

3.2.2 Production of master alloys

In the main refining experiments, the metal contains varying amounts of titanium and carbon dissolved in iron. To achieve this, the metal is a mix of several master alloys. These alloys are produced using the metallic raw materials in table 3.1. A graphite crucible is used as a carbon source, giving an estimated carbon content of 5,5 wt% at saturation [Kai Tang, personal communication, 6th March 2020]. In order to prevent the formation of titanium carbide during production, separate alloys were made containing either carbon or titanium. The compositions of the master alloys are shown in table 3.2.

Table 3.2: Composition of the master alloys.

Alloy name	**Fe (wt%)**	**Ti (wt%)**	**C_{sat} (wt%)**
MA1	99	1	
MA2	97	3	
MA3	94,5		5,5

To make the alloys with titanium, both metal powders were charged into Al_2O_3 crucibles which were then placed inside graphite crucibles. These were then heated in the blue furnace to 1700 °C and kept there for half an hour before cooling. A top view of this setup is shown in figure 3.4. As the use of two crucibles did not allow for the tilting necessary for mould casting, the metal was allowed to solidify in the crucibles. The Al_2O_3 crucibles were then removed from the metal by crushing with a hammer. Two compositions were made, corresponding to alloys MA1 and MA2 in table 3.2. The resulting metal slabs can be seen in figure 3.5.

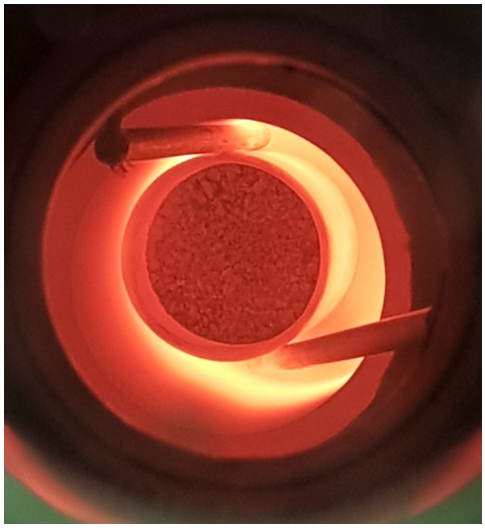

Figure 3.4: Top view of the setup using an Al_2O_3 crucible in the blue furnace during heating.

Following this, the alloys were remelted in an attempt to improve the homogeneity of the slabs. For this they were cut into smaller pieces and recharged into new Al_2O_3 crucibles. Some powdered metal was also added in this step to increase the amount of alloy produced. The blue furnace was first used to remelt the MA1 alloy, but this attempt was unsuccessful as the furnace had to be shut down due to safety concerns before reaching the target temperature of 1800 °C. The remelting was then moved to the TF3 furnace where both MA1 and MA2 were remelted, still in Al_2O_3 crucibles. The former was heated to 1750 °C and held for 2,5 hours, while the latter was heated to 1800 °C and kept for half an hour. For MA2, a controlled cooling rate of 300 °C h^{-1} was used to see if it would reduce the surface inhomogenieties that were observed in earlier attempts. The final alloys slabs used for further experimental work are shown in figure 3.6.

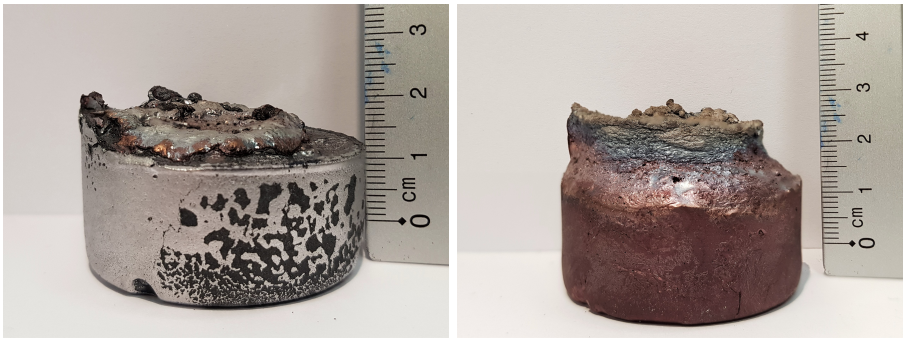

(a) Sideview of the 1 % Ti alloy.

(b) Sideview of the 3 % Ti alloy.

Figure 3.5: The results from the first alloying attempts in Al_2O_3 crucibles.

(a) The 1% Ti alloy (MA1) before cutting. (b) The 3% Ti alloy before (MA2) cutting.

Figure 3.6: The alloys after remelting in the TF3 furnace.

3.3 Refining experiments

3.3.1 Preparation

In order to use the master alloys for the refining experiments, the metal slabs had to be cut into smaller pieces. The metal had proven impractical to cut using the equipment at the department, so this was done by NTNU's Finmekanisk Verksted, a workshop for use by the Faculty of Natural Science. They were able to cut each slab into six equally-sized pieces using a water-jet cutter with abrasives. The pieces are shown in figure 3.7.

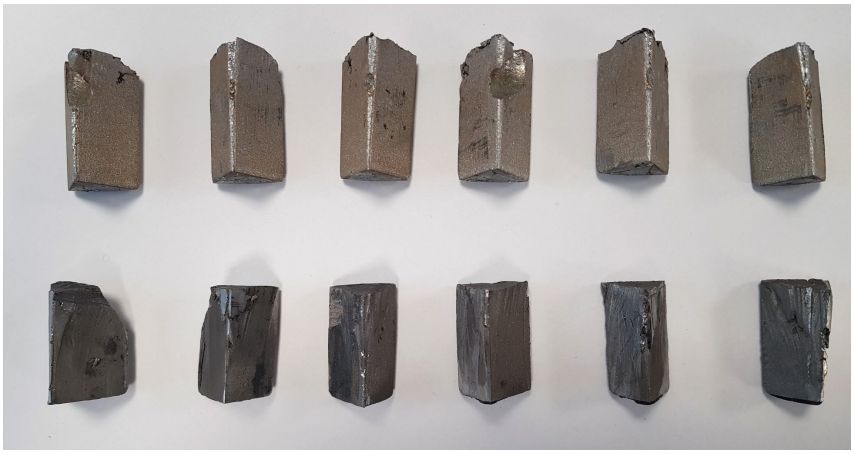

Figure 3.7: The pieces of the master alloys as received from the workshop. The upper pieces are MA1 and the lower pieces are MA2. The rust visible on the MA1 pieces developed during the laboratory lockdown.

The refining experiments required combining the three master alloys, with the compositions as defined in table 3.2, in three different ways. Three of each combination was required for a total of nine alloy combinations. This was done by semi-randomly cutting the metal into even smaller pieces, weighing them, and then combining the pieces with matching weights. When some of the refining experiments had to be redone, this process was repeated. The alloy combinations used for the final experiments are shown in table 3.3.

Table 3.3: The alloy combinations for refining, labelled by which experiment they were used for.

Nr.	**Intended content**			**Weight of pieces (g)**		
	MA1	MA2	MA3	MA1	MA2	MA3
1				22,7	-	22,7
4	50%	-	50%	19,7	-	19,7
7				27,0	-	26,9
2				12,8	12,8	25,6
5	25%	25%	50%	10,5	10,5	20,9
8				-	-	-
3				-	22,9	22,9
6	-	50%	50%	-	18,8	18,9
9				-	-	-

3.3.2 Experiments

In the refining experiments, slag and metal was heated together in the TF3 furnace and kept at 1600 °C for 2 hours. The metal to slag ratio was 2:1 by weight and the crucible material was Y_2O_3-stabilised MgO. The crucibles were charged as shown in figure 3.8, which also shows the outer graphite crucible.

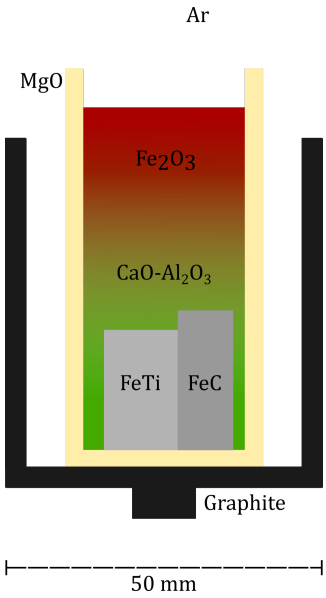

Figure 3.8: Sketch of the crucible setup for refining experiments.

In table 3.4, the intended chemical composition of the metal and slag prior to refining is shown for each experiment. Three different metal compositions are used, containing either 0,5 wt%, 1,0 wt% or 1,5 wt% titanium. The amount of Fe_2O_3 added to the slag is then chosen from the stochiometry of reactions 3.1 and 3.2 below: For experiments 1-3, just enough Fe_2O_3 is added to oxidise only the Ti. For experiments 4-6, just enough Fe_2O_3 is added to oxidise both the carbon and the titanium. These stochiometric calculations assume that no other reactions occur. Experiments 7-9 in table 3.4 refer to a planned series of tests using double the amount of Fe_2O_3 as in experiments 4-6. While one of these tests were attempted, they were ultimately abandoned due to time and material constraints.

Table 3.4: Initial composition of the metal and slag phases used in the refining experiments.

Experiment	**1**	**2**	**3**	**4**	**5**	**6**	**7**	**8**	**9**
Fe (wt%)	96,75	96,25	95,75	96,75	96,25	95,75	96,75	96,25	95,75
Ti (wt%)	0,5	1,0	1,5	0,5	1,0	1,5	0,5	1,0	1,5
C (wt%)	2,75	2,75	2,75	2,75	2,75	2,75	2,75	2,75	2,75
CaO (wt%)	48,9	47,8	46,7	36,7	35,6	34,5	23,4	21,2	19,0
Al_2O_3 (wt%)	48,9	47,8	46,7	36,7	35,6	34,5	23,4	21,2	19,0
Fe_2O_3 (wt%)	2,2	4,4	6,6	26,6	28,8	31,0	53,2	57,6	62,0

$$3Ti + 2Fe_2O_3 = 4Fe + 3TiO_2 \tag{3.1}$$

$$3C + Fe_2O_3 = 2Fe + 3CO \tag{3.2}$$

Some of the refining experiments were unsuccessful, referring to experiments where the MgO crucibles cracked before cooling, causing the molten metal and slag to spill out into the outer graphite crucible. This was assumed to happen either because of thermal expansion of entrapped metal or slag particles, or because of the crucibles' vulnerability to thermal shock. While the risk of the former could be reduced by careful charging of the crucibles,

alleviation of the latter issue was attempted by reducing the heating rate. A heating rate of 600 °C h^{-1} was initially used, but due to a number of failures it was later reduced to 200 °C h^{-1} in accordance with the recommendations of the crucible manufacturer.

Table 3.5: Overview of all refining attempts.

Nr.	Heating rate	Result
Test	Fast	Success
1	Fast	Success
2	Fast	Success
3	Fast	Success
4	Fast	Failure
6	Fast	Failure
4	Slow	Success
5	Slow	Failure
6	Slow	Success
5	Slow	Success
7	Slow	Failure

Table 3.5 shows an overview of all furnace experiments in chronological order. The choice of heating rate is shown along with whether or not the experiment was successful. The number column refers to the compositions in table 3.4. A total of 11 furnace runs were completed, 4 of which did not succeed.

3.4 Characterisation

In preparation for characterisation, the resulting slag and metal phases were removed from the crucibles. This was done by first crushing the crucibles with a hammer, freeing the metal. The remaining crucible material was then removed from the slag by sand blasting.

3.4.1 EPMA

In order to study the distribution of elements within the slag and metal, samples were taken from each phase and investigated using an electron probe microanalyser (EPMA). This equipment allows for imaging of sample cross sections by use of backscatter electrons (BSE), elemental analysis of phases by use of wavelength-dispersive spectroscopy (WDS), as well as X-ray mapping to show elemental distribution. This is done by comparing the characteristic x-rays of a sample to a standard of known composition [34].

The samples were prepared for EPMA by retrieving small pieces of the phases by either crushing (slag) or cutting (metal). These were then cast in epoxy and polished to produce a flat surface. A nano-layer of carbon was deposited on these surfaces using high vacuum sputtering to ensure electrical conductivity.

3.4.2 Chemical analysis

Chemical analysis was done of both the metal and slag to learn the distribution of elements between the two phases. X-ray fluorescence spectrometery (XRF) was used for the analysis of oxides in the slag as well as for metallic elements in the iron. Combustion analysis was also used on the metal samples to find the amount of carbon.

The slag was prepared for XRF by crushing and milling it into a fine powder. The analysis was then performed at the Department of Geoscience and Petroleum at NTNU. As for the

metal, disc samples were cut from the material. These were sent to SINTEF Norlab, where both XRF and combustion analysis were done.

3.5 Modelling the phase distribution

In an attempt to predict the distribution of elements between the metal and slag phase after refining, a model was made based on the thermodynamic principles outlined in section 2.3. The model is built in Microsoft Excel 2005 using the Excel Solver tool. Thermodynamic data is provided using the HSC Chemistry 9 [32] and FactSage 8.0 [13] softwares.

3.5.1 Gibbs energy minimisation

The Excel Solver tool functions by optimising one *target* parameter by changing several other *variable* parameters under limitations defined through *restrictions*. In this case, the target parameter is the total Gibbs energy of the system, which should be minimised as this would indicate the thermodynamic equilibrium. The variable parameters are the number of moles of each component in the liquid phases, limited by mass balance restrictions, demanding the total amount of each element in the system to be constant.

The total Gibbs energy of the system is defined in section 2.3 as

$$G_{sys} = \sum_{i=1}^{k} n_i G_{m,i} + \sum_{i=1}^{k} n_i RT \ln x_i + \sum_{i=1}^{k} n_i RT \ln \gamma_i. \tag{3.3}$$

Here, G_{sys} is the target parameter that Solver will minimise and n_i are the parameters Solver can change. The $G_{m,i}$ for each pure component in their liquid state at 1600 °C are taken from HSC. The molar fractions of each component in their respective phase, x_i, is a simple function of n_i and is calculated as such.

3.5.2 Estimation of activity coefficients

To obtain values for γ_i applicable at all the composition combinations the Solver software will attempt, continuous functions in which each activity coefficient depends on all components of its phase are estimated. This is done by first obtaining the activity data of the phases at several compositions from FactSage. It is then assumed that should such a function exist, it would be on the form described in section 2.3:

$$\ln \gamma_i = \ln \gamma_i^0 + \sum_{j=2}^{k} \varepsilon_i^j x_j. \tag{3.4}$$

Then, the Solver tool is used to do a multi-variable regression analysis based on the least-squares method. This method lets the Solver tool determine the parameters $\ln \gamma_i^0$ and ε_i^j by minimising the sum of the squared differences between the FactSage activity coefficients and the calculated coefficients at each point for which FactSage data exists. While these are only estimates of γ_i^0 and ε_i^j, the nomenclature is nonetheless used here.

Equation 3.4 is only used for the metal phase, as it mostly contains iron with only a little titanium and carbon. As the slag phase has oxide concentrations that can vary greatly and are often of comparable magnitudes to each other, equation 3.5 is used instead as described in section 2.3. The inclusion of ρ_i^j and $\rho_i^{j,k}$, the second order interaction coefficients, corrects for the greater variety and complexity in the slag, but also increases the amount of activity data necessary to do linear regression.

$$\ln \gamma_i = \ln \gamma_i^0 + \sum_{j=1}^{m} \left(\varepsilon_i^j x_j + \rho_i^j x_j^2 + \sum_{k=2}^{m} \rho_i^{j,k} x_j x_k \right). \tag{3.5}$$

3.5.3 Assumptions and simplifications

In order to simplify the calculations described above it is necessary to make a number of assumptions. These are listed below together with a brief explanation.

1. The metal phase only contains Fe, C and Ti. In reality, all components will exist in all phases, but it is assumed that the amount of dissolved amount of other elements in the metal phase is negligible.
2. Carbon only exists in the gas phase or dissolved in metal. This assumption means that the possibility for formation of carbides and the dissolution of carbon in the slag is ignored.
3. The only gas that is formed is CO.
4. The dissolution of crucible material is negligible. While some dissolution of crucible material may occur, ignoring it drastically simplifies calculations.
5. The gas phase can be represented by a constant and very low partial pressure of CO. This avoids the kinetic calculations necessary for modelling a flowing gas atmosphere in which CO is continuously removed. The partial pressure is chosen as $\frac{p}{p^0} = 0,1$.

3.5.4 Implementation of the model

When using this model, input data in the form of initial composition in both the slag and metal phases must be provided, as well as initial mass for each phase. Then, the composition of each phase at equilibrium and activity data for each component is returned as output data. The simplicity of the model limits the number of compositions that can be modelled to one at a time, meaning that the model must be run repeatedly if a range of compositions is to be investigated. In order to match the refining experiments, the calculations were done using a 2:1 initial metal to slag ratio.

Chapter 4

Results

4.1 Visual inspection after refining

This section contains images and descriptions of the slag and metal as they were upon removal from the furnace. The pictures were taken after removing excess crucible material. Experiment numbers refer to table 3.4.

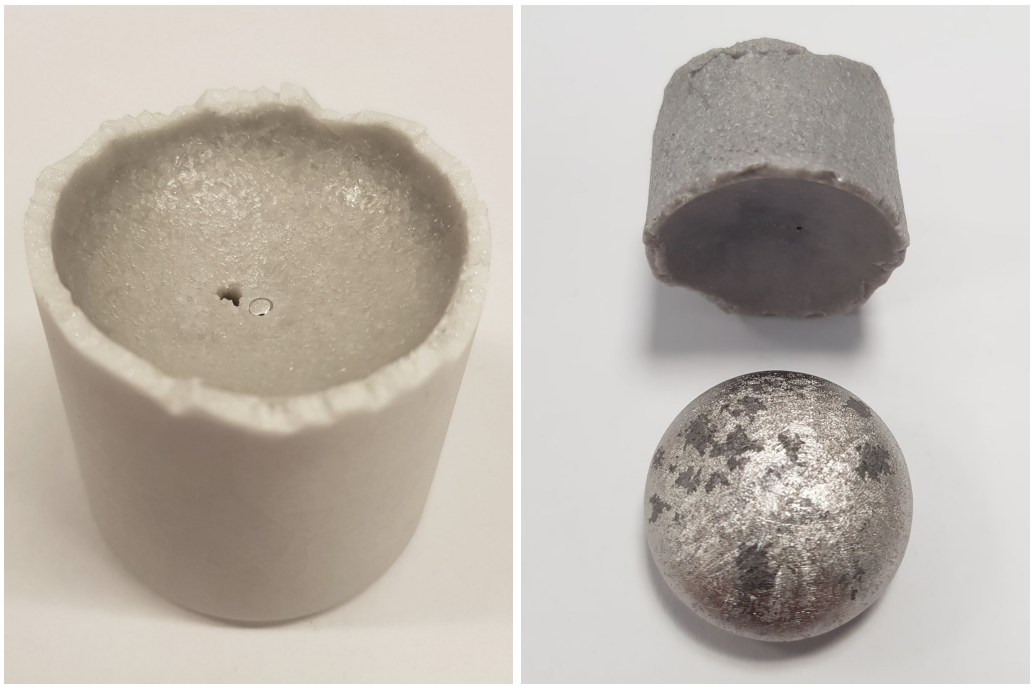

(a) The top of the slag after removing the upper part of the crucible.

(b) The slag and metal after removing the crucible.

Figure 4.1: Crucible contents from experiment 1.

Figure 4.1 shows the contents of the crucible after refining experiment 1. The slag was white/gray in colour and proved difficult to crush due to its hardness. The metal was easily separated from both slag and crucible, but some slag remnants visible in figure 4.1b had to be removed by sand blasting prior to further processing.

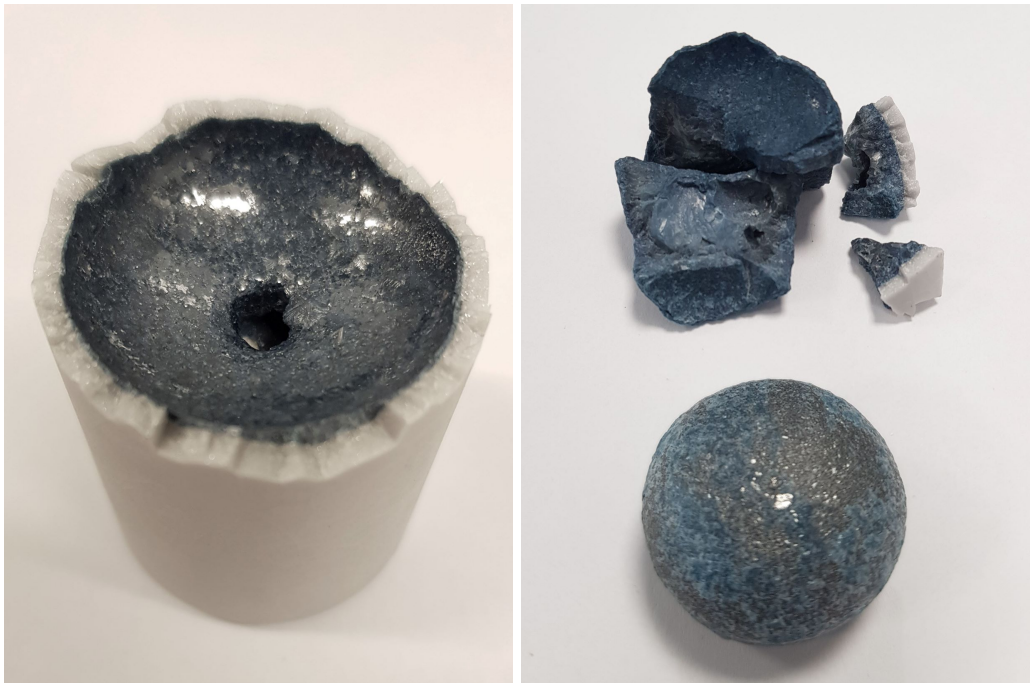

(a) The top of the slag after removing the upper part of the crucible.

(b) The slag and metal after crushing and removing the slag from the larger parts.

Figure 4.2: Crucible contents from experiment 2.

In figure 4.2 the crucible contents from experiment 2 is shown. The slag from this experiment was blue in colour, and contained a large cavity from solidification. It was somewhat brittle, and cracked upon removal of the metal. The crucible was not removed from the piece of slag selected for EPMA analysis, so a picture of the slag-crucible boundary can be seen in appendix C. A fine layer of slag covered the metal from this experiment, and was removed by sand blasting together with some crucible material bonded to the underside of the metal.

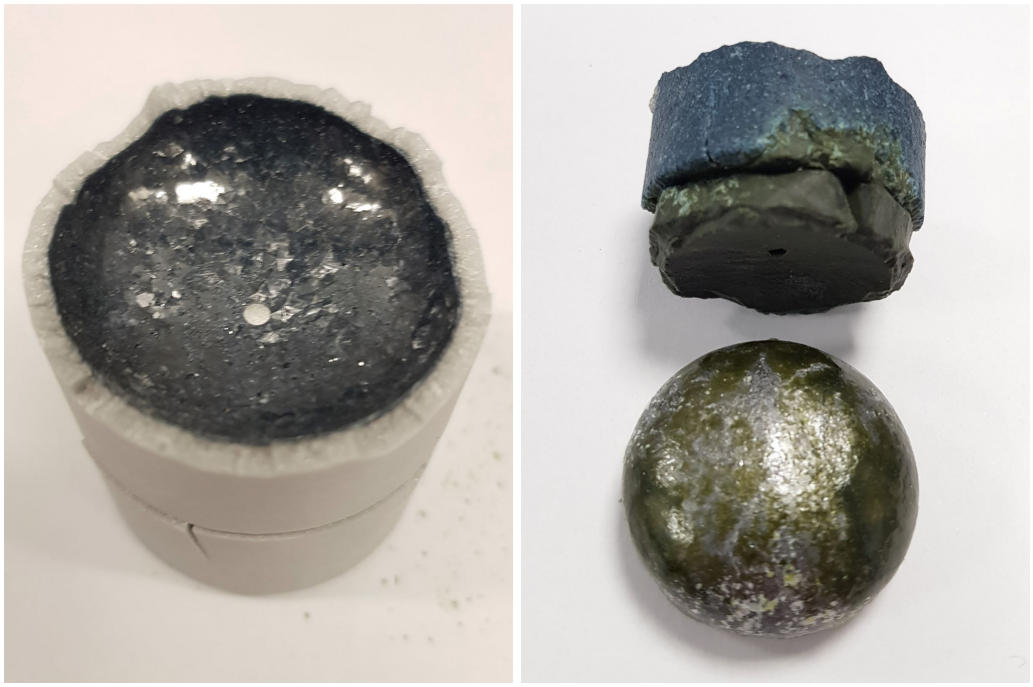

(a) The top of the slag after removing the upper part of the crucible.

(b) The slag and metal after removing the crucible.

Figure 4.3: Crucible contents from experiment 3.

The crucible contents from experiment 3 is shown in figure 4.3. In figure 4.3a the surface of the slag is blue and similar to the one from experiment 2. As can be seen in figure 4.3b however, the slag seemed to actually have separated into two phases. Care was taken during processing of this slag to ensure a representative sample for XRF, as well as selecting a piece containing both phases for EPMA. The green slag phase was the one solidifying in contact with the metal, and sand blasting was used to remove some remnants from the metal surface.

(a) The top of the slag after removing the upper part of the crucible.

(b) The slag and metal after removing the crucible.

Figure 4.4: Crucible contents from experiment 4.

Figure 4.4 shows the slag and metal from experiment 4. The slag was brown/gray in colour and was significantly more porous than that of other experiments. No slag remnants had to be removed from the metal, but the metal protrusion visible in figure 4.4b caused cracking of the slag upon separation.

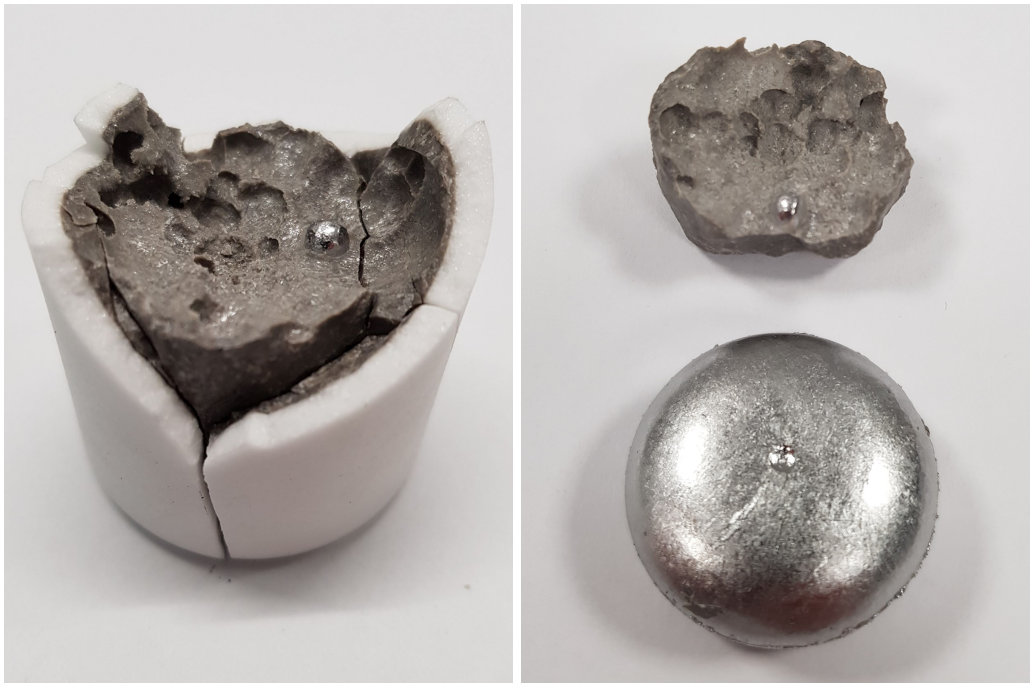

(a) The top of the slag after removing the upper part of the crucible.

(b) The slag and metal after removing the crucible.

Figure 4.5: Crucible contents from experiment 5.

In figure 4.5 the contents of the crucible after refining experiment 5 is shown. As seen in figure 4.5a the gray slag was brittle, and seemed to have cracked during cooling. Unlike what was observed in other experiments, a fine slag layer covered the metal on all sides, seemingly preventing metal-crucible contact during solidification. This slag did not adhere to the metal, but was rather strongly bonded to the crucible.

Finally, the crucible contents of experiment 6 is shown in figure 4.6. The slag seemed similar in appearance to the slag from experiment 5, but did not crack as easily. It left some remnants on the metal as seen in figure 4.6b, which again were removed by sand blasting.

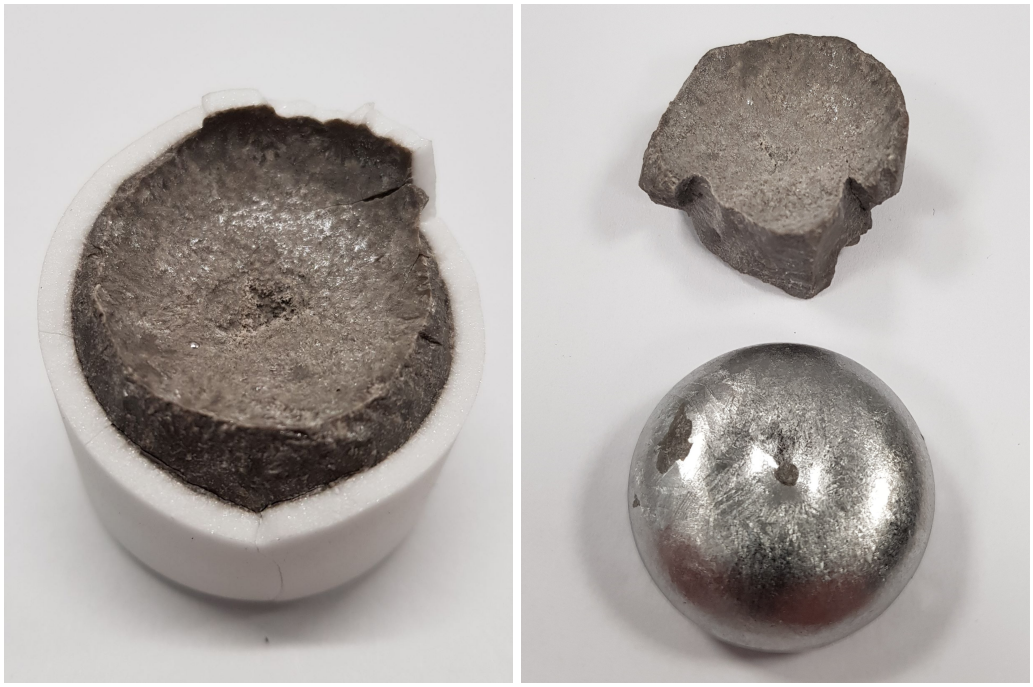

(a) The top of the slag after removing the upper part of the crucible.

(b) The slag and metal after removing the crucible.

Figure 4.6: Crucible contents from experiment 6.

In general, the slag appeared more varied than the metal upon inspection. The slags from experiments 1-3 were more colourful, less brittle and seemed to adhere more to the metal than the slags from experiments 4-6. All slags were bonded to the walls of the crucible to the point where sand blasting had to be used for all samples. The metal was not pictured after removal of slag remnants, but it could be noted that the metal samples from experiments 1-3 seemed darker in colour than the ones from experiments 4-6. The shape and position of slag and metal in the crucible reveals a high difference in density between the two phases. The wettability of the metal seems to be low towards both slag and crucible, compared to the apparent high wettability between the slag and crucible walls.

4.2 Metal analysis

The metal from the refining experiments was examined using EPMA for microstructure analysis, as well as XRF and combustion analysis to learn the average chemical composition of the metal. This chemical composition is shown in table 4.1. Here, carbon content is found by combustion analysis and the rest by XRF.

Table 4.1: Results of chemical analysis on refined metal done by Sintef Norlab.

Element	**Sample 1**	**Sample 2**	**Sample 3**	**Sample 4**	**Sample 5**	**Sample 6**
C (wt%)	2,42	2,26	1,98	0,19	0,09	0,02
Ti (wt%)	-	0,16	0,46	-	-	-
Al (wt%)	0,09	0,06	0,09	0,09	0,05	0,06
Co (wt%)	0,052	0,044	0,044	0,043	0,047	0,045
Cr (wt%)	0,012	0,009	0,011	0,020	0,022	0,021
Cu (wt%)	0,012	-	-	-	0,030	0,046
Mn (wt%)	0,09	0,011	0,009	0,006	0,010	0,006
Ni (wt%)	-	-	-	-	0,008	-
Si (wt%)	-	0,04	0,06	0,04	0,04	0,07
V (wt%)	-	0,002	-	-	-	-

These results show carbon levels comparable to the initial amount of 2,75 wt% for samples 1-3, and significantly lower levels for samples 4-6. Titanium was only detected in samples 2 and 3. The lower detection limit for titanium with this technique is 0,020 wt%, meaning that samples 1, 4, 5 and 6 contain less than this.

Figure 4.7 contains BSE images of the metal samples. Larger versions are available in appendix B together with pictures taken at lower magnification. Particles of TiC were found in samples 2 and 3, along with some MgO particles in sample 2. X-ray maps of these samples are therefore shows in figure 4.8. Table 4.2 contains the results from WDS analysis of the metal, including the aforementioned particles. The darker areas in other samples were found to be pores.

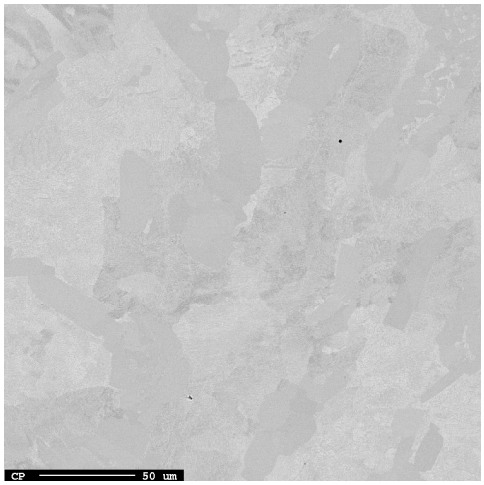

(a) Sample 1 at x400 magnification.

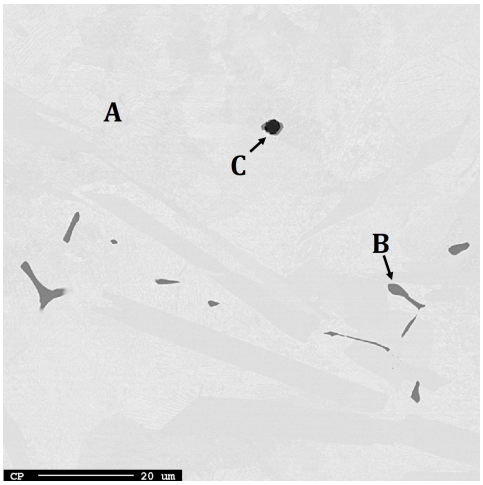

(b) Sample 2 at x1000 magnification.

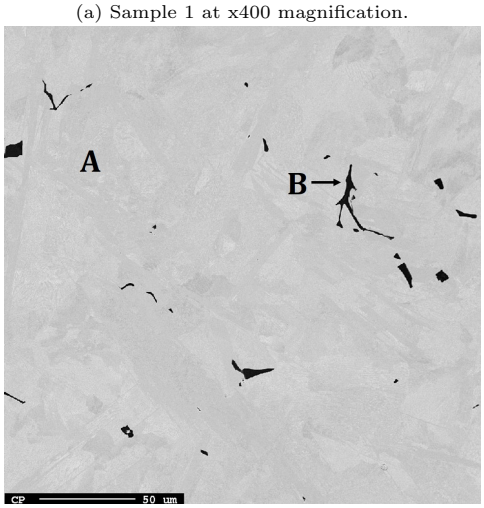

(c) Sample 3 at x400 magnification.

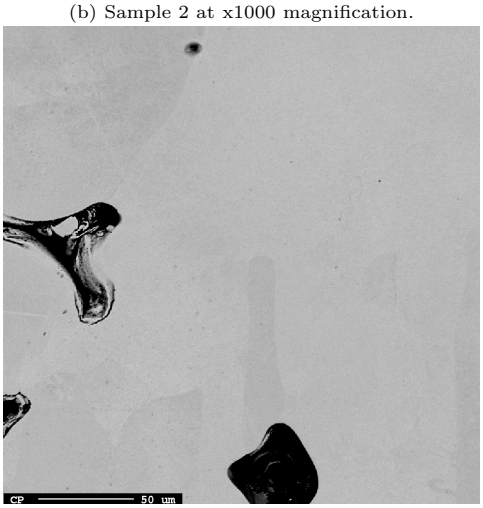

(d) Sample 4 at x400 magnification.

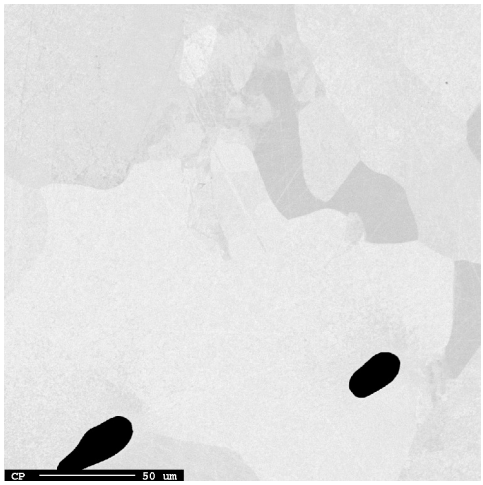

(e) Sample 5 at x400 magnification.

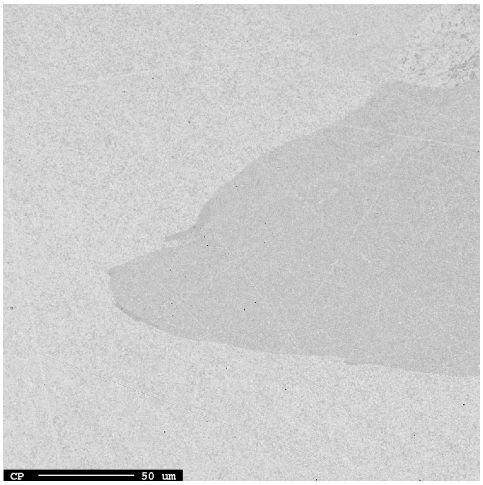

(f) Sample 6 at x400 magnification.

Figure 4.7: Backscatter images of the metal samples from refining experiments. The phases compositions are shown in table 4.2. Larger versions without labelling are available in appendix B.

Table 4.2: Chemical composition of the samples in figure 4.7. The results are averages of three point-analysis done using WDS.

Sample/area		Al	Mg	Ti	Fe	Ca	C	O	Total
1	wt%	0,00	0,00	0,01	96,29	0,00	3,25	0,00	99,55
	σ	0,00	0,00	0,01	2,26	0,00	1,13	0,00	1,14
2A	wt%	0,00	0,01	0,02	100,42	0,00	1,41	0,00	101,86
	σ	0,00	0,02	0,01	0,39	0,00	0,30	0,00	0,20
2B	wt%	0,00	0,00	79,08	4,70	0,00	18,43	0,00	102,21
	σ	0,01	0,01	0,19	0,33	0,00	0,07	0,00	0,35
2C	wt%	0,01	62,48	2,23	6,98	0,18	2,57	36,90	111,34
	σ	0,02	5,22	1,29	2,23	0,02	0,62	1,88	4,19
3A	wt%	0,06	0,02	0,04	100,64	0,00	1,24	0,00	102,00
	σ	0,01	0,02	0,00	0,27	0,00	0,02	0,00	0,27
3B	wt%	0,00	0,01	80,56	4,00	0,00	19,06	0,00	103,63
	σ	0,00	0,01	0,21	0,09	0,00	0,20	0,00	0,46
4	wt%	0,00	0,00	0,01	101,32	0,00	0,77	0,00	102,10
	σ	0,00	0,00	0,01	0,06	0,00	0,01	0,00	0,07
5	wt%	0,00	0,01	0,00	101,05	0,00	0,31	0,00	101,37
	σ	0,00	0,01	0,00	0,16	0,00	0,02	0,00	0,20
6	wt%	0,00	0,00	0,01	98,61	0,00	0,29	0,00	98,91
	σ	0,00	0,01	0,02	1,39	0,00	0,01	0,00	1,42

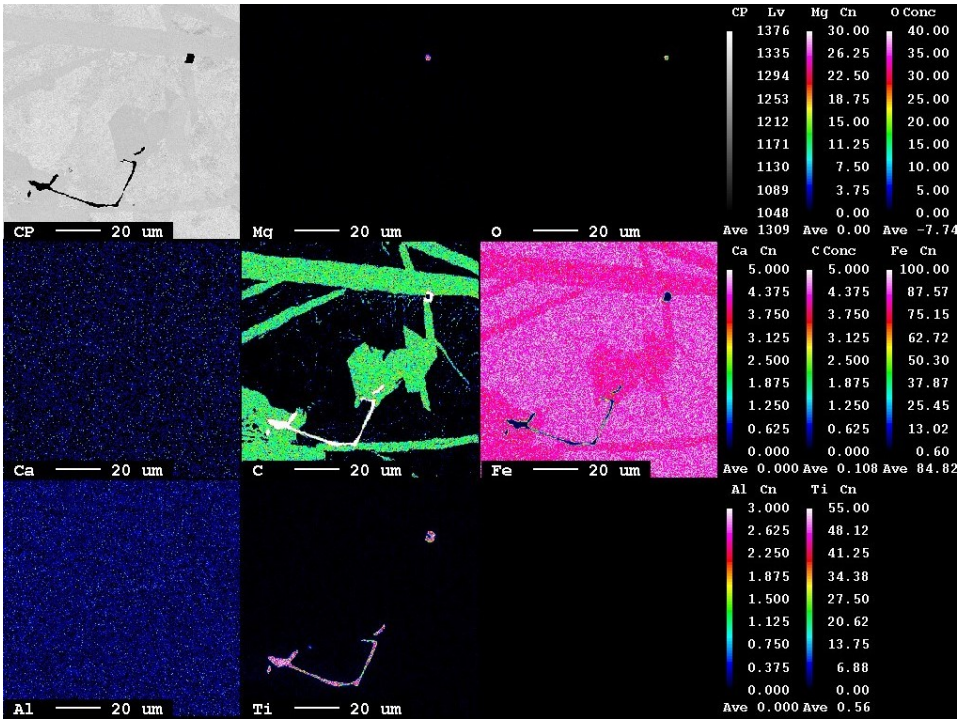

(a) MgO and TiC particles in sample 2 at x1000 magnification.

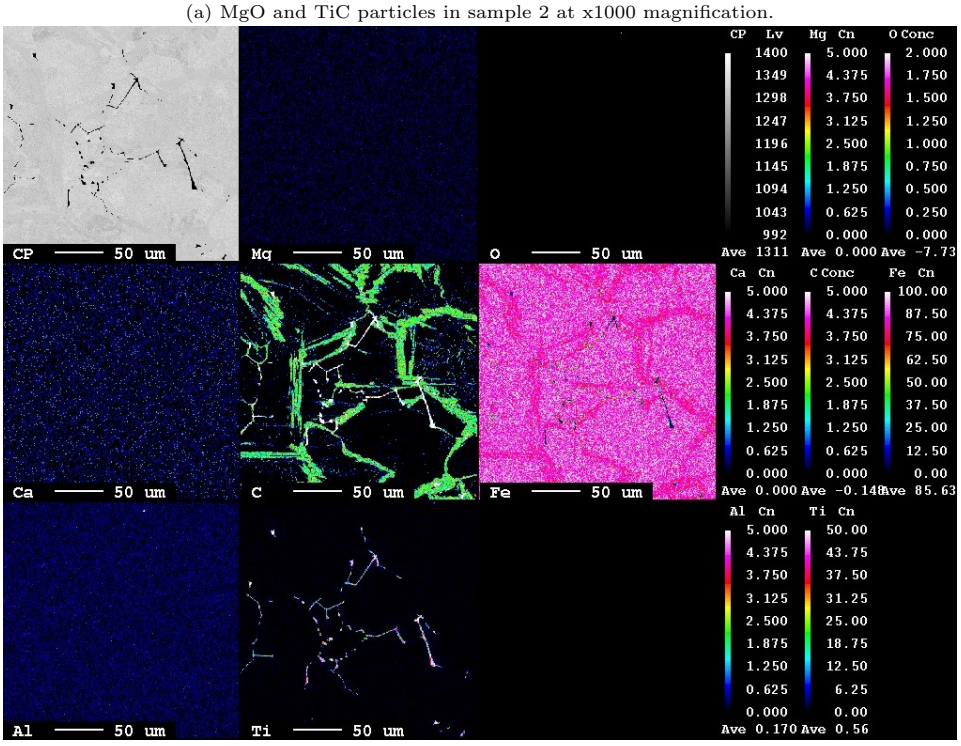

(b) TiC particles in sample 3 at x400 magnification.

Figure 4.8: X-ray maps of particles in metal samples.

4.3 Slag analysis

The slag from the refining experiments was examined using XRF and EPMA. A semi-quantitative measurement of the average oxide content of each sample is produced from the former, shown in table 4.3. The latter provides insight into the internal structure of the slag, and is presented sample by sample.

Table 4.3: Results of XRF-analysis on refining slag. LOI indicates loss on ignition. Results are semi-quantitative.

Sample	**1**	**2**	**3**	**4**	**5**	**6**
MgO (wt%)	7,96	7,96	8,16	9,00	10,25	9,66
Al_2O_3 (wt%)	44,36	44,53	44,82	43,83	42,55	41,97
SiO_2 (wt%)	0,20	0,20	0,18	0,91	0,99	1,08
P_2O_5 (wt%)	0,01	0,01	0,01	0,01	0,01	0,01
SO_3 (wt%)	0,02	0,01	0,01	0,10	0,11	0,07
CaO (wt%)	42,73	43,27	43,34	42,03	40,85	40,52
TiO_2 (wt%)	0,79	1,31	1,20	0,38	1,78	3,06
Cr_2O_3 (wt%)	-	-	-	0,01	0,02	0,02
Fe_2O_3 (wt%)	0,13	0,07	0,05	1,32	1,57	1,84
SrO (wt%)	0,02	0,02	0,02	0,02	0,02	0,02
Mn_2O_3 (wt%)	0,01	0,01	0,01	0,03	0,04	0,04
LOI (wt%) 1000 °C	1,18	0,50	-0,28	-0,05	-0,02	-0,06
Sum (wt%)	97,40	97,89	97,51	97,60	98,16	98,25

In the above table, we see that all slags contain significant amounts of MgO. The amount of TiO_2 in slag sample 4 is also inconsistenly low, and may be incorrect.

4.3.1 Sample 1

When studied using EPMA, the slag from experiment 1 was revealed to contain 3 clearly distinguishable phases as well as small, elongated particles too small to analyse. These are all shown in figure 4.9 with the phases labelled A-C from lightest to darkest. More BSE images of the slag are shown in appendix C.

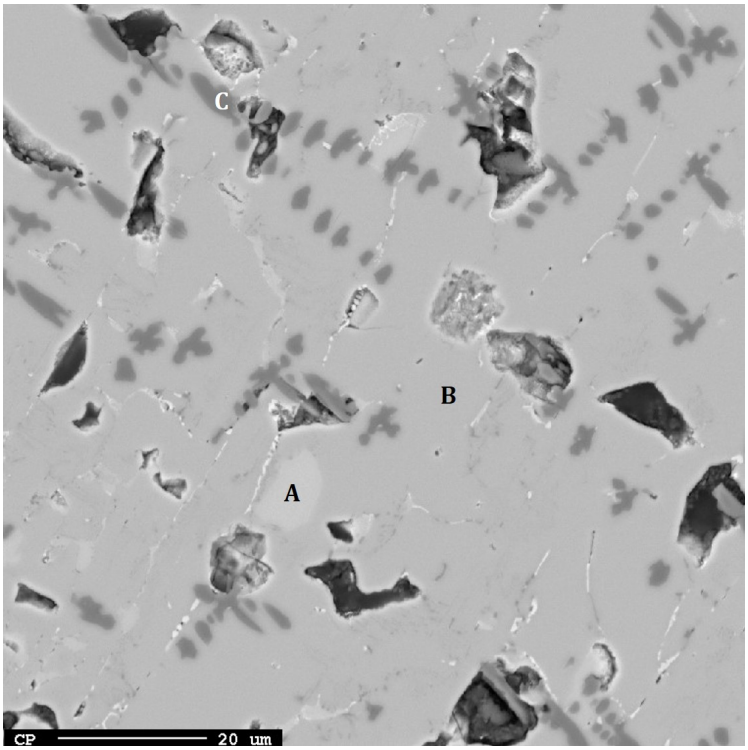

Figure 4.9: Backscatter image of the slag from experiment 1 at x1000 magnification. The phases are labelled according to table 4.4

The chemical composition of the main phases are shown in table 4.4. These values are averages of analysis done at 3 points each, of which the standard deviation is also shown. An x-ray map of the cross section also is included in figure 4.10. We see that the dendrittic areas labelled C are mostly MgO and that the small particles contain most of the titanium in the slag.

Table 4.4: Chemical composition of the phases visible in figure 4.9. The results are averages of three point-analysis done using WDS.

Area		**MgO**	**CaO**	**FeO**	**Al_2O_3**	**TiO_2**	**Total**
A	wt%	0,77	61,11	0,04	38,11	0,78	100,82
	σ	0,10	0,36	0,02	0,22	0,06	0,52
B	wt%	1,17	46,97	0,02	52,38	0,37	100,91
	σ	0,07	0,35	0,01	0,11	0,02	0,48
C	wt%	97,99	1,83	0,24	1,94	0,11	102,12
	σ	0,84	0,28	0,06	0,26	0,12	0,27

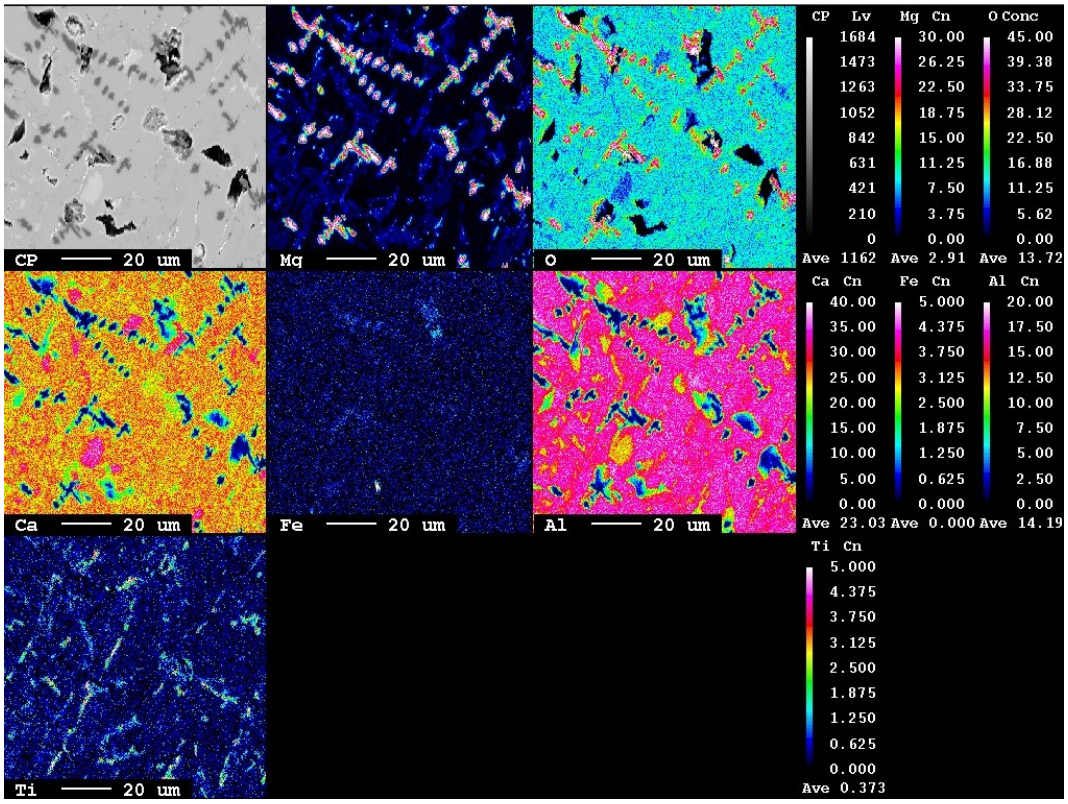

Figure 4.10: X-ray map of the cross section displayed in figure 4.9.

4.3.2 Sample 2

In the BSE images of sample 2, shown in figure 4.11, we see similar phases as in sample 1. The bright, elongated particles seem however to intrude more into the other phases. Particularly in the areas labelled A there seems to be a mixture of these particles and another phase. More images of this sample are available in appendix C, including figure C.2a showing the slag-crucible interface.

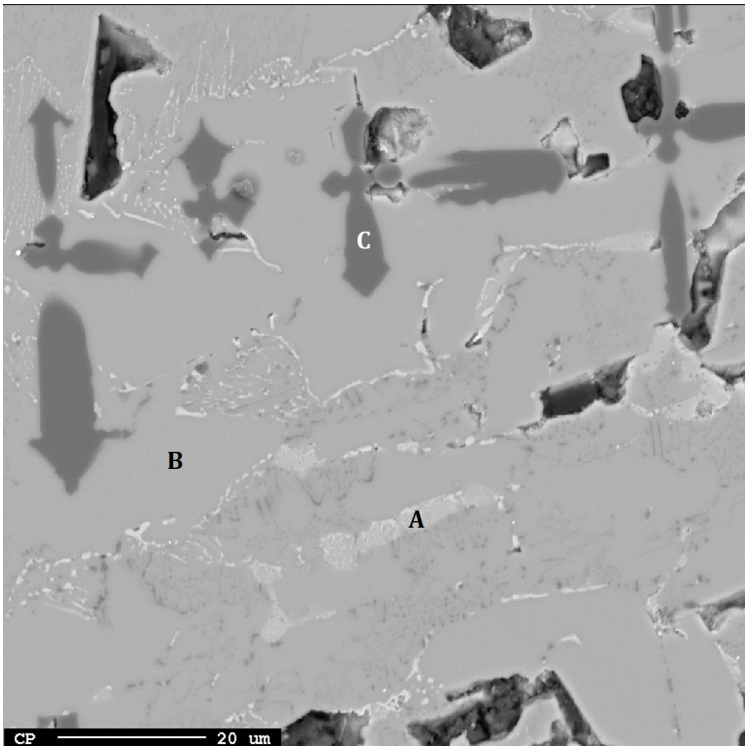

Figure 4.11: Backscatter image of the slag from experiment 2 at x1000 magnification. The phases are labelled according to table 4.5

Table 4.5 shows the measured chemical composition of the areas visible in sample 2. Due to the inhomogeniety of the areas labelled A, the point measurements were done unfocused, providing average data from a small area. This is reflected in the greater standard deviation for these values. The x-ray map of the sample, shown in figure 4.12, reveal that while the particles are rich in titanium similarly to the ones in sample 1, the difference to the areas around is less distinct.

Table 4.5: Chemical composition of the phases visible in figure 4.11. The results are averages of three point-analysis done using WDS.

Area		**MgO**	**CaO**	**FeO**	**Al_2O_3**	**TiO_2**	**Total**
A	wt%	1,28	55,70	0,01	40,46	3,61	101,06
	σ	0,62	4,45	0,01	7,62	2,56	2,03
B	wt%	1,18	47,04	0,00	52,48	0,50	101,20
	σ	0,03	0,09	0,01	0,06	0,03	0,07
C	wt%	98,35	1,66	0,04	1,60	0,06	101,70
	σ	1,00	0,59	0,02	0,11	0,01	0,38

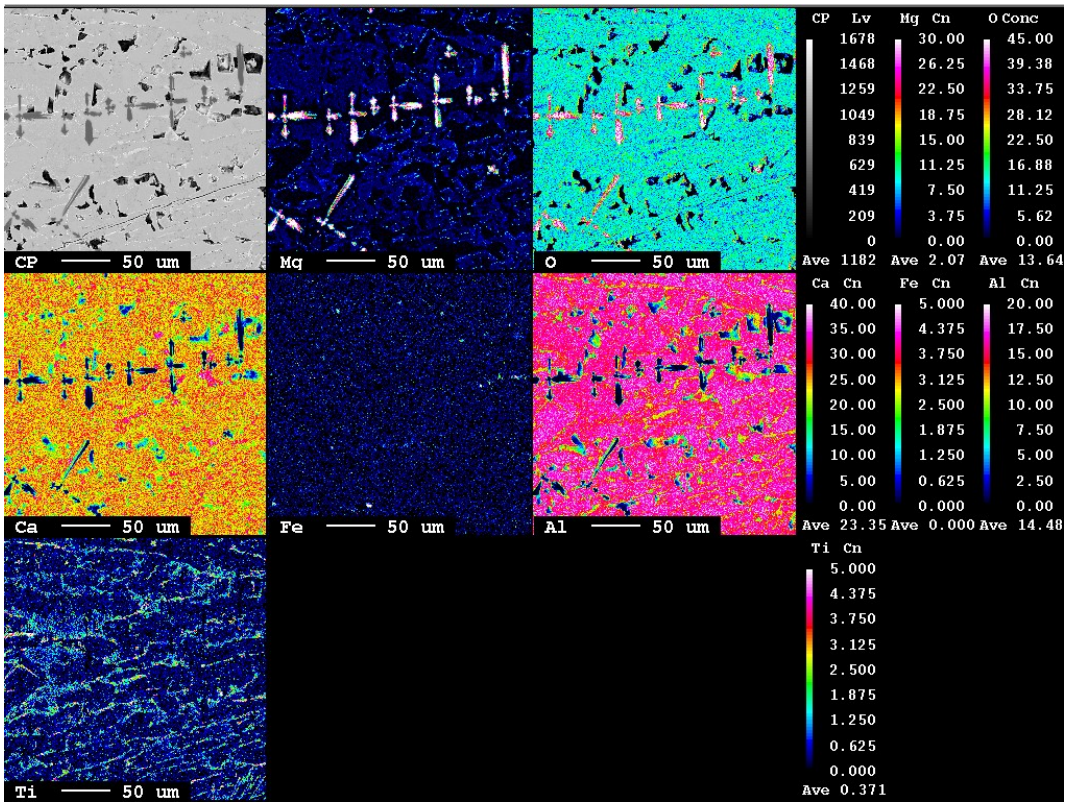

Figure 4.12: X-ray map of the cross section displayed in figure 4.11

4.3.3 Sample 3

As the slag from experiment 3 was separated into two distinctly coloured areas, EPMA analysis was done on both to reveal the difference. As can be seen in figure 4.13, the blue parts of the slag seem to be similar to the slags in samples 1 and 2. The green parts seem to be much more homogeneous.

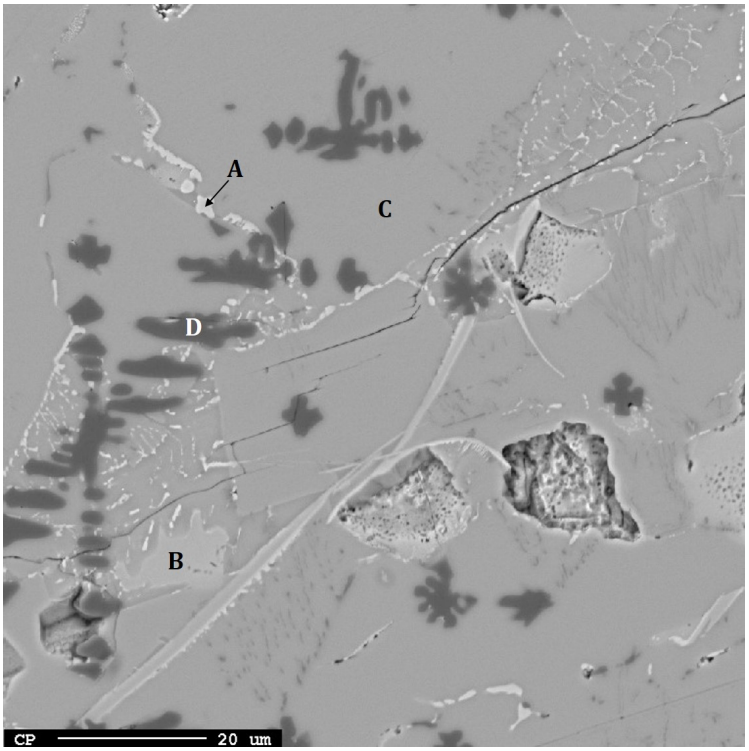

(a) Blue area

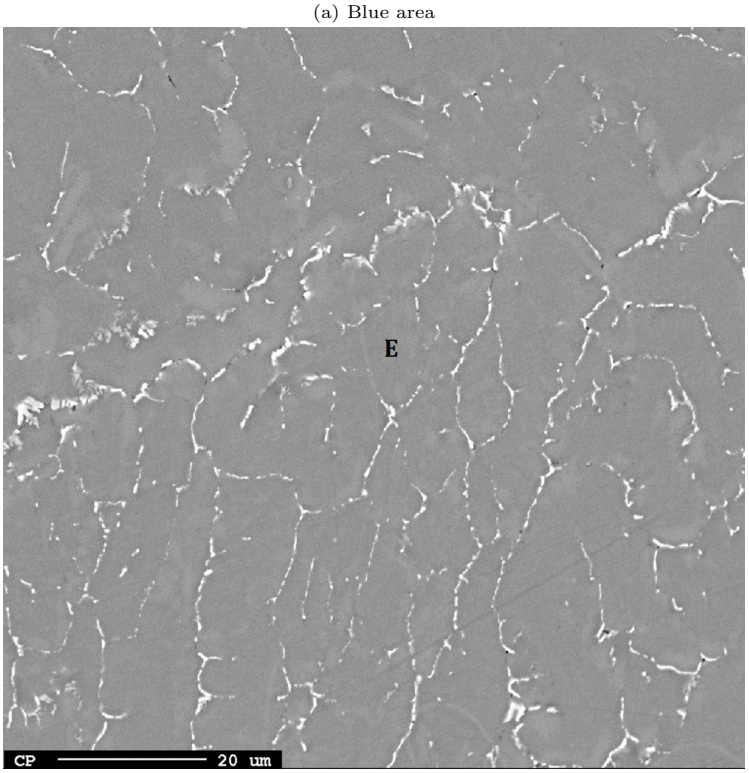

(b) Green area

Figure 4.13: Backscatter images of the slag from experiment 3 at x1000 magnification. The phases are labelled according to table 4.6

Table 4.6 shows the measured chemical composition of the areas in sample 3, as labelled in figure 4.13. X-ray maps of the two areas are shown in figure 4.14. In the blue area we again see particles rich in titanium as well as MgO-dendrites in a matrix of various CaO-Al_2O_3 phases. In the green are we also se particles rich in titanium, that appear to have formed along grain boundaries in a matrix having a similar composition to the average composition of the sample, as shown in table 4.3.

Table 4.6: Chemical composition of the phases visible in figure 4.13. The results are averages of three point-analysis done using WDS.

Area		**MgO**	**CaO**	**FeO**	**Al_2O_3**	**TiO_2**	**Total**
A	wt%	0,87	61,13	0,01	38,81	0,58	101,39
	σ	0,06	0,43	0,01	0,24	0,09	0,54
B	wt%	1,04	47,18	0,00	53,30	0,33	101,85
	σ	0,02	0,21	0,00	0,06	0,03	0,26
C	wt%	7,54	44,28	0,01	50,16	0,39	102,38
	σ	1,25	0,69	0,01	0,74	0,06	0,11
D	wt%	96,81	2,99	0,04	2,70	0,09	102,62
	σ	3,09	1,35	0,02	0,58	0,09	1,33
E	wt%	9,36	44,68	0,04	46,92	0,78	101,78
	σ	0,86	0,48	0,01	0,99	0,08	0,72

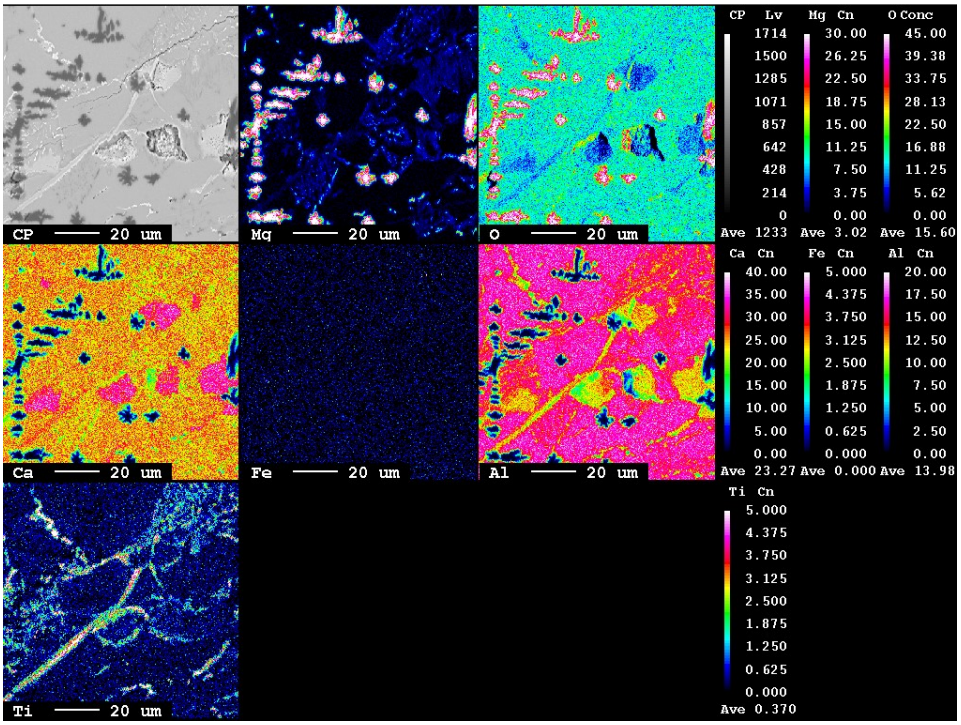

(a) Blue area.

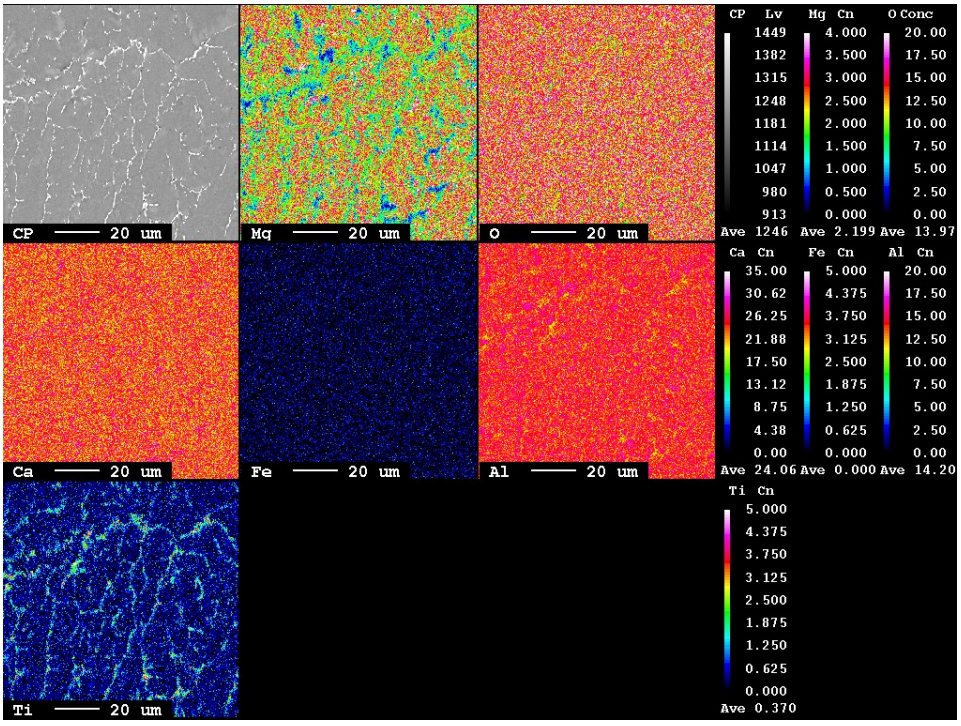

(b) Green area.

Figure 4.14: X-ray maps of the cross sections displayed in figure 4.13.

4.3.4 Sample 4

In figure 4.15 we see a BSE-image of the slag from sample 4. Four distinctly different areas are visible, labelled A-D. More pictures are shown in appendix C.

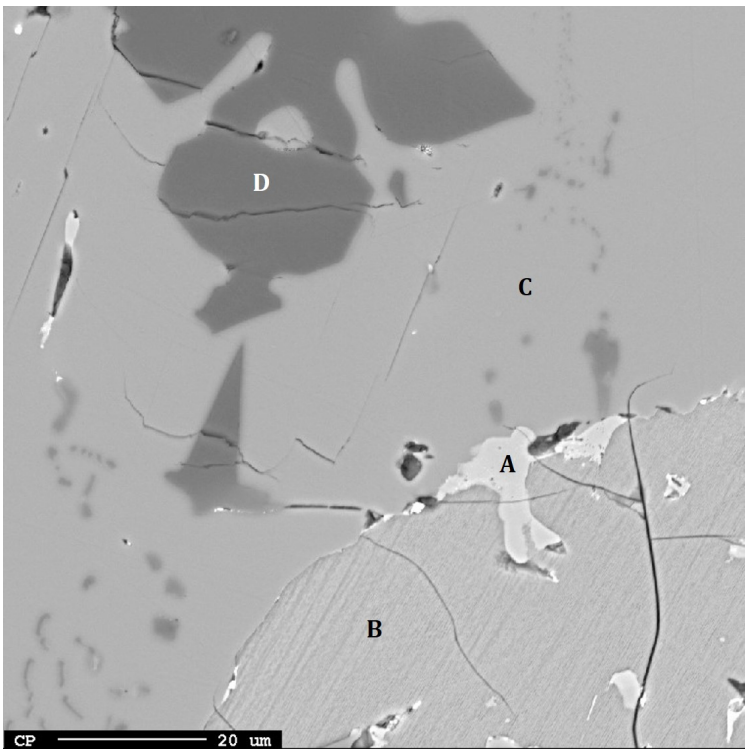

Figure 4.15: Backscatter image of the slag from experiment 4 at x1000 magnification. The phases are labelled according to table 4.7

Table 4.7 shows the measured chemical composition of the areas in shown above. The relatively high standard deviation of the values for area A should be noted, and may stem from either contamination from other areas, or from possibly confusing two similar-looking areas as the same and using both for the WDS-analysis. The x-ray map in figure 4.16 does somewhat support the values in the table however, at least for the visible particle.

Table 4.7: Chemical composition of the phases visible in figure 4.15. The results are averages of three point-analysis done using WDS.

Area		MgO	CaO	FeO	Al_2O_3	TiO_2	Total
A	wt%	1,37	46,56	6,25	24,69	16,99	95,87
	σ	0,54	2,04	6,53	8,64	13,75	2,91
B	wt%	0,47	59,46	0,79	36,93	0,33	97,98
	σ	0,06	0,15	0,12	0,43	0,08	0,35
C	wt%	0,80	47,19	0,36	52,82	0,10	101,27
	σ	0,08	0,23	0,11	0,33	0,05	0,53
D	wt%	97,64	0,91	3,59	1,09	0,03	103,25
	σ	1,02	0,02	1,57	0,16	0,03	0,59

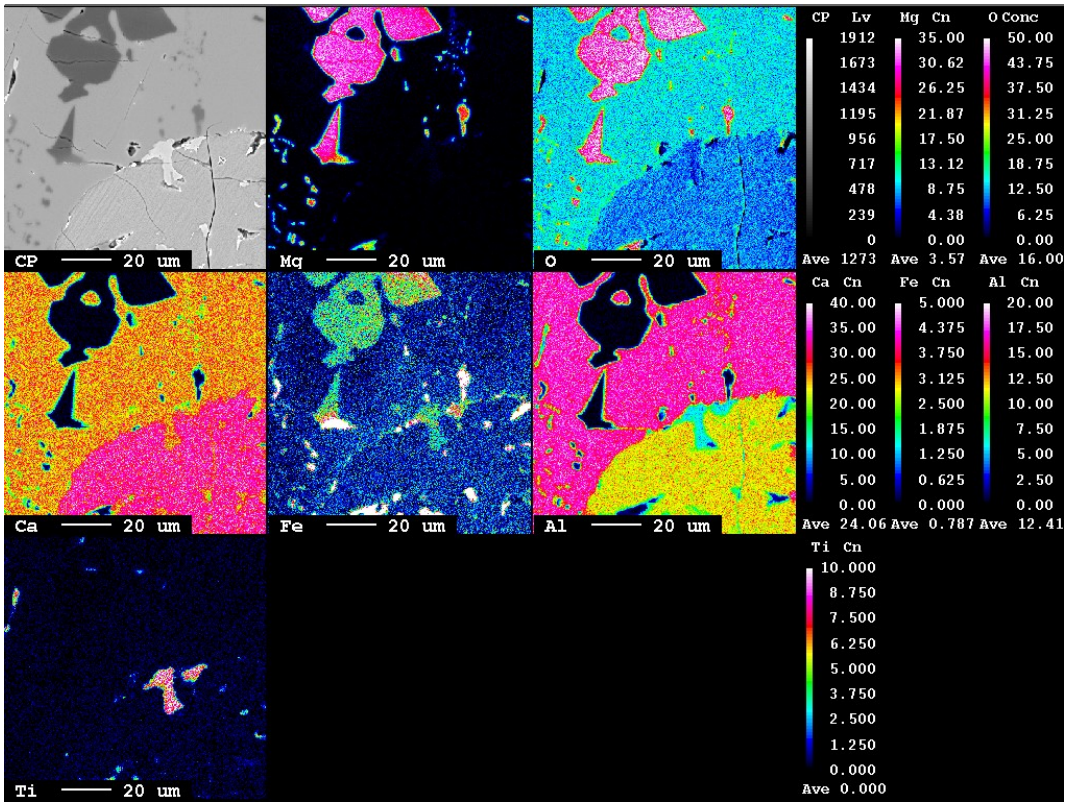

Figure 4.16: X-ray map of the cross section displayed in figure 4.15.

4.3.5 Sample 5

A cross-section of the slag from experiment 5 with four labelled areas is pictured in figure 4.17. There are larger particles present, labelled A, as well as areas containing a mixture of at least two phases, labelled B.

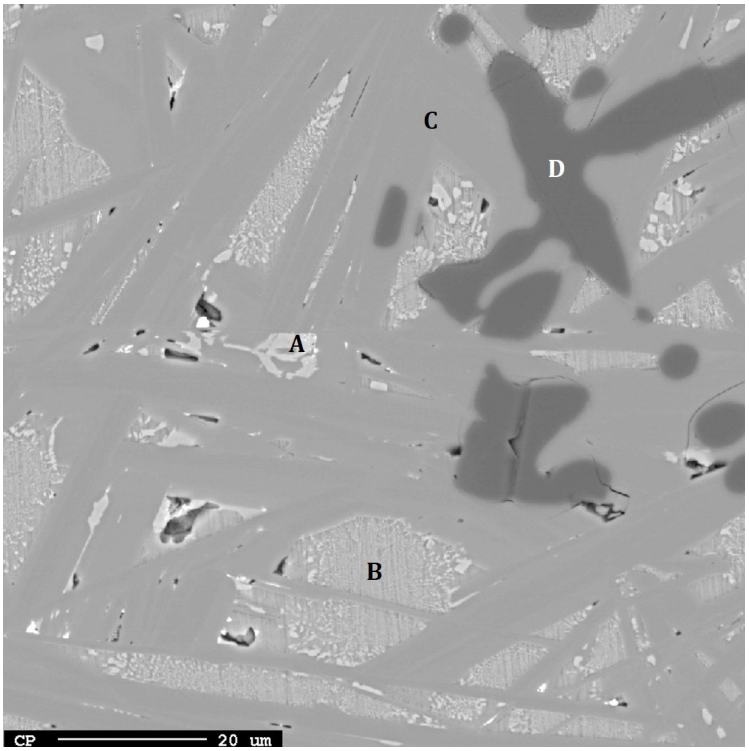

Figure 4.17: Backscatter image of the slag from experiment 5 at x1000 magnification. The phases are labelled according to table 4.8

Table 4.8 shows the results from WDS-analysis of sample 5. Despite the analysis points being unfocused for areas labelled B and the particles labelled A being somewhat mixed with the matrix, the table shows low standard deviation values compared to that of other samples. An x-ray map, showing the distribution of various elements in the sample, is shown in figure 4.18.

Table 4.8: Chemical composition of the phases visible in figure 4.17. The results are averages of three point-analysis done using WDS.

Area		MgO	CaO	FeO	Al_2O_3	TiO_2	Total
A	wt%	1,61	47,73	1,42	21,36	26,18	98,30
	σ	0,41	1,29	0,32	1,78	1,76	1,10
B	wt%	1,09	57,20	0,69	32,15	6,34	97,46
	σ	0,13	0,22	0,15	0,53	0,77	0,79
C	wt%	7,87	40,93	1,09	49,70	0,13	99,72
	σ	0,79	0,37	0,22	0,24	0,05	1,22
D	wt%	93,77	1,12	3,97	1,34	0,03	100,23
	σ	0,54	0,08	0,72	0,06	0,02	0,30

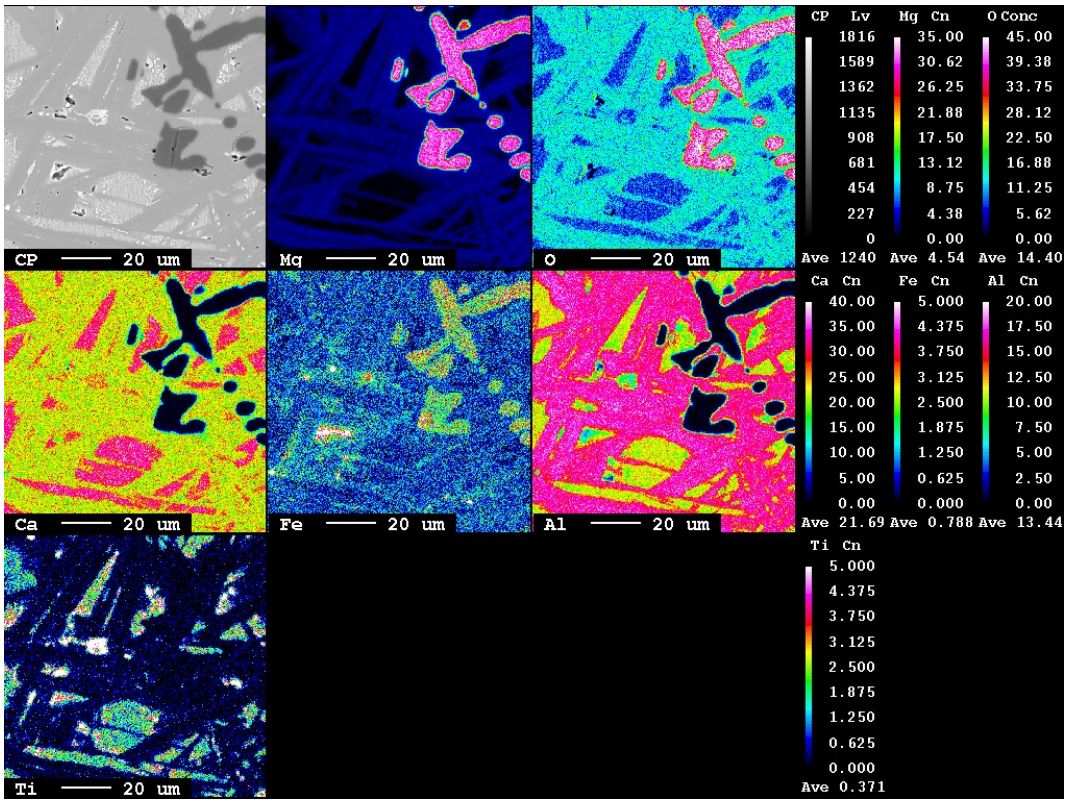

Figure 4.18: X-ray map of the cross section displayed in figure 4.17.

4.3.6 Sample 6

In sample 6, pictured in figure 4.19, we only see 3 clearly distinct areas: The dark dendrites labelled C, the matrix labelled B, and a mixed area with the label A. Compared to the mixed areas in sample 5, the ones in this sample contain much larger particles.

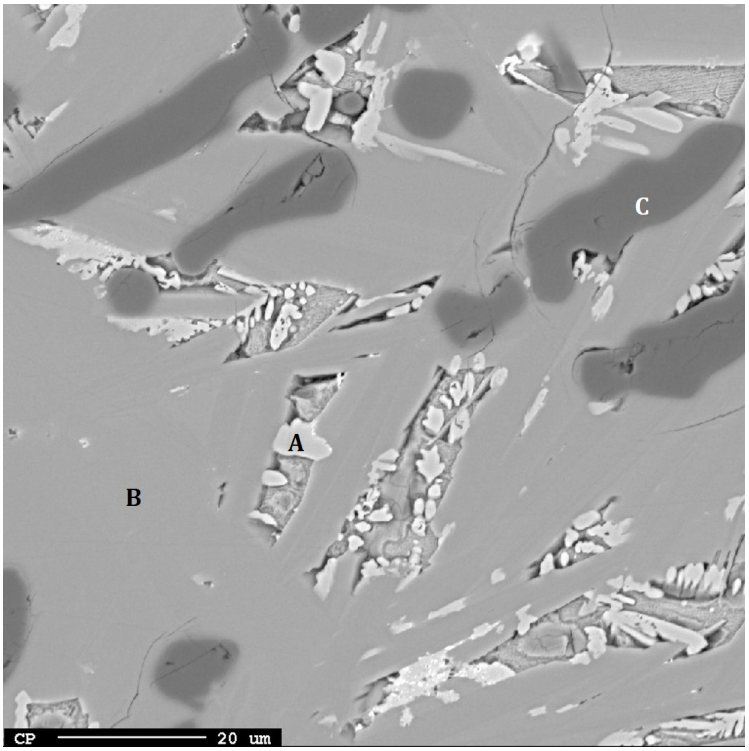

Figure 4.19: Backscatter image of the slag from experiment 6 at x1000 magnification. The phases are labelled according to table 4.9

Table 4.9 shows the chemical composition of the areas visible above. In area A the point analysis was done in the lighter particles. The x-ray map in figure 4.20 shows that there is a slight difference between these particles and the rest of the areas, especially with regards to titanium content.

Table 4.9: Chemical composition of the phases visible in figure 4.19. The results are averages of three point-analysis done using WDS.

Area		MgO	CaO	FeO	Al_2O_3	TiO_2	Total
A	wt%	1,94	47,49	1,43	24,73	22,13	97,72
	σ	0,51	2,47	0,21	1,33	1,29	1,00
B	wt%	6,28	40,56	1,00	51,91	0,41	100,15
	σ	0,38	0,11	0,05	0,44	0,13	0,29
C	wt%	94,14	1,15	5,68	1,32	0,07	102,36
	σ	0,74	0,05	0,83	0,09	0,03	0,25

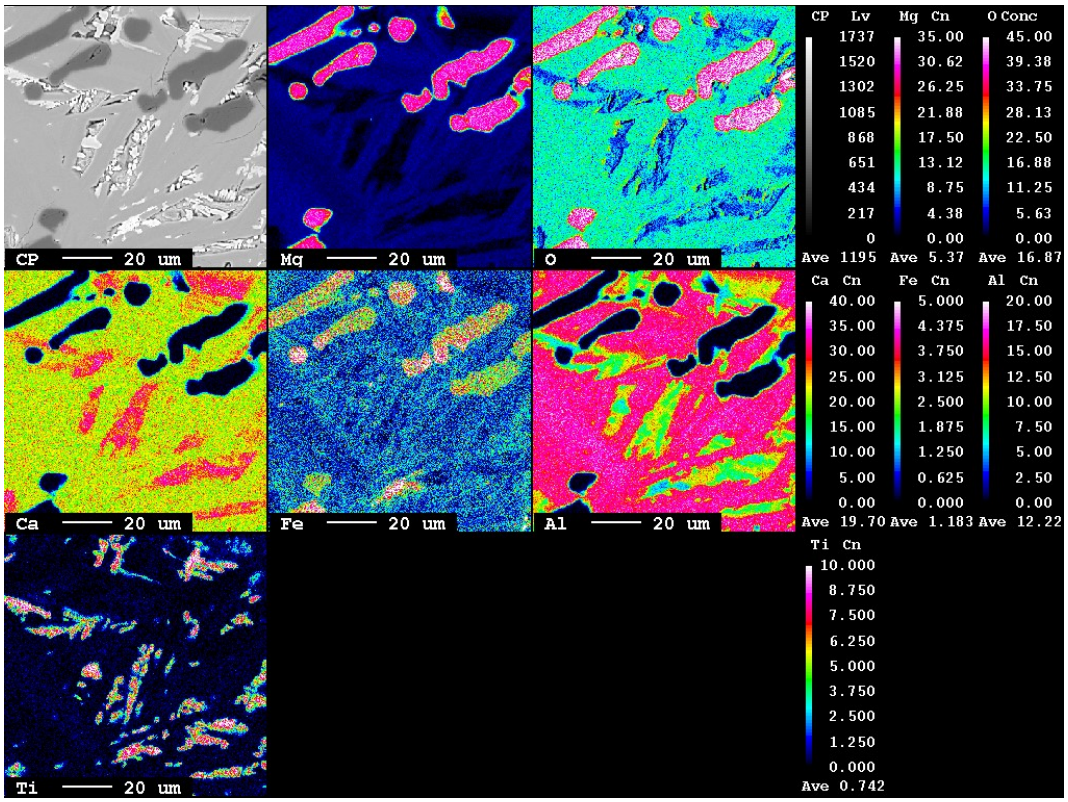

Figure 4.20: X-ray map of the cross section displayed in figure 4.19.

4.4 Model results

The model made for this project was used for two purposes: To calculate the energy of the individual slag and metal phases as a function of composition, and to predict the composition in both phases when they are in equilibrium with each other as a function of starting composition.

In figure 4.21, the calculated variation in Gibbs energy of a 1:1 CaO-Al_2O_3 slag is shown when a single form of iron or titanium oxide is added. The oxidation state of the metallic cations is here assumed to remain uniform and constant. In figure 4.22, the effect on Gibbs energy of varying the oxidation state of titanium and iron in the slag is shown.

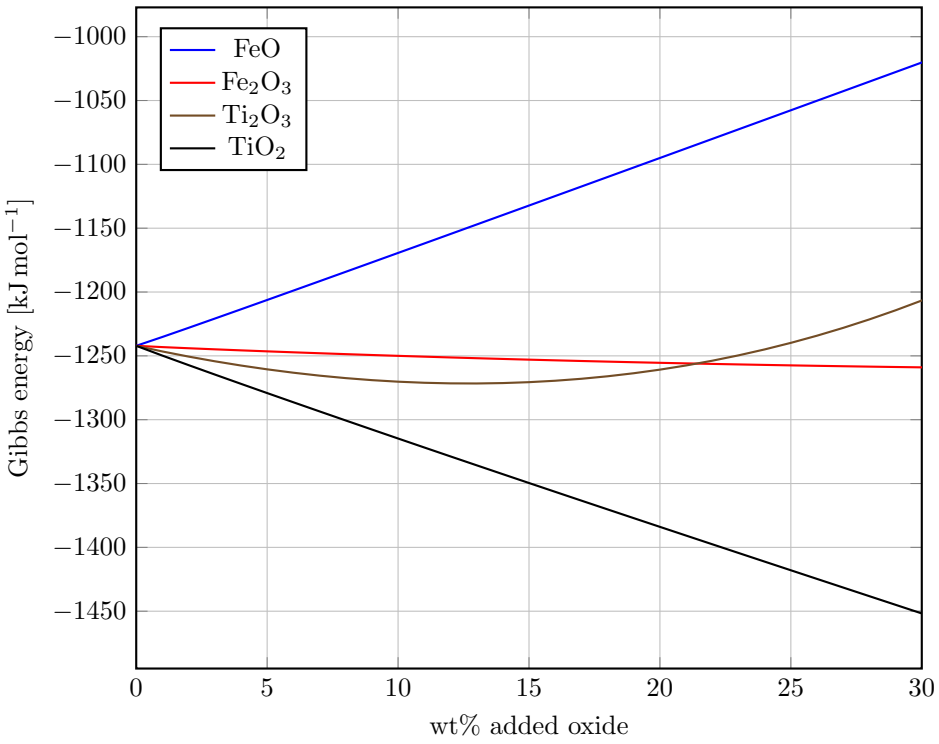

Figure 4.21: Calculated Gibbs energy in a 1:1 CaO-Al_2O_3 slag when adding iron or titanium oxides at 1600 °C

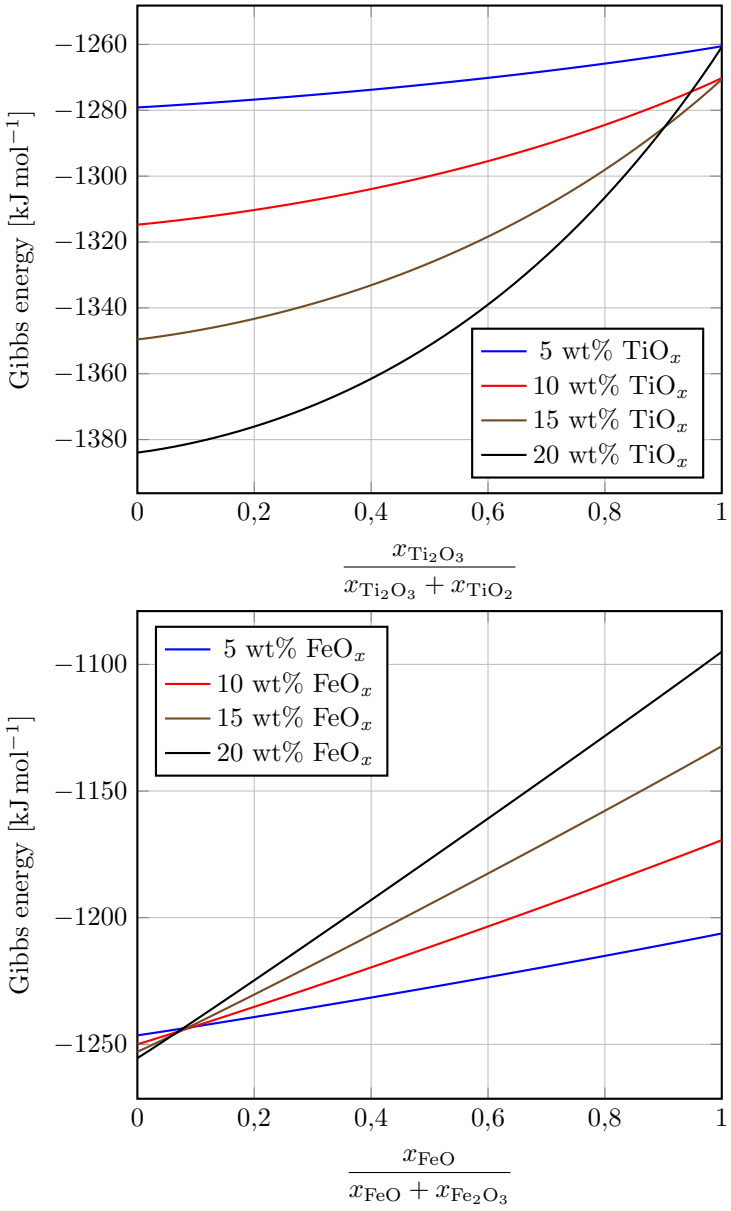

Figure 4.22: Calculated variation in the Gibbs energy of the slag depending on iron and titanium oxidation state.

In figure 4.23, the calculated energy of the metal phase is shown as a function of carbon and titanium content. The activity data for compositions below 95 wt% Fe is extrapolated from compositions above.

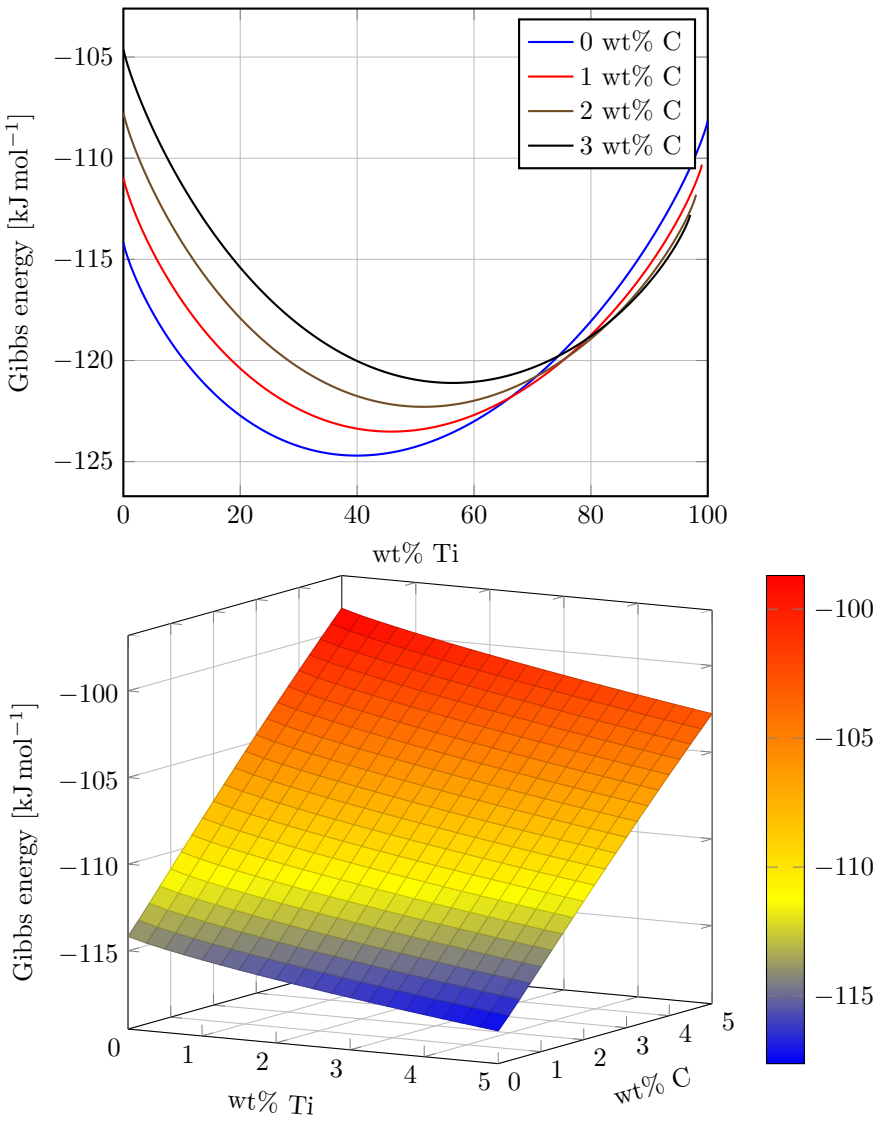

Figure 4.23: Calculated Gibbs energy in Fe-Ti$_x$-C$_x$ at 1600 °C.

The results from calculating the equilibrium compositions are shown in the figures below. In figure 4.24, the equilibrium content of both phases after starting with 0,5 wt% Ti in the metal is shown as a function of initial Fe_2O_3 in the slag. Figure 4.25 shows the calculation results after starting with 1,0 wt% Ti, and figure 4.26 shows this for 1,5 wt% Ti. The temperature is 1600 °C for all calculations. These calculations predict the preferential oxidation of titanium by formation of TiO_2.

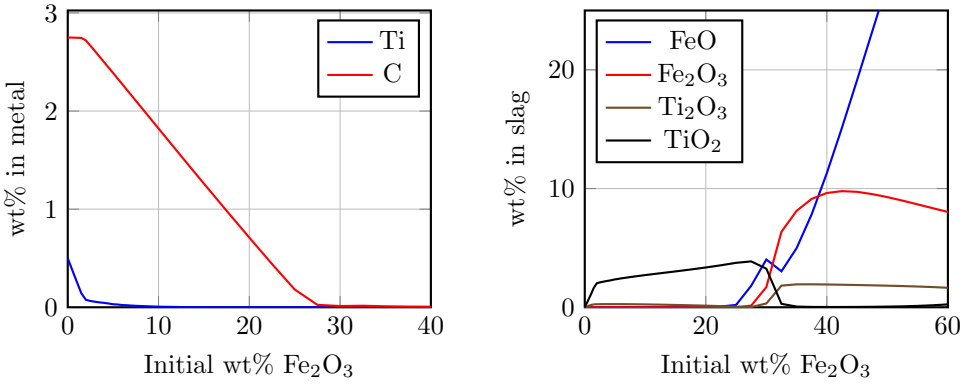

Figure 4.24: Calculated equilibrium phase content after refining of Fe-0,5Ti-C.

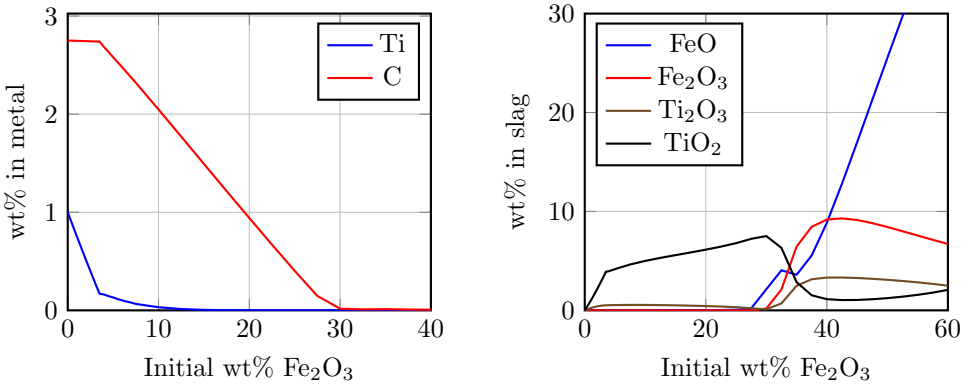

Figure 4.25: Calculated equilibrium phase content after refining of Fe-1,0Ti-C.

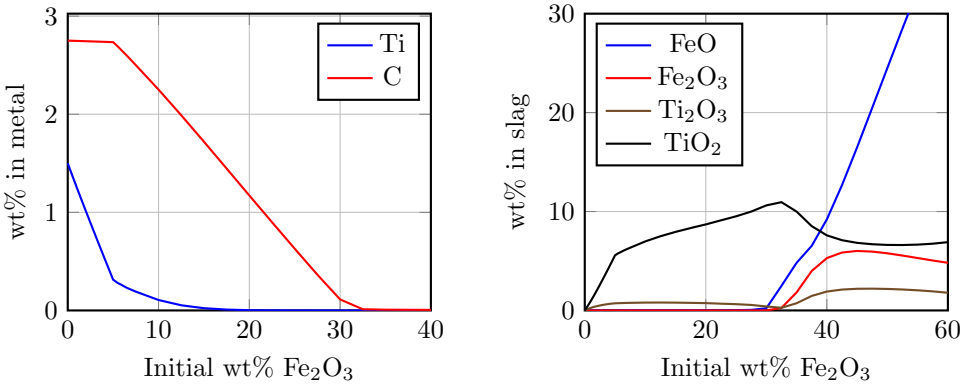

Figure 4.26: Calculated equilibrium phase content after refining of Fe-1,5Ti-C.

Chapter 5

Discussion

5.1 Implications of the model results

As seen in the figures of section 4.4, both the carbon and titanium is expected to be removed from the metal during refining. Figure 4.21 shows that there is a driving force in the slag to remove the titanium from the metal by forming TiO_2. The plot in figure 4.23 shows the opposite; titanium reduces the energy of the metal, while carbon increases it. Comparing the magnitudes of the energies shown on the y-axis on both plots gives an indication that the slag energy may dominate over the metal. This is confirmed in the equilibrium calculations in figures 4.24-4.26, which show that titanium is preferentially oxidised over carbon according to the model.

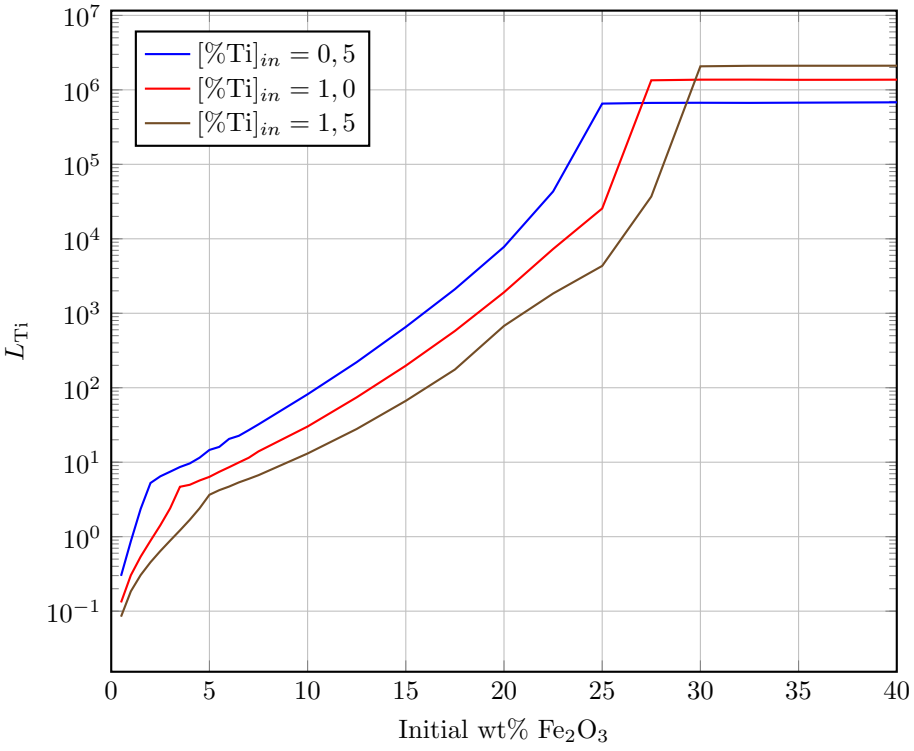

Figure 5.1: Calculated partition coefficients for titanium between the slag and metal phases.

For comparison with other results, it may be convenient to present the model results by the use of the partition coefficient L_{Ti} as described in section 2.6. This is shown in figure 5.1. In this figure we see three distinct regions: At very low amounts of iron oxide the carbon does not oxidise much, so the partition coefficients increase quickly. At high amounts of iron oxide most of the titanium is in the slag, so the partition coefficients are constant. The actual values in this region are mostly determined by the lower limits of titanium concentration imposed by the model. In the middle region the partition coefficients increase slowly with initial Fe_2O_3 content, as some of it is used to oxidise carbon as well as titanium.

These regions are recognisable also in figures 4.24-4.26. Here we see that carbon is not predicted to oxidise before the titanium level is below a certain amount, which happens at around 2-5 wt%. These calculations also predict that TiO_2 is the main form of titanium in the slag while the metal still contains some titanium. When Fe_2O_3 is added in excess however, Ti_2O_3 is formed to balance the formation of FeO as per reaction 5.1.

$$Fe_2O_3 + 2\,TiO_2 \rightleftharpoons 2\,FeO + Ti_2O_3 \tag{5.1}$$

5.2 Metal composition

As seen in section 4.2, the metal samples contain very small amounts of anything but iron. Table 5.1 shows a version of table 4.1, with the chemical analysis for only the studied elements.

Table 5.1: Normalised results of chemical analysis on refined metal done by Sintef Norlab.

Element	**Sample 1**	**Sample 2**	**Sample 3**	**Sample 4**	**Sample 5**	**Sample 6**
Fe (wt%)	97,33	97,41	97,35	99,58	99,70	99,73
C (wt%)	2,42	2,26	1,98	0,19	0,09	0,02
Ti (wt%)	<0,02*	0,16	0,46	<0,02*	<0,02*	<0,02*

** Element not found in sample, lower detection limit displayed.*

We see that titanium is only found in samples 2 and 3, resulting from combining low amounts of Fe_2O_3 with medium and high amounts of Ti respectively. These are the same samples in which TiC-particles were found. The relatively high amount of titanium detected could then either be because not enough Fe_2O_3 was present to oxidise it all or because it was trapped in the metal in carbide form.

As for why the samples contain carbides, we turn to the phase diagram in figure 2.5. It can here be seen that the initial metal compositions for samples 2, 3, 5 and 6 are actually within the primary crystallisation area of TiC. It should however not form at temperatures above 1400 °C. The particles are thus not an equilibrium phase at 1600 °C. If we assume that they formed during cooling, we can attribute the difference to the increased oxidation of both carbon and titanium in samples 5 and 6. If we think they might have formed during heating however, the difference in heating rate may have been the cause. As shown in table

3.4, a higher heating rate was used in experiments 2 and 3. As higher heating rates lead to less uniform heating, conditions allowing for TiC formations may have occurred locally in these samples. Thus, the particles in sample 2 and 3 may be either a cause or a consequence of reduced Ti removal.

The amount of carbon found in the samples supports the model results discussed in section 5.1. Samples 1-3 were exposed to low amounts of Fe_2O_3 and contains carbon comparable to the initial levels. Samples 4-6 were exposed to higher amounts of Fe_2O_3 and contains much less carbon after refining. The predicted preferential oxidation of titanium would explain this difference. Figure 5.2 show the metal composition after refining as measured in the samples and compared to model results at the same conditions. The content of titanium is displayed as the lower detection limit for the samples where it was not detected, indicated by lower error bars. We see here that when low amounts of Fe_2O_3 is used, the resulting metal contains a varied and somewhat unpredictable amount of titanium. When much Fe_2O_3 is available this is less of an issue for titanium, but more so for carbon.

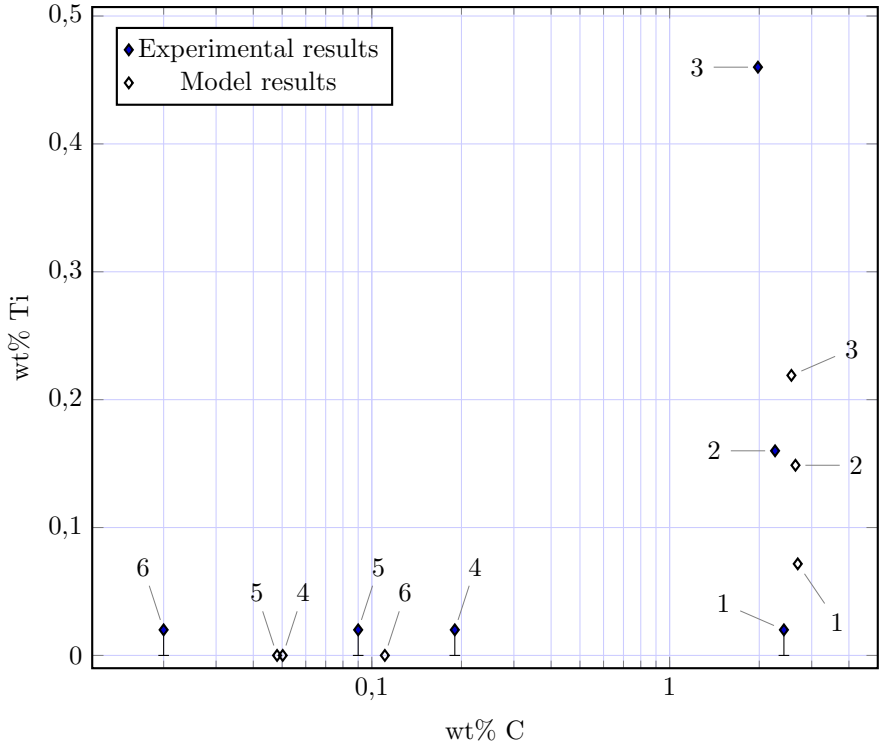

Figure 5.2: Comparison of metal composition from experimental and modelling results.

5.3 Distribution of titanium

As the main purpose of this project is to study the transfer of titanium from the metal to the slag, looking further at the distribution coefficients may provide some insight. These are defined in section 2.6 as the ratio of at% Ti in the slag over that in the metal. The percentages and resulting coefficients are shown in table 5.2.

Table 5.2: Content of titanium and titanium distribution coefficients from experimental samples.

Sample	**1**	**2**	**3**	**4**	**5**	**6**
(%Ti)	0,24	0,39	0,36	0,11	0,53	0,91
[%Ti]	<0,02	0,17	0,50	<0,02	<0,02	<0,02
L_{Ti}	>11,10	2,27	0,71	>4,93	>22,66	>38,95

From this table it becomes evident that the low Ti content in the slag from experiment 4 observed before is not balanced by a higher content in the metal. It is therefore considered likely that the measured amount of titanium in slag 4 is wrong, and should be somewhere between the values from samples 1 and 5. This would also make the distribution coefficient higher. Similarly, the distribution coefficients for samples 2 and 3 seem inconsistently low considering their slags contain more titanium than that of sample 1. This is likely because their [%Ti]-values are artificially increased by TiC particles in the metal, as shown in section 4.2. While this titanium is still trapped in the metal, it is not dissolved and can be removed by other means.

In figure 5.3, the partition coefficients from experimental measurements are compared to those predicted by the model. Three graphs are shown, one for each starting alloy. They are also compared to calculations done using the FactSage 8.0 software. Arrows are used on the experimental values to show that these would be higher if more accurate values for [%Ti] were available.

We see that the distribution coefficients from the refining experiments are much lower than predicted by the model, but this comparison is of little value when the titanium could not be measured to the accuracy used by the model. However, the predictions of the model are similar to the calculations from FactSage with regards to the three regions described in section 5.1. The trend of increasing distribution coefficients is evident regardless of method, especially if the results from slag sample 4 are wrong as discussed. Thus, the effectiveness of Fe_2O_3 for removal of titanium is clearly demonstrated, but only in a qualitative manner.

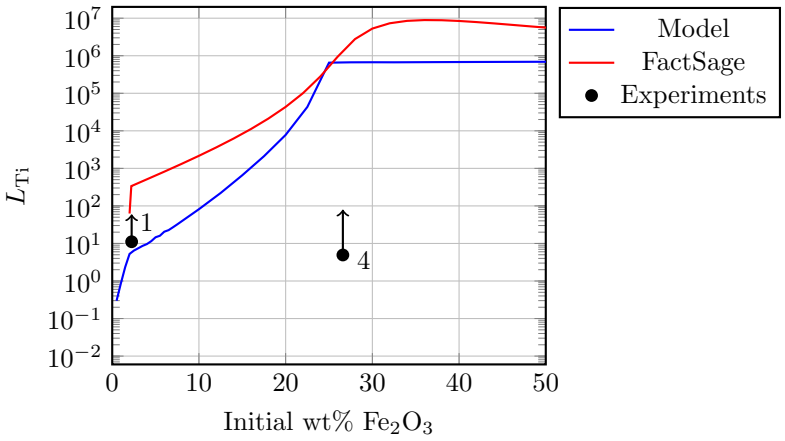

(a) 0,5 wt% initial Ti in the metal.

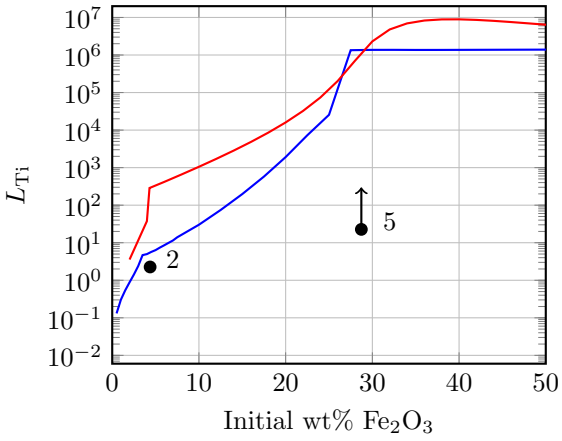

(b) 1,0 wt% initial Ti in the metal.

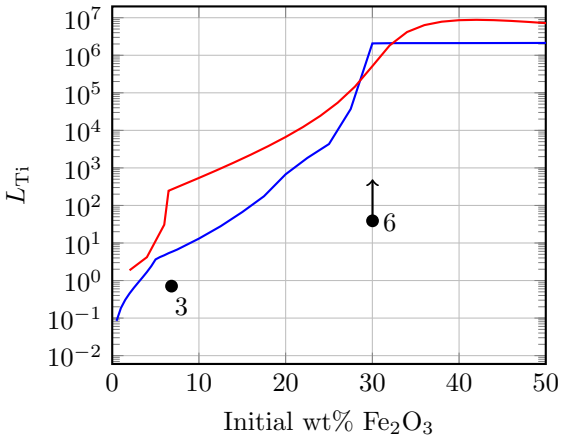

(c) 1,5 wt% initial Ti in the metal.

Figure 5.3: Comparison of partition coefficients between model results, experimental results and calculations from FactSage 8.0 [13].

5.4 Structure of refining slag

In order to determine what phases are present in the refining slag after solidification, the WDS results for each slag sample is compared with the phases presented in the phase diagrams in section 2.2. Table 5.3 shows the normalised XRF results for these slags, which can be used in conjunction with the phase diagrams to determine what phases can be expected. As the stochiometric ratios of metallic elements in the slag phases are known by the phase labels, such as 6:7 Ca:Al in the $Ca_{12}Al_{14}O_{33}$ phase, converting the WDS results to atomic percentages allows for direct comparison.

Table 5.3: Normalised results of XRF-analysis on refining slag. LOI indicates loss on ignition. Results are semi-quantitative.

Sample	**1**	**2**	**3**	**4**	**5**	**6**
MgO (wt%)	8,17	8,13	8,37	9,22	10,44	9,83
Al_2O_3 (wt%)	45,55	45,49	45,96	44,91	43,35	42,72
SiO_2 (wt%)	0,21	0,21	0,19	0,93	1,01	1,10
P_2O_5 (wt%)	0,01	0,01	0,01	0,01	0,01	0,01
SO_3 (wt%)	0,02	0,01	0,01	0,10	0,11	0,08
CaO (wt%)	43,87	44,20	44,45	43,07	41,61	41,24
TiO_2 (wt%)	0,81	1,34	1,23	0,39	1,81	3,12
Cr_2O_3 (wt%)	-	-	-	0,01	0,02	0,02
Fe_2O_3 (wt%)	0,14	0,07	0,06	1,36	1,59	1,88
SrO (wt%)	0,02	0,02	0,02	0,02	0,02	0,02
Mn_2O_3 (wt%)	0,01	0,01	0,01	0,03	0,04	0,04
LOI (wt%) 1000 °C	1,21	0,51	-0,29	-0,05	-0,02	-0,06
Sum (wt%)	100,00	100,00	100,00	100,00	100,00	100,00

From the CaO-Al_2O_3 system, the $Ca_{12}Al_{14}O_{33}$ phase is likely to appear as the main matrix phase when CaO and Al_2O_3 are present in around equal amounts. A second phase could then be either $Ca_3Al_2O_6$ or $CaAl_2O_4$. In the latter two phases, Al can be replaced by Fe. As seen in the phase diagram in figure 2.7, a phase containing almost only MgO is likely to be present. A small amount of MgO is also reported to be solvable in the CaO-Al_2O_3 phases. As seen in the phase diagram of figure 2.6b, the titanium is unlikely to be present together with aluminium, but may form compounds with calcium, such as $Ca_3Ti_2O_7$ or $Ca_6Ti_4O_{13}$.

Sample 1

The EPMA analysis of sample 1 revealed it to consist of 3 distinct, seemingly homogeneous areas. Table 5.4 shows the elemental composition of each phase as measured by WDS. It is proposed that the dendrite phase in area A, which seems to be relatively pure MgO and appears in all samples, was the first to solidify. It is suggested that the matrix around the dendrites solidified next, and that this phase is $Ca_{12}Al_{14}O_{33}$ with very small amounts other

dissolved elements. The remaining liquid, containing most of the almost negligible amount of titanium, will then have solidified into a phase very similar to $Ca_3Al_2O_6$ in composition.

Table 5.4: Characterisation of slag phases from experiment 1.

Area	Content (at%)						Suggested
	Ca	Al	Fe	Ti	Mg	O	phases
1A	26,47	18,16	0,01	0,24	0,46	54,66	$Ca_3Al_2O_6$
1B	19,41	23,81	0,01	0,11	0,67	56,00	$Ca_{12}Al_{14}O_{33}$
1C	0,65	0,76	0,07	0,03	48,20	50,20	MgO

Sample 2

Also sample 2 was revealed to have solidified into 3 distinct areas, with the dendrites being MgO and the matrix being $Ca_{12}Al_{14}O_{33}$. Based on the fine structure of the last area, it is suggested that the the remaining liquid solidified as a eutectic containing $Ca_3Al_2O_6$ and a different Ti-containing phase.

Table 5.5: Characterisation of slag phases from experiment 2.

Area	Content (at%)						Suggested
	Ca	Al	Fe	Ti	Mg	O	phases
2A	23,82	19,03	0,00	1,08	0,76	55,30	Eutectic
2B	19,38	23,78	0,00	0,14	0,68	56,02	$Ca_{12}Al_{14}O_{33}$
2C	0,59	0,62	0,01	0,01	48,60	50,16	MgO

Sample 3

The slag in sample 3 had separated into two areas with different colouring during solidification. The blue area in figure 4.13a solidified in contact with the gas phase while the green area in figure 4.13b solidified in contact with the metal. The reason for this separation could either be a local difference in composition or from a local difference in cooling rate. We see that with the exception of titanium, which is shown by the x-ray map in figure 4.14b to have formed particles, the composition of the green area labelled 3E in table 5.6 is reminiscent of the average slag composition as displayed in table 5.3. While the composition is similar to that of the $Ca_3MgAl_4O_{10}$ phase, the lack of dendrites and overall homogeneity of the area suggests a semi-amorphous structure. The placement of titanium particles contradicts this however, as they seem to follow crystalline grain boundaries.

As for the blue area, there are four distinct areas visible. The usual MgO dendrites are labelled 3D, while 3A and 3B are close in composition to $Ca_3Al_2O_6$ and $Ca_{12}Al_{14}O_{33}$ respectively. The phase present in largest area, 3C, is more difficult to determine. As seen in table 5.6, the magnesium content does not satisfy the stochiometry of the $Ca_3MgAl_4O_{10}$ or

$Ca_7MgAl_{10}O_{15}$ phases. As the analysis is not completely quantitative and the phases may allow for some extra magnesium, it could be either of these two. Another possibility is for Mg^{2+} cations to substitute for Ca^{2+} cations in mayenite, forming a phase described in the table as $(Ca, Mg)_{12}Al_{14}O_{33}$.

Table 5.6: Characterisation of slag phases from experiment 3.

Area	Content (at%)						Suggested phases
	Ca	Al	Fe	Ti	Mg	O	
3A	26,28	18,35	0,00	0,17	0,52	54,67	$Ca_3Al_2O_6$
3B	19,30	23,98	0,00	0,10	0,59	56,04	$Ca_{12}Al_{14}O_{33}$
3C	17,38	22,22	0,00	0,11	4,23	55,61	$(Ca, Mg)_{12}Al_{14}O_{33}$
3D	1,06	1,05	0,01	0,02	47,59	50,27	MgO
3E	18,15	20,97	0,01	0,22	5,29	55,35	Amorphous

Sample 4

In sample 4, two matrix phases are visible, labelled 4B and 4C. As shown in table 5.7, these are likely to be the $Ca_{12}Al_{14}O_{33}$ and $Ca_3Al_2O_6$ phases. In addition to these and the MgO dendrites, there are particles containing most of the titanium and iron present in the slag. These particles appear homogeneous, so a quarternary CaO-Al_2O_3-TiO_x-FeO_x phase seems to have formed. If titanium were able to substitute for aluminium in the same way as iron, the stochiometry would match a $Ca_2(Al, Fe, Ti)_2O_5$ phase. The phase diagrams of section 2.2 does not support this however.

Table 5.7: Characterisation of slag phases from experiment 4.

Area	Content (at%)						Suggested phases
	Ca	Al	Fe	Ti	Mg	O	
4A	22,13	12,91	2,32	5,67	0,90	56,06	-
4B	26,58	18,16	0,28	0,10	0,29	54,59	$Ca_3Al_2O_6$
4C	19,45	23,95	0,11	0,03	0,46	56,00	$Ca_{12}Al_{14}O_{33}$
4D	0,32	0,42	0,99	0,01	48,15	50,11	MgO

Sample 5

Slag sample 5 consists of 4 different areas, of which only the MgO dendrites are easily identifiable. The matrix seems to be the same as the one in 3C, comparable to $Ca_{12}Al_{14}O_{33}$ in composition, but with a substantial amount of magnesium as seen in the row for 5C in table 5.8. The other matrix-like phase in 5B is clustered with particles, but is suggested to be $Ca_3Al_2O_6$. There are two kinds of particles in this slag, the ones large enough to be analysed are labelled 5A. These seem to contain most of the titanium in the system, but

some is also present in the 5B areas. This can be either as part of the matrix phase or in the smaller particles.

Table 5.8: Characterisation of slag phases from experiment 5.

Area	Content (at%)						Suggested phases
	Ca	Al	Fe	Ti	Mg	O	
5A	22,09	10,88	0,51	8,51	1,04	55,30	-
5B	25,97	16,05	0,24	2,02	0,69	56,02	$Ca_3Al_2O_6$ + particles w/ Ti
5C	16,88	22,55	0,35	0,04	4,51	55,66	$(Ca, Mg)_{12}Al_{14}O_{33}$
5D	0,41	0,54	1,13	0,01	47,77	50,14	MgO

Sample 6

In slag sample 6 we see the usual MgO dendrites together with mixed areas containing particles in a CaO-Al_2O_3 matrix. This matrix, labelled 6B in table 5.9, is similar to the ones in 3C and 5C. The titanium is concentrated in the 6A particles or the area around, and the dendrites contain most of the iron in the system. Unlike other samples, this slag contains no areas with magnesium levels below 1 at%.

Table 5.9: Characterisation of slag phases from experiment 6.

Area	Content (at%)						Suggested phases
	Ca	Al	Fe	Ti	Mg	O	
6A	21,86	12,52	0,52	7,15	1,24	56,71	$Ca_3Al_2O_6$ + $Ca_3Ti_2O_6$
6B	16,64	23,42	0,32	0,12	3,58	55,91	$(Ca, Mg)_{12}Al_{14}O_{33}$
6C	0,41	0,53	1,60	0,02	47,30	50,14	MgO

Summary

All slags contain almost 10 wt% MgO, which seems to have solidified as a rather pure phase as the first solidification step, based on the dendrittic structure of the phase. These dendrites also contain some iron oxides in the samples where Fe is present. It is proposed that the next phases to solidify are either $Ca_{12}Al_{14}O_{33}$ or $Ca_3Al_2O_6$ depending on composition. In some cases the former contains around 4 at% magnesium, and may instead be the $Ca_3MgAl_4O_{10}$ phase. Most of the titanium seems to be in the last remaining liquid, and appears to either solidify into particles or structures reminiscent of eutectics in which some iron may also be found.

Chapter 6

Conclusion

The removal of titanium from pig iron by use of slag refining is by the results of this project deemed to be feasible. Alloys with initial titanium content between 0,5 wt% and 1,5 wt% were used, and final levels below the detectable limit of 0,020 wt% were achieved for all of them. Calculations from both the project model and FactSage predict even more effective removal, but this could not be quantitatively verified by experimental work. Using a method for analysis with a lower detection limit could have provided even more insight into the effectiveness of removal.

The slag is shown to contain significant amounts of MgO after refining, which originates from the crucibles. While it appears to have had a minimal impact on the slag phases formed during solidification, its effect on the liquid equilibrium is unexplored as it was not included in the modelling.

Titanium is shown to preferentially oxidise even in the presence of carbon, but not to a degree where the latter can be ignored. This is in accordance with the predictions of the model. The partial oxidation of carbon consumes Fe_2O_3 and must thus be accounted for. At low amounts of Fe_2O_3 there is also a risk of forming TiC-particles in the metal, which requires another method for removal. Effective and predictable refining therefore seems to require more Fe_2O_3 than what is necessary by stochiometry.

References

[1] Arnim von Gleich. "Outlines of a Sustainable Metals Industry". en. In: *Sustainable Metals Management: Securing our Future - Steps Towards a Closed Loop Economy*. Ed. by Arnim von Gleich, Robert U. Ayres, and Stefan Gößling-Reisemann. Eco-Efficiency in Industry and Science. Dordrecht: Springer Netherlands, 2006, pp. 3–39. ISBN: 978-1-4020-4539-4.

[2] *ENSUREAL – sustainable alumina production*. URL: `https://www.ensureal.com/` (visited on 07/07/2020).

[3] Adamantia Lazou et al. "On the Direct Reduction Phenomena of Bauxite Ore Using H2 Gas in a Fixed Bed Reactor". en. In: *Journal of Sustainable Metallurgy* 6.2 (June 2020), pp. 227–238. ISSN: 2199-3831. DOI: `10.1007/s40831-020-00268-5`.

[4] Jafar Safarian and Leiv Kolbeinsen. "Smelting-reduction of bauxite for sustainable alumina production". English. In: vol. 5. ISSN: 2291-1227 Journal Abbreviation: SISP. Flogen Star Outreach, Mar. 2016, pp. 149–158. ISBN: 978-1-987820-58-4.

[5] Jan Miller and Aake Irgens. "Alumina Production by the Pedersen Process — History and Future". en. In: *Essential Readings in Light Metals: Volume 1 Alumina and Bauxite*. Ed. by Don Donaldson and Benny E. Raahauge. Cham: Springer International Publishing, 2016, pp. 977–982.

[6] Fathi Habashi. "A Hundred Years of the Bayer Process for Alumina Production". en. In: *Essential Readings in Light Metals: Volume 1 Alumina and Bauxite*. Ed. by Don Donaldson and Benny E. Raahauge. Cham: Springer International Publishing, 2016, pp. 85–93. ISBN: 978-3-319-48176-0. DOI: `10.1007/978-3-319-48176-0_12`.

[7] Fabian Imanasa Azof et al. "Leaching characteristics and mechanism of the synthetic calcium-aluminate slags for alumina recovery". In: *Hydrometallurgy* 185 (May 2019), pp. 273–290.

[8] Hanne Sellaeg, Leiv Kolbeinsen, and Jafar Safarian. "Iron Separation from Bauxite Through Smelting-Reduction Process". en. In: *Light Metals 2017*. Ed. by Arne P. Ratvik. The Minerals, Metals & Materials Series. Cham: Springer International Publishing, 2017, pp. 127–135.

[9] Ivan Anich et al. "The Alumina Technology Roadmap". en. In: *Essential Readings in Light Metals: Volume 1 Alumina and Bauxite*. Ed. by Don Donaldson and Benny E. Raahauge. Cham: Springer International Publishing, 2016, pp. 94–99. ISBN: 978-3-319-48176-0. DOI: `10.1007/978-3-319-48176-0_13`.

[10] Christoph Schmitz. *Handbook of Aluminium Recycling*. en. Vulkan-Verlag GmbH, 2006. ISBN: 978-3-8027-2936-2.

[11] Ken Evans. "The History, Challenges, and New Developments in the Management and Use of Bauxite Residue". en. In: *Journal of Sustainable Metallurgy* 2.4 (Dec. 2016), pp. 316–331. ISSN: 2199-3831. DOI: `10.1007/s40831-016-0060-x`.

[12] Daniel Winkler et al. "Long-term ecological effects of the red mud disaster in Hungary: Regeneration of red mud flooded areas in a contaminated industrial region". en. In: *Science of The Total Environment* 644 (Dec. 2018), pp. 1292–1303. ISSN: 0048-9697. DOI: 10.1016/j.scitotenv.2018.07.059.

[13] *FactSage*. Montreal, Canada; Achen, Germany, 2020. URL: http://www.factsage.com/.

[14] Fabian Imanasa Azof, Leiv Kolbeinsen, and Jafar Safarian. "Characteristics of Calcium-Aluminate Slags and Pig Iron Produced from Smelting-Reduction of Low-Grade Bauxites". en. In: *Metallurgical and Materials Transactions B* 49.5 (Oct. 2018), pp. 2400–2420. ISSN: 1543-1916. DOI: 10.1007/s11663-018-1353-1.

[15] Terkel Rosenqvist. *Principles of Extractive Metallurgy*. en. Tapir Academic Press, 2004. ISBN: 978-82-519-1922-7.

[16] Verlag Stahleisen and Verein Deutscher Eisenhüttenleute (R.F.A). *Slag atlas*. English. 2nd. OCLC: 493877454. Dusseldorf: Verlag Stahleisen GmbH, 1995. ISBN: 978-3-514-00457-3.

[17] P. Herasymenko. "Electrochemical theory of slag-metal equilibria. Part I.—Reactions of manganese and silicon in acid open-heart furnace". en. In: *Transactions of the Faraday Society* 34.0 (Jan. 1938). Publisher: The Royal Society of Chemistry, pp. 1245–1254. ISSN: 0014-7672. DOI: 10.1039/TF9383401245.

[18] Yoshio Waseda and J. M. Toguri. *Structure And Properties Of Oxide Melts, The: Application Of Basic Science To Metallurgical Processing*. English. Singapore: World Scientific, 1998. ISBN: 978-981-02-3317-4.

[19] Kai Tang and Merete Tangstad. "Modeling Viscosities of Ferromanganese Slags". In: New Delhi, India, 2007, pp. 344–357.

[20] Ziwei Chen et al. "Insight into the Relationship Between Viscosity and Structure of CaO-SiO2-MgO-Al2O3 Molten Slags". In: *Metallurgical and Materials Transactions B* (Aug. 2019). DOI: 10.1007/s11663-019-01660-7.

[21] James E. Shelby. *Introduction to Glass Science and Technology*. English. 2nd. Cambridge: The Royal Society of Chemistry, 2005. ISBN: 0-85404-639-9.

[22] W. Kurz and D. J. Fisher. *Fundamentals of Solidification*. English. 4th edition. Uetikon-Zuerich, Switzerland ; Enfield, N.H: CRC Press, June 1998. ISBN: 978-0-87849-804-8.

[23] Svein Stølen. *Chemical thermodynamics of materials: macroscopic and microscopic aspects*. eng. Pages: XII, 395. Chichester: Wiley, 2004. ISBN: 978-0-471-49230-6.

[24] Thorvald Abel Engh. *Principles of metal refining*. eng. Oxford: University Press, 1992. ISBN: 978-0-19-856337-2.

[25] Guo Yuanchang, Wang Changzhen, and Yu Hualong. "Interaction coefficients in the iron-carbon-titanium and titanium-silver systems". en. In: *Metallurgical Transactions B* 21.3 (June 1990), pp. 537–541. ISSN: 1543-1916. DOI: 10.1007/BF02667866.

[26] Geoffrey Sigworth and J. Elliott. "The Thermodynamics of Liquid Dilute Iron Alloys". In: *Metal Science* 8 (Jan. 1974), pp. 298–310. DOI: 10.1179/msc.1974.8.1.298.

[27] Stefan Jonsson. "Assessment of the Fe-Ti-C system, calculation of the Fe-TiN system, and prediction of the solubility limit of Ti(C,N) in liquid Fe". en. In: *Metallurgical and Materials Transactions B* 29.2 (Apr. 1998), pp. 371–384. ISSN: 1543-1916. DOI: 10.1007/s11663-998-0114-y.

[28] Jan Ketil Solberg. *Teknologiske metaller og legeringer*. nob. Trondheim: Metallurgisk institutt, Norges tekniske høgskole, 1991.

[29] William D. Callister. *Materials science and engineering*. eng. 9th ed., SI Version. Pages: XXIII, 905. Hoboken, N.J: Wiley, 2015. ISBN: 978-1-118-31922-2.

[30] Wang Bo et al. "Effect of Calcium/Aluminium ratio on MgO containing calcium aluminate slags". en. In: *Light Metals 2011*. Ed. by Stephen J. Lindsay. Cham: Springer International Publishing, 2016, pp. 201–204. ISBN: 978-3-319-48160-9. DOI: 10.1007/978-3-319-48160-9_35.

[31] Merete Tangstad. *Metal production in Norway*. Akademika Publ, 2013. ISBN: 978-82-321-0241-9.

[32] Antti Roine. *HSC Chemistry*. Pori, 2019. URL: https://www.outotec.com/hsc.

[33] Magnus K. Windfeldt. *High temperature viscosity of molten CaO-Al2O3 slags*. en. Tech. rep. Trondheim: NTNU, IMA, Dec. 2019.

[34] Jarle Hjelen. *Scanning elektron-mikroskopi*. Metallurgisk institutt, NTH, Oct. 1986.

Appendix A

Software

A.1 HSC Chemistry 9

This section is based on the user's guide included in the HSC Chemistry 9 software [32].

HSC Chemistry is a thermochemical software created by Outotec. It is designed for various kinds of chemical reactions, equilibrium calculations and process simulations. It offers powerful ways to perform heat and material balances. It does not allow for non-ideality in solutions, and is in this project therefore only used as a source of thermodynamic data for elements, compounds and reactions. These are taken from the software's main database, which is compiled from over 900 different literature sources.

The software is comprised of several modules, each with a specific purpose. This project utilises the *Database* module as a source of molar weights and formation energies, the *Reaction Equations* module for reaction energies and equilibrium constants and the *Phase Stability Diagrams* to gain data for the Ellingham diagram in figure 2.9.

A.2 FactSage 8.0

This section is based on information available at the official FactSage website [13].

FactSage is a fully integrated database computing system in chemical thermodynamics, created as a collaboration between Thermfact/CRCT of Montreal, Canada and GTT-Technologies of Aachen, Germany. It allows for calculation of multiphase and multicomponent equilibria under a large range of constraints. Systems can easily be evaluated by creating phase diagrams with a wide choice of variables. In this project it is used to obtain non-ideal activity data and as a source of composition-temperature phase diagrams, both binary and ternary.

As FactSage is not made available to students at NTNU, all use of it for this project was done by Kai Tang from Sintef.

Appendix B

BSE images of metal

This section contains BSE images of the refined metal samples. This includes both larger versions of the ones displayed in section 4.2 as well as images taken at lower magnification. The dark spots are pores, except in samples 2 and 3 where some particles are found.

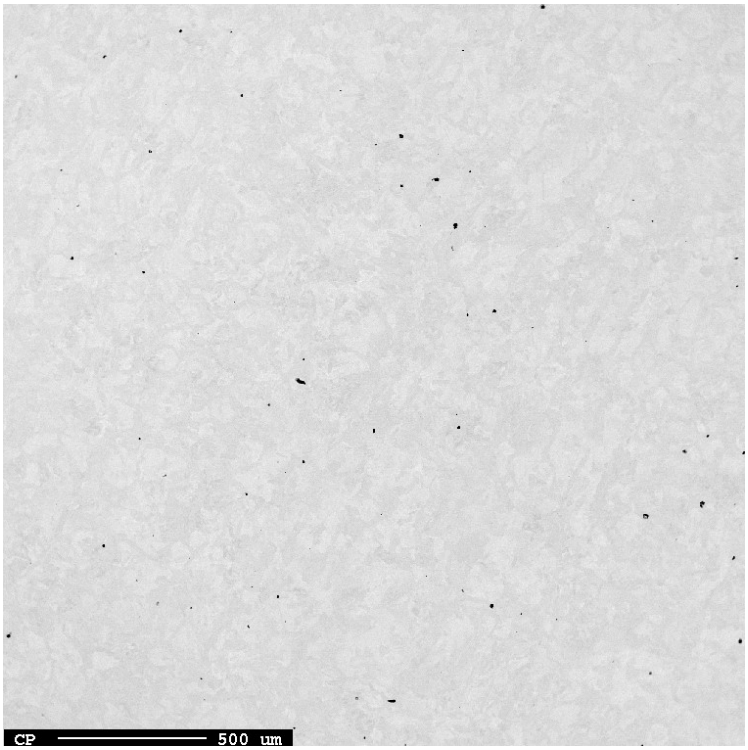

(a) x40 magnification.

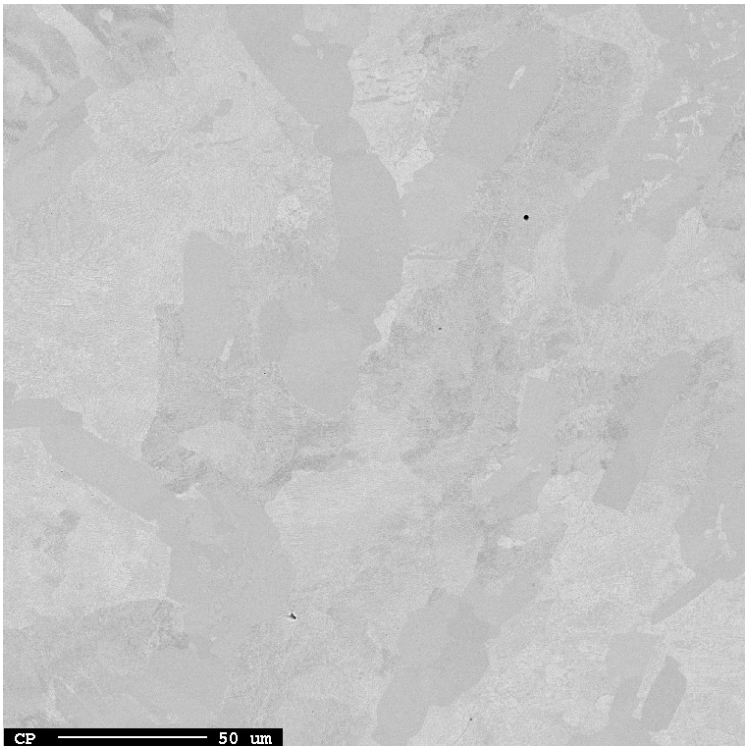

(b) x400 magnification.

Figure B.1: Backscatter images of the metal from experiment 1.

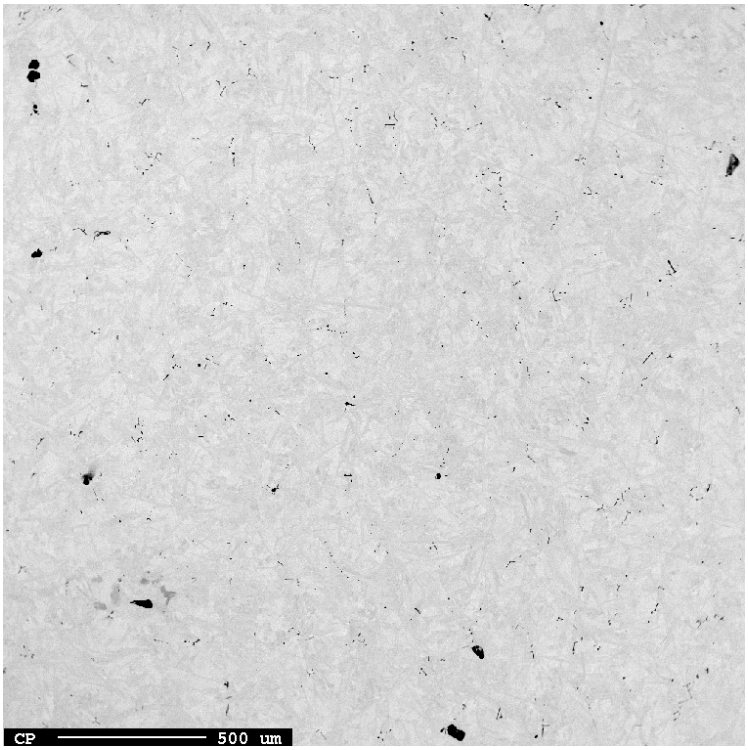

(a) x40 magnification.

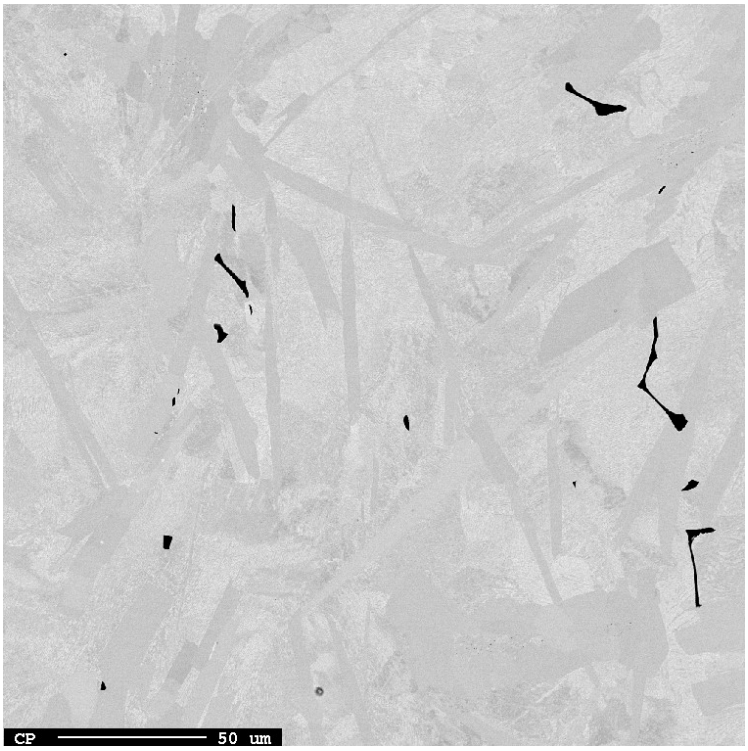

(b) x400 magnification.

Figure B.2: Backscatter images of the metal from experiment 2.

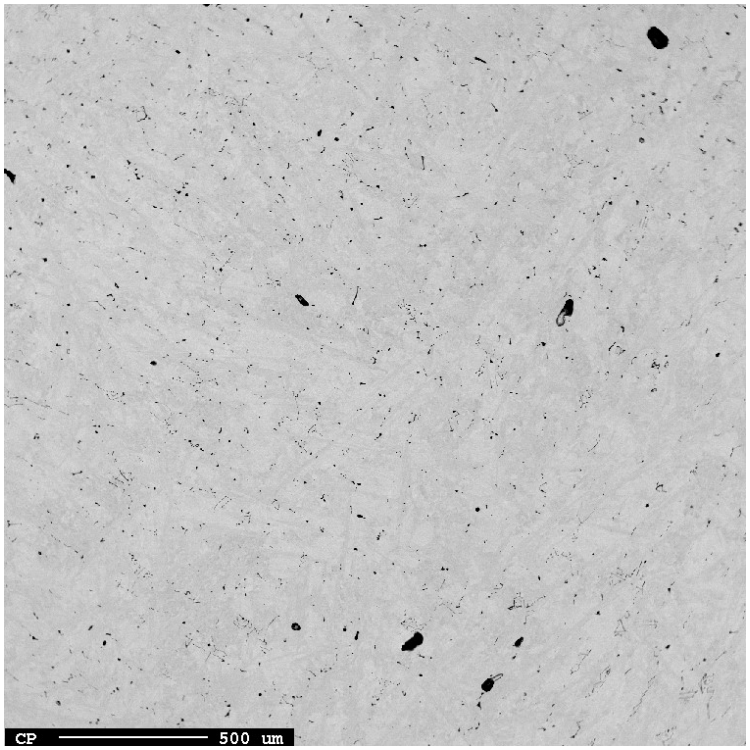

(a) x40 magnification.

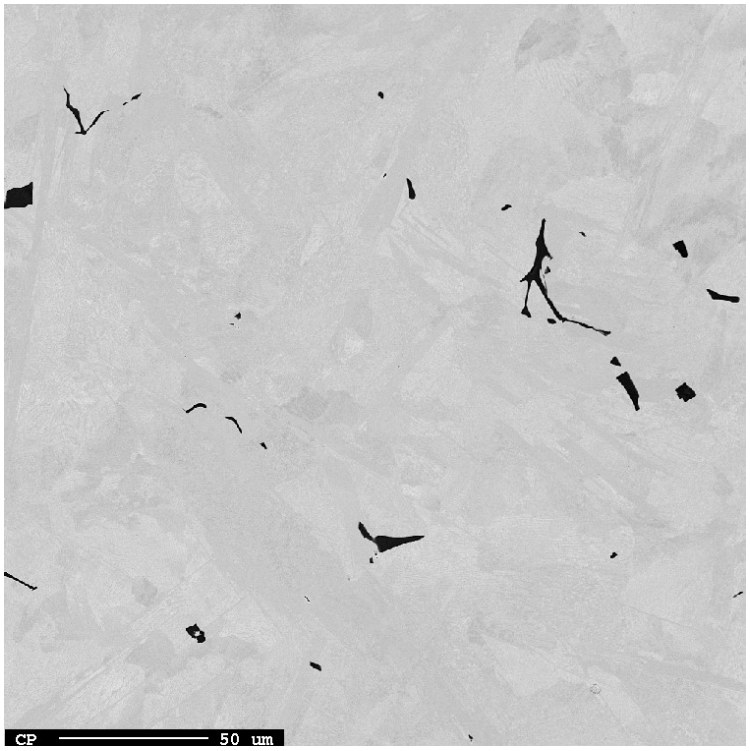

(b) x400 magnification.

Figure B.3: Backscatter images of the metal from experiment 3.

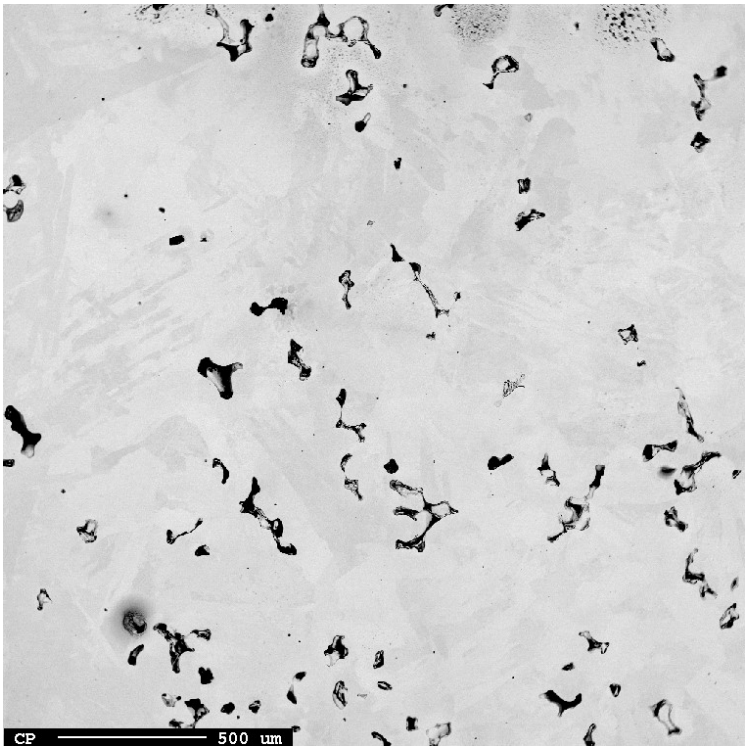

(a) x40 magnification.

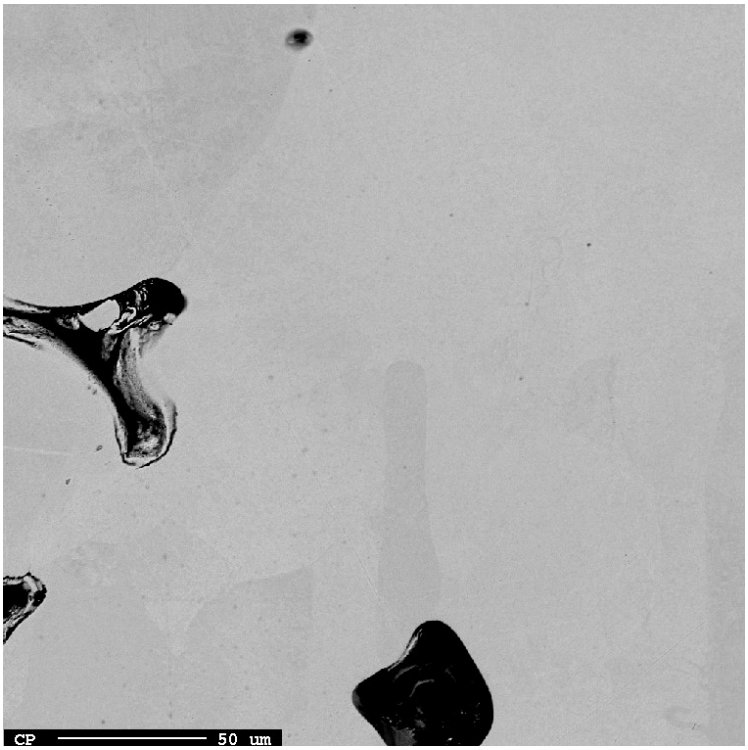

(b) x400 magnification.

Figure B.4: Backscatter images of the metal from experiment 4.

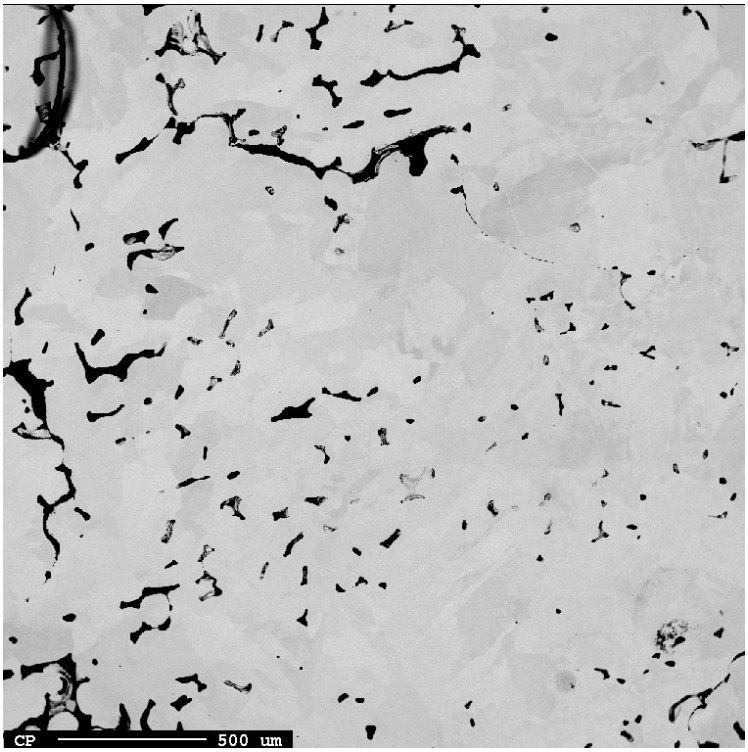

(a) x40 magnification.

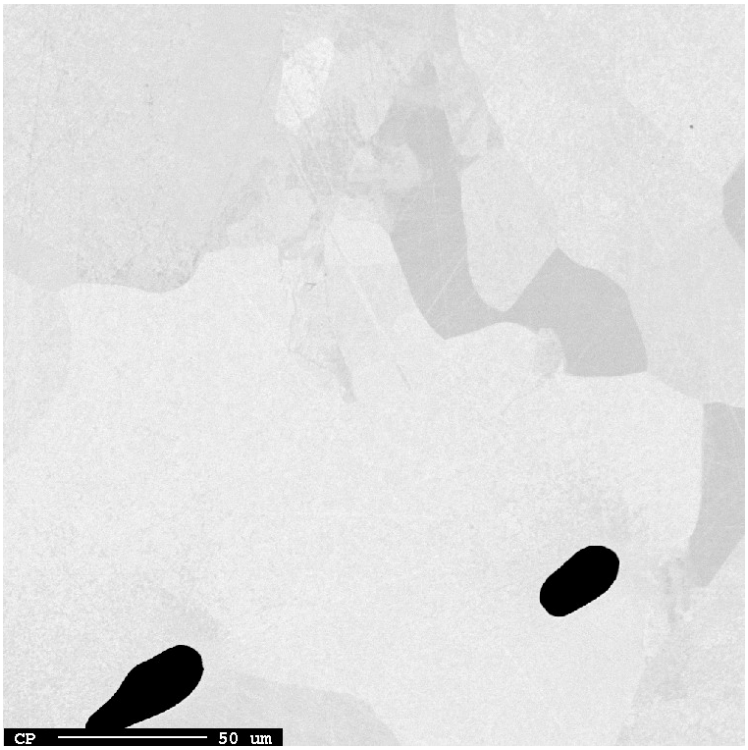

(b) x400 magnification.

Figure B.5: Backscatter images of the metal from experiment 5.

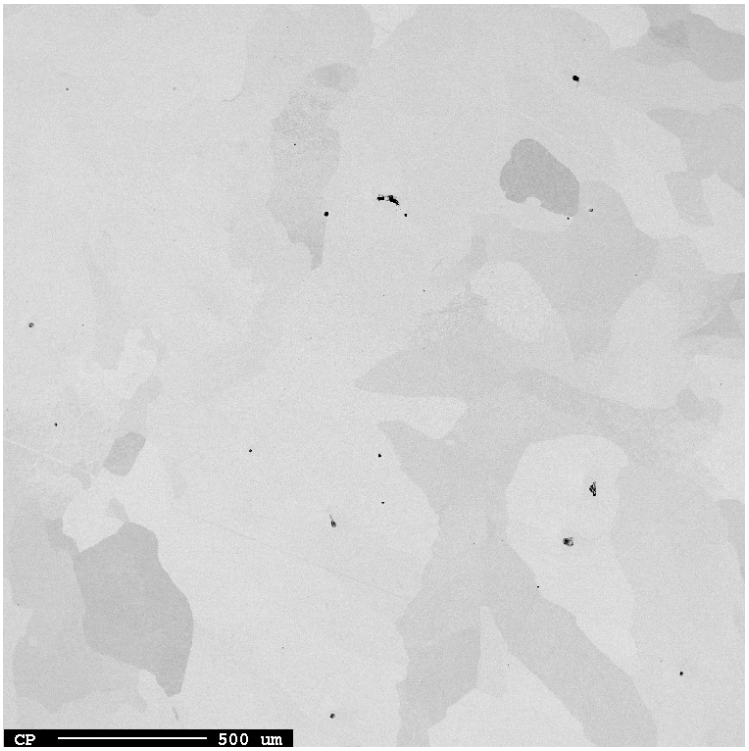

(a) x40 magnification.

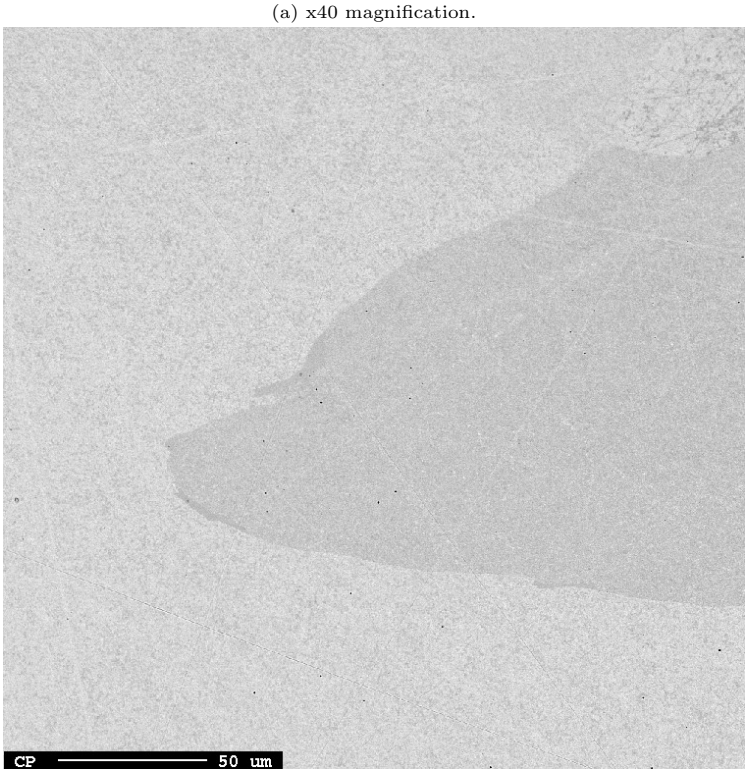

(b) x400 magnification.

Figure B.6: Backscatter images of the metal from experiment 6.

Appendix C

BSE images of slag

This section contains BSE images of the refining slag. These images are taken at lower magnification than the ones in section 4.3. The images of samples 2 and 6 include the slag-crucible boundary.

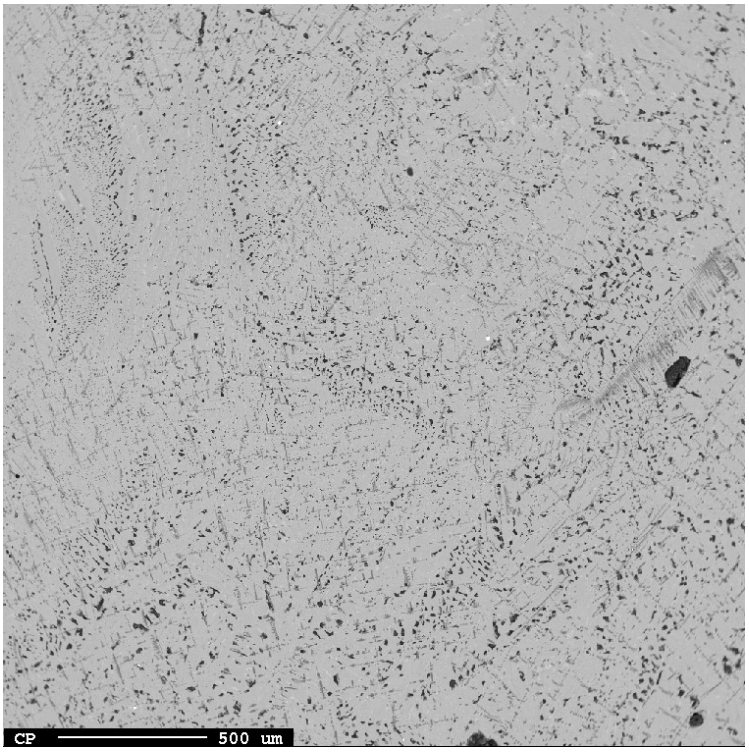

(a) x40 magnification.

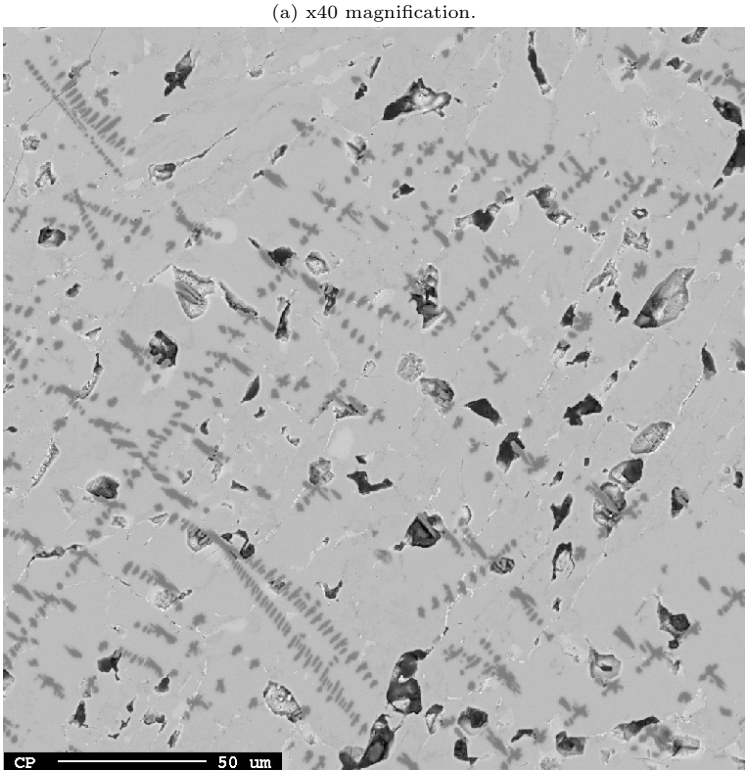

(b) x400 magnification.

Figure C.1: Backscatter images of the slag from experiment 1.

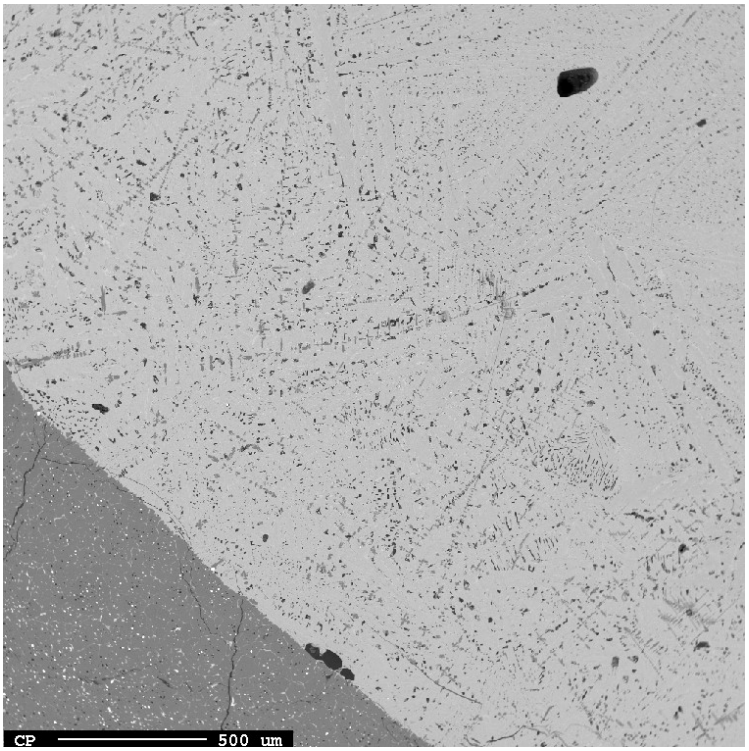

(a) x40 magnification.

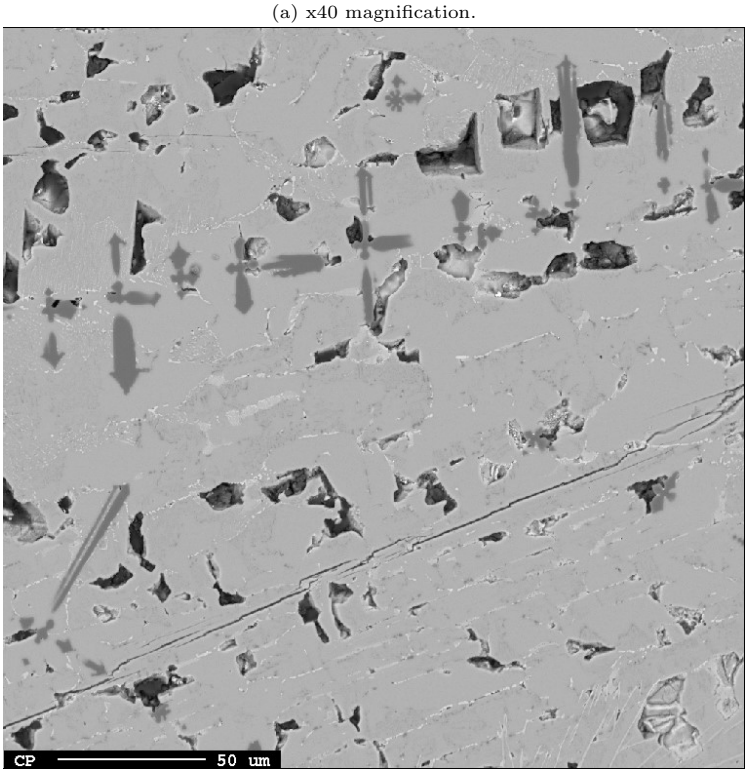

(b) x400 magnification.

Figure C.2: Backscatter images of the slag from experiment 2.

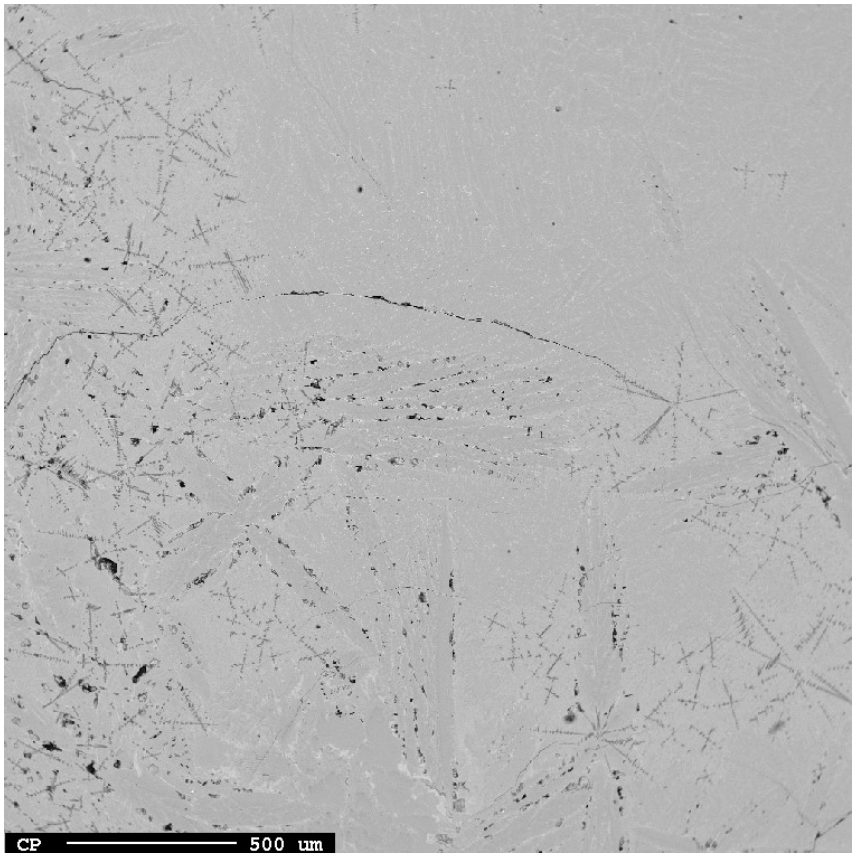

(a) x40 magnification.

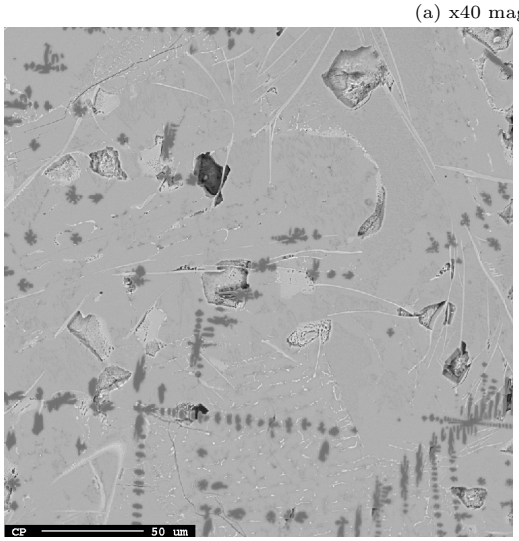

(b) x400 magnification of the blue area.

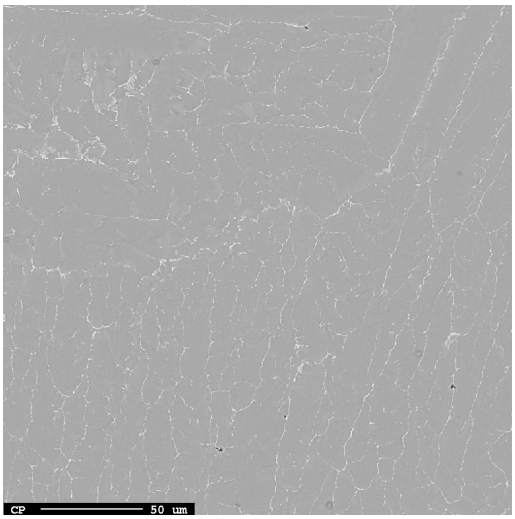

(c) x400 magnification of the green area.

Figure C.3: Backscatter images of the slag from experiment 3.

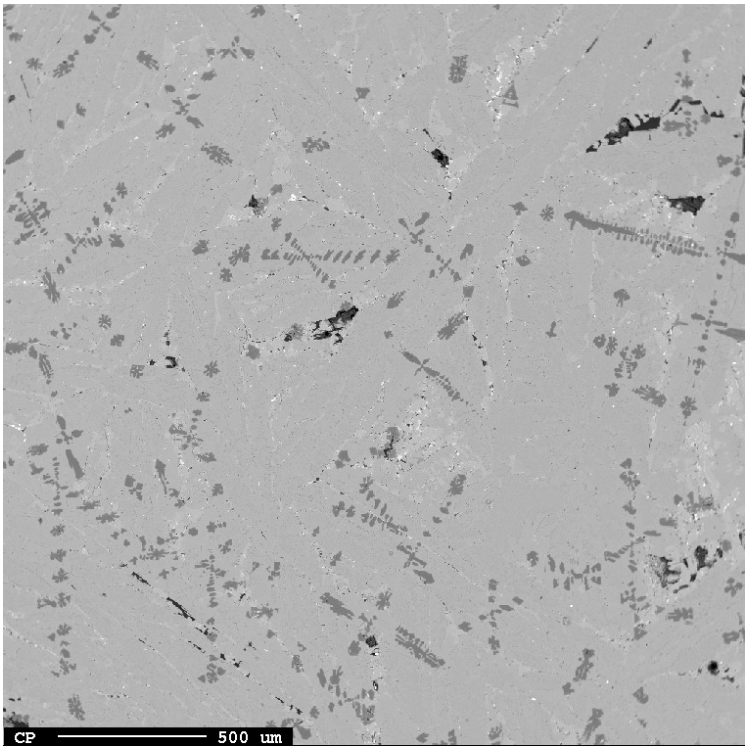

(a) x40 magnification.

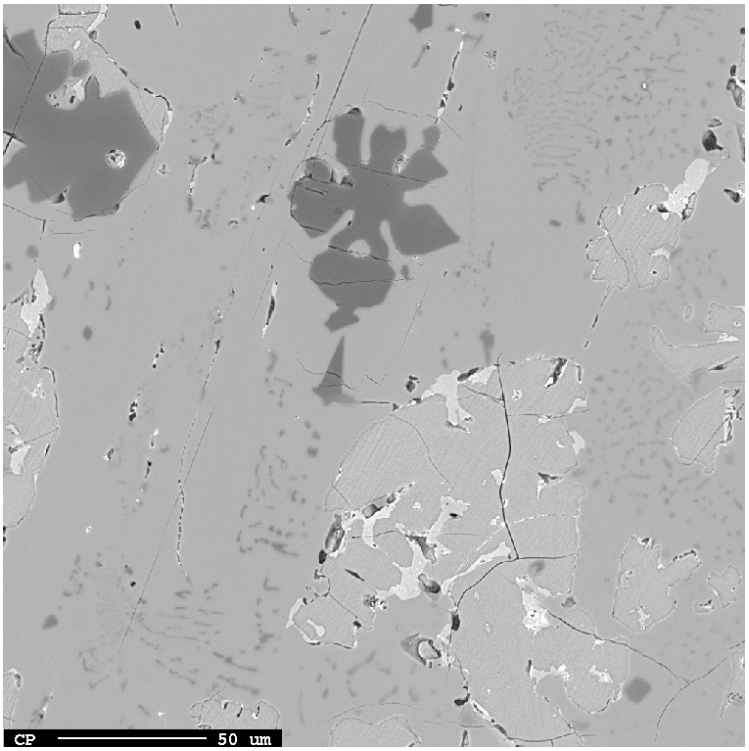

(b) x400 magnification.

Figure C.4: Backscatter images of the slag from experiment 4.

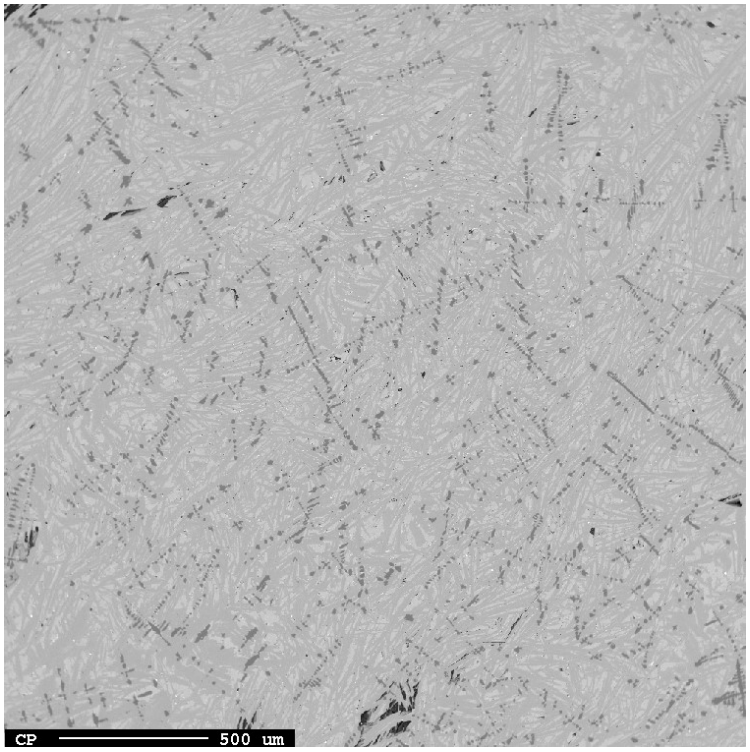

(a) x40 magnification.

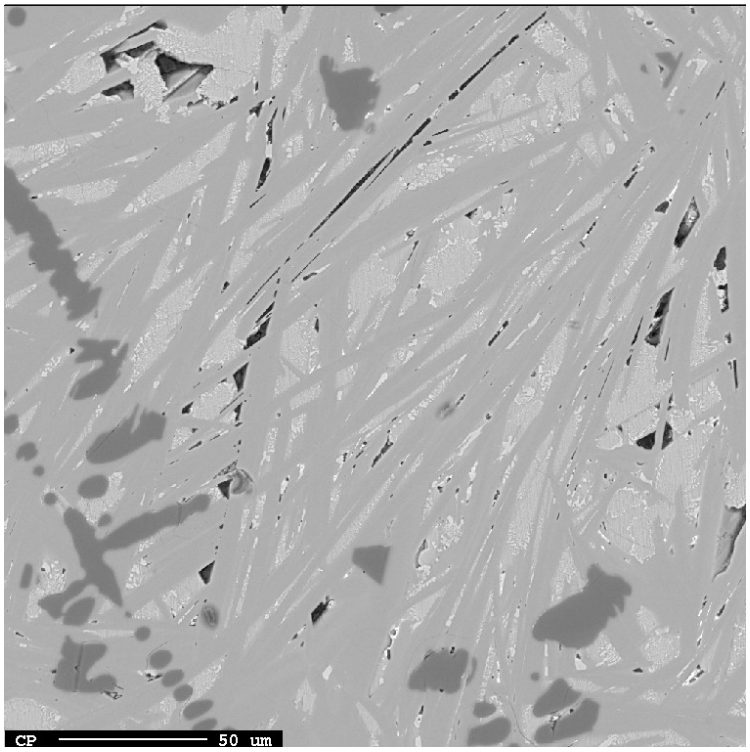

(b) x400 magnification.

Figure C.5: Backscatter images of the slag from experiment 5.

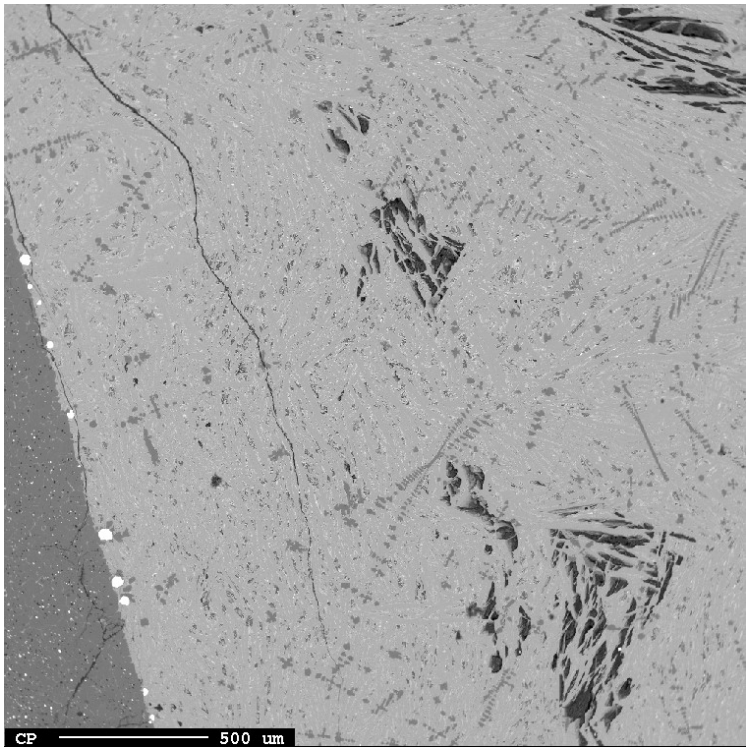

(a) x40 magnification.

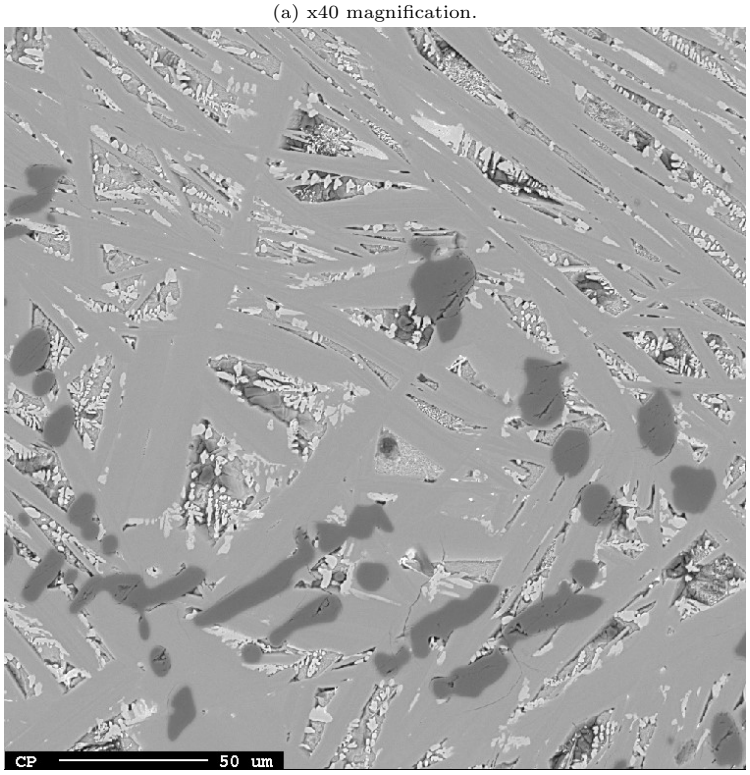

(b) x400 magnification.

Figure C.6: Backscatter images of the slag from experiment 6.

Magnus Kyrre Windfeldt

Removal of Ti from pig iron by slag refining

NTNU
Norwegian University of
Science and Technology